UCLouvain

epl

École polytechnique de Louvain

Strain engineering for opto-electronic properties change of Si & Ge at nanometer scale

And an improved data reduction scheme for lab-on-chip devices

Author: **Alex Pip**
Supervisor: **Prof. Jean-Pierre Raskin**
Readers: **Dr. Marie-Stéphane Colla, Prof. Hosni Idrissi, Prof. Thomas Pardoen**
Academic year 2019–2020
Master [120] in Chemical and Materials Engineering

Acknowledgement

This master thesis couldn't have been completed without the help and support of many people who I wish to thank here.
First, I would like to thank my supervisor, Prof. Jean-Pierre Raskin for his continuous support, presence and helpfulness despite his agenda and the complex situation brought by the covid19 crisis. I would also like to thank Prof. Pardoen for his unforeseen implication and his guidance at the most critical moments. I would also like to thank Nicolas Roisin for his involvement and expertise in semiconductor physics and Grégoire Le Brun for his decisive guidance with the sustainability assessment. Furthermore, I would like to thank Prof. Hosni Idrissi for taking the time to read this master thesis.
Finally I would like to deeply thank Dr. Marie-Stéphane Colla for her day-to-day availability, uplifting spirit and indispensable help throughout this very special semester.

List of Figures

1.1 What strain engineering can (theoretically) do: transform the indirect band gap of a semiconductor like germanium into a direct band gap. From [1] . . . 6
1.2 An elementary on-chip tensile testing device, a key MEMS-based device for this master thesis. From [2] . . . 7

2.1 Schematic drawing of a MOSFET transistor, where the dimension L designates the gate length. . . . 9
2.2 Typical CMOS chip structure. The transistors are on the bottom of the structure. Interconnects are the orange channels above the transistors. From [11] . . . 10
2.3 Energy required per bit of data versus *on-chip* interconnect length, from [5] . . . 11
2.4 Latency versus *on-chip* interconnect length, from [5] . . . 11
2.5 Power consumption versus *off-chip* interconnect length, for different technology nodes. The crossing between optical and electrical interconnect curve is called the critical length. From [5] . . . 12
2.6 Schematic diagram of an on-chip optical interconnect. Modified diagram from [12] . . . 12
2.7 Photonic interconnect: SiGe waveguide and Ge/SiGe active MQW modulator and photodetector, from [16] . . . 14
2.8 Diamond cubic crystal structure of Si and Ge, along with the [1 0 0], [0 0 1], [0 1 0] and [1 1 0] crystalline direction. From [17] . . . 15
2.9 First Brillouin zone for a FCC lattice. Corresponds to the Brillouin zone used to describe semiconductor with the diamond cubic crystal structure, from [18]. . . . 15
2.10 Band structure of nearly free electrons for Germanium. The band structure is only shown between the points of high symmetry L, Γ, X, κ in the first Brillouin zone of a diamond crystal structure. From [20] . . . 18
2.11 Band structure of Ge with the Tigh-Binding model, from [20]. . . . 18
2.13 Overlap of the p_x orbitals, forming a bonding and antibonding σ orbitals, from [20]. p_y and p_z orbital overlap perpendiculary to the direction of the bond, forming π orbitals 19
2.12 Result of the molecular orbital bonding in the H_2 molecule. The bonding orbital is the σ_{1s} and is filled with two electrons, from [22]. . . . 19
2.14 Evolution of s and p atomic orbitals into valence and conduction bands, in the case of a semiconductor, from [20]. $E_f = \epsilon_f$ is the Fermi energy in the crystal. . . . 19
2.15 Schematic representation of recombination mechanisms in Si, absorption and phonon-associated emission. E_g is the indirect band gap in this figure (in eV). From [25] . . . 21
2.16 **Left:** Bandgaps in Si, E_2 denotes the position of the indirect band gap with the lowest transition energy (Δ valley). E_1 represents the second indirect band gap with transition energy lower than the direct band gap E_g. **Right:** Absorption coefficient in Si. The peaks in absorption coincide with the transition energy of the E_2 and E_1 indirect bandgaps. From [26] . . . 22
2.17 Comparison of carrier distribution and light emission between Ge (left) and InGaAs (right). From [4] . . . 23
2.18 Photoluminescence in density Of States vs energy representation of the band structure. From [27] . . . 23

2.19 GaAs diode laser. The pAlGaAs-GaAs-nAlGaAs structure forms the heterojunction. From [26] . . . 24
2.20 Representation of strain-induced degeneracy lifting at the Γ point in the valence band of Si. **a,b** and **c** refers to, respectively, the unstressed, biaxially tensile stressed and unixially compressive stressed cases. From [18] . . . 26
2.21 Qualitative effect of strain on band gap, for Si, Ge and GaAs in different stress/strain configurations. From [18] . . . 27
2.22 Schematic representation ofΔ valley splitting in Si under [110] uniaxial tensile stress. The Δ valleys split into the Δ_2 and Δ_4-valleys, from [18] . . . 28
2.23 Band edges to be considered in the deformation potential calculation of band gap. Modified figure from [18]. . . . 28
2.24 Theoretical calculation and experimental measures of the strained Si indirect band gap for a biaxially tensile strained sample. Theoretical calculation where made using deformation potentials. From [30]. . . . 30
2.25 Comparison between theoretical calculation and experimental data of the strained direct and indirect band gap in Ge, for a [110] uniaxial tensile strain. Theoretical data are obtained from tight-binding and a modified deformation potential methods. From [28]. 30
2.26 Diagrams of band structures in momentum space. **(A)**: Reference, band structure of a direct band gap material such as GaAs. **(B)**: Unstrained Ge, excited electrons occupy the conduction band at the L-valleys, radiative recombinations of electrons are hindered by the momentum mismatch in the k-space. **(C)**: Band structure of Ge that has been strained to a sufficiently high value or has been alloyed with Sn. The balance of electron population between the Γ and L points are inverted and Ge behaves as a direct band gap material. From [1] . . . 30
2.27 Direct and indirect band gaps of Ge as a function of [100] uniaxial tensile strain (a), using deformation potentials and tight binding models (b). From [3] . . . 31
2.28 Relative offset of the Γ- and L-conduction bands in Ge that is either strained or alloyed with Sn. An offset below 0% means that the band gap is direct. Coloured arrows represent the offset experimentally achieved in the literature. From [1] . . . 31
2.29 Fraction of electrons present in direct valley rather than in indirect valley vs. temperature, theoretically calculated from the deformation potentials of Ge. a) Linear scale, b) log scale, from [35]. . . . 32
2.30 Actuator and sample of a lab-on-chip device. A mobile cursors moves with the actuator, while a fixed cursor on the sidewall acts as a reference for the direct measurement of displacement. From [37] . . . 33
2.31 VLS grown silicon nanowire, strained using a push-to-pull mechanism. From [36] . . . 33
2.32 Cross-sectionnal TEM image of the interface between a) Si and Ge in a thick film of Ge grown on a top of a SOI wafer b) Ge and SiO_2 (BOX) in a GeOI wafer. The TEM image show a lot more misfit dislocations in the thick Ge film grown on the SOI. From [3] 33
2.33 The SmartCut^{TM} process applied to GeOI wafer fabrication. From *Reboud et Al. (2017)*: "*Process flow to obtain optical GeOI substrates using the Smart Cut™ technology: (a) Ge growth on Si wafer, (b) Oxide deposition and H+ ion implantation, (c) Bonding onto a SiO2-Si handle, (d) Splitting of bonded wafers, (e) Surface cleaning by reactive ion etching and chemical mechanical polishing, then capping by 10 nm of deposited oxide.*"[3] 34
2.34 Top (A): Ge NM resting on a PI film, with holes used to introduce the etchant that allowed the top-Ge film to be removed from a GeOI wafer. Bottom (B): experimental set-up, with sample mount and high pressure gas chamber. From [38] . . . 35
2.35 Fabrication steps of the suspended micro-bridge design, to induce uniaxial strain in Ge nanowires. From [3] . . . 35
2.36 Micro cross design to induce biaxial strain in Ge. From [34] . . . 36
2.37 (a): SEM image of the suspended strained Ge pseudoheterostructure. (b): schematic representation of the band structure in the pseudoheterostructure. From [40] . . . 36
2.38 SEM image of the device: strained Ge pseudoheterostructure and DBR mirrors. From [41] 37

2.39 PL spectra for devices with 0%, 1.95% and 2.37% tensile strain. The direct-gap emission intensity increases greatly at higher strain [41]. 37
2.40 From [35]: "*Theoretical internal quantum efficiency of a Ge LED as a function of strain for various defect-limited minority carrier lifetimes at room temperature (300 K), assuming* 10^{19}*cm*$^{-3}$ *n-type doping and 1017 cm*$^{-3}$ *carrier injection.*" 38

3.1 Basic principle of the Raman spectroscopy: Rayleigh vs. Raman (Stokes and antistrokes) scattering in crystals, from [42] 39
3.2 "*Elementary internal stress actuated uniaxial tensile test structure, (a) before release, (b) after release*" from [2] 42
3.3 From [2]:"*Processing steps used to prepare tensile structures. (a) substrate, (b) deposition of the sacrificial layer, (c) deposition of the actuator, (d) patterning of the actuator, (e) deposition of the specimen layer, (f) patterning of the specimen and (g) release*" 43
3.4 SEM image of a released structure, displacement u highlighted in magenta. Modified image from [47] 44
3.5 Fabrication process of a SOI top film micro scale tensile testing device, from [48] . . . 46
3.6 Picture of one of the wafer that underwent failure during the RIE etching. Two zones can be distinguished: a circular purple zone on the left and a green moon crescent-shaped zone on the right. Ellispometry on the wafer revealed a partial etching combined with the formation of an unknown layer on top of the Si on the left zone and a completed Si etching on the right zone. 47
3.7 Photolithography process in 7 steps, the post-treatment step is an etching step. 49
3.8 Isotropic versus anisotropic etched of Si 49
3.9 CO_2 critical point drying represented on a (p, T) diagram, from [49] 50

4.1 Illustration: application of the data reduction scheme on experimental data from lab-on-chip devices. Blue data has been treated with the correction model. 51
4.2 Schematic decomposition of the displacement u into the displacements of smaller, distinct, elements. 53
4.3 Schematic representation of an on-chip tensile test structure, top view. The white dashed line delimits the under-etched zone. The zone inside the white dashed line is considered to be suspended. 54
4.4 Schematic representation of an on-chip tensile test structure, side view. The under-etch profile is represented as a curved edge below the "under-etch" parts of the actuator ue, a and sample "ue, s. 54
4.5 General diagram illustrating how the data reduction scheme is applied. The picture of the structure is from [47] 55
4.6 Schematic representation of the dog bone element, with key dimensions. 59
4.7 Simplification of the device's structure used as a basis for the correction model, with the α and β parameters highlighted 61
4.8 Evolution of the error made by the model of equation (4.21) as a function of the α parameter, for fixed sample size and varying actuator sizes. Case of a ductile sample. . 63
4.9 Evolution of the error made by the model of equation (4.21) as a function of the α parameter, for a fixed sample size and varying actuator sizes. Case of a brittle sample. 63
4.10 Evolution of the $\alpha_{min,i}$ parameters with the mapping h, case of a brittle material (ZnO) 64
4.11 Evolution of the $\alpha_{min,i}$ parameters with the mapping h, case of a ductile material (Pd) 65
4.12 Logarithmic plot of $\alpha_{approx}(h)$. 3 curve-fitting regimes corresponding to specific h values are highlighted. Case of a brittle material (ZnO) 65
4.13 Curve fitting model (linear regression) of $\alpha_{approx}(h)$, case of a ductile material (Pd). . 66
4.14 Evolution of the error made by the model of equation (4.26) as a function of the parameter β, for fixed sample size and varying actuator size, case of a brittle sample (ZnO) 66
4.15 Evolution of the error made by the model of equation (4.26) as a function of the parameter β,for fixed sample size and varying actuator size, case of a ductile sample (Pd) 67
4.16 Curve fitting model of $\beta_{approx}(h)$, case of a brittle material (ZnO). 68

4.17 Curve fitting model of $\beta_{approx}(h)$, case of a ductile material (Pd). 68
4.18 Simplification of the device's structure used as a basis for the correction model, with some important dimensions highlighted. 69
4.19 Stress-strain curve for brittle ZnO samples, data simulated from FE simulations. The grey data is the reference data, computed by finite element methods on the Abaqus software. The red data corresponds to the application of the scheme with the displacement correction. The blue data corresponds to the application of the scheme without the displacement correction. 70
4.20 Stress-strain curve for ductile Pd samples, data simulated from FE simulations. The grey data is the reference data, computed by finite element methods on the Abaqus software. The red data corresponds to the application of the scheme with the displacement correction. The blue data corresponds to the application of the scheme without the displacement correction. 71
4.21 Strain in different regions of the lab-on-chip device, represented as a bar plot. Plain bars indicates the result of the correction model while the hatched bar represent the reference data, case of a brittle sample 72
4.22 Strain in different regions of the lab-on-chip device, represented as a bar plot. Plain bars indicates the result of the correction model while the hatched bar represent the reference data, case of a ductile sample 73
4.23 Supposed stress state in the dog bone connected to the under-etched frame. The stress is assumed to be compressive because of the effect of the mismatch strain in the under-etched segment. 73
4.24 Graph equivalent to figure 4.21 but for different sample dimensions 74
4.25 Stress-strain curve for ZnO samples with various geometries, experimental data from R. Tuyaerts. 74
4.26 Stress-strain curve for Al samples with width, experimental data from H. Wang. Case of unaltered $\varepsilon^a_{mis.}$. 75
4.27 Stress-strain curve for Al samples with width, experimental data from H. Wang. Case of modified $\varepsilon^a_{mis.}$. For the raw data, $\varepsilon^a_{mis.} = -0.0034$, for the corrected data, $\varepsilon^a_{mis.} = -0.0032$. 75
4.28 Stress-strain curve for Al_2O_3samples. 76

5.1 Hybrid integrated III-V/Si laser fabrication using die-to-wafer bonding. The red film is made out of III-V material, GaAs or InP, while the blue substrate is silicon, a SOI substrate in this representation from [67]. 80
5.2 Schematical representation of sealed tube synthesis of GaAs, from [69] 82
5.3 Roadmap for differents categories of sustainability indicators for Si, Ge and GaAs integrated light sources 83

A.1 Band structure of Si from the pseudopotential method, from [20]. The 0 in energy is set at the top of the valence band at the Γ point in the Brillouin zone. The high symmetry points and direction have "double goup" notation on this figure. 91
A.2 Band structure in Ge along the [1 1 1] and [1 0 0] direction in the reciprocal space. From [86] 92

C.1 Global substance flow of gallium in 2011, from [71] 96
C.2 Global substance flow of germanium in 2011, from [71] 97

Contents

1 Introduction **6**

2 State of the Art **8**

2.1 Motivation: silicon and germanium based photonics 8
2.1.1 The interconnect bottleneck 8
2.1.2 Optical interconnections: a material science challenge 12
2.2 Silicon and germanium as opto-electronic materials 15
2.2.1 Crystalline structure of Si and Ge 15
2.2.2 Electronic band structure and symmetry 16
2.2.3 Accurate modelling of Si and Ge electronic band structure 17
2.2.4 Light absorption and emission in Si and Ge 21
2.3 Strain engineering in Si and Ge 25
2.3.1 Strain effects on symmetry 25
2.3.2 Strain engineering of the band gap: the Deformation Potential model 27
2.3.3 Indirect to direct band gap transition in Si and Ge 30
2.3.4 From direct band gap transition to population inversion 31
2.4 Review of strained Si and Ge opto-electronic devices 32
2.4.1 Strained Si devices 32
2.4.2 Strained Ge devices 32

3 Experimental methods **39**

3.1 Raman spectroscopy 39
3.1.1 Basics of Raman spectroscopy 39
3.1.2 Raman and strain 40
3.1.3 Raman spectroscopy applied to measure photoluminescence 41
3.2 Lab-on-chip devices 42
3.2.1 Design and concet 42
3.2.2 Mechanical analysis of lab-on-chip devices 43
3.2.3 Fabrication steps for Si lab-on-chip devices 45
3.2.4 Microfabrication processes 48

4 Development of a new data reduction scheme for lab-on-chip devices **51**

4.1 A data reduction scheme for lab-on-chip devices 52
4.2 The analytical correction model 53
4.2.1 Modelling the actuator side 54
4.2.2 Modelling the sample's side 58
4.3 Linking the model to FE predictions 61
4.3.1 Overview of the reference data 61
4.3.2 Optimisation and modelling of the α parameter 62
4.3.3 Optimisation and modelling of the β parameter 66
4.4 Final correction model and data reduction scheme 69
4.5 Results and sicussion 70
4.5.1 Application on reference data 70

4.5.2 Practical example: ZnO samples 74
4.5.3 Practical example: Al samples 74
4.5.4 Practical example: Al_2O_3 samples 76

5 Sustainability assessment of opto-electronic devices fabrication 77
5.1 Actors and industry involved in integrated opto-electronic devices fabrication 77
5.2 Scope and assumptions 79
5.3 Si, Ge and GaAs wafers industrial fabrication 80
5.4 Systemic and multidisciplinary approach to the sustainability assessment 82
5.4.1 Assessment of sustainability through indicators comparison 82
5.4.2 Indicators linked to the environmental impact of the wafer production 82
5.4.3 Indicators linked to the supply chain 83
5.4.4 Indicators linked to regulations 84
5.4.5 Indicators linked to social impact 84
5.5 Results and discussion 86

6 Conclusion 88

Appendix A Electronic band structure modelling, supplementary models 90

Appendix B Data reduction scheme: results 93

Appendix C Global substance flows 96

References 98

Chapter 1

Introduction

Strain, along with stress, forms the very basis of solid mechanics. Though strain has been studied for decades in the field of material mechanics, it has seen a recent renaissance in the field of electronics and opto-electronics as the concept of "strain engineering" emerged. When this field saw the light during the 80's in pioneer works, strain engineering of functional materials referred to the improvement of performances related to carrier transport. Nowadays, strain engineering is also applied in the fields of photonics and opto-electronics. The extension of strain engineering to photonics and opto-electronics is the driver of this master thesis. This relatively new field studies how strain can be used to engineer semiconductors like silicon and germanium to enhance, or completely alter, their opto-electronic properties. The focus of this work is the study of strain engineering as a mean to improve light emission mechanisms in silicon and germanium thin films. Such work is part of the broader scientific effort to transform indirect band gap semiconductors into direct band gap semiconductors able to exhibit the LASER effect.

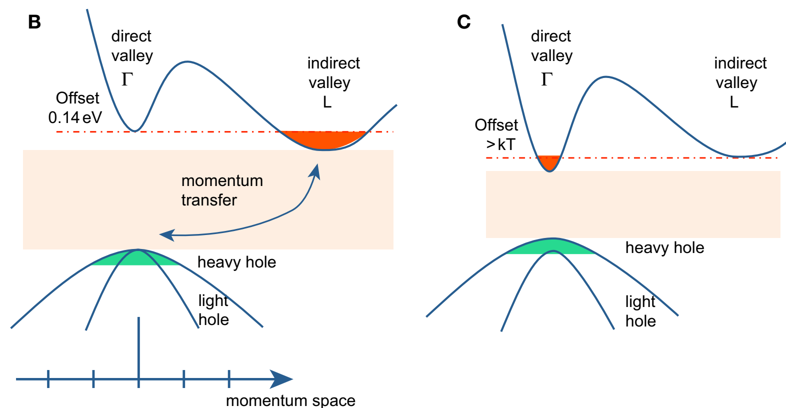

Figure 1.1: What strain engineering can (theoretically) do: transform the indirect band gap of a semiconductor like germanium into a direct band gap. From [1]

The main tools used for this study should have been the lab-on-chip devices developed at UCLouvain along with Raman spectroscopy and photoluminescence. The lab-on-chip devices' purpose would have been to induce high strain in hundreds of Si or Ge thin film samples. These devices should have been fabricated in the Winfab facilities, on the UCLouvain campus. Then, photoluminescence experiments on the strained samples should have measured the evolution of Si and Ge's band gap for strains ranging from 0 to $\approx 2\%$. The photoluminescence experiments should have been performed in a Raman spectrometer in the Welcome facilities, on the UCLouvain campus again.

The latter paragraph has been written using the "should" auxiliary. As this work began in the Winfab facilities on the UCLouvain campus, it was all of a sudden caught in the midst of the global Covid19 pandemic and its subsequent confinement measures. As the virus raged across the country, access to the clean rooms and spectroscopy equipment was prohibited, disrupting the study performed in this

Master thesis. Therefore, as the study of strain engineering in Si and Ge required both microfabrication processes and photoluminescence spectroscopy, it had to be dropped in favour of another, more "home working-friendly" study.

Consequently, the work of this Master thesis has been shifted towards the development of an upgraded data reduction scheme for on-chip tensile testing devices. Strain in thin films stays at the core of this alternative study, which focuses more on the Micro Electro Mechanical System (MEMS) used to induce strain rather than the consequence of strain on Si and Ge's bandgap. The on-chip tensile testing devices that were a mere mean to induce strain in Si or Ge samples in the initial study become the heart of this new study. The purpose of this work is to develop an analytical correction model to improve measures made on the on-chip tensile testing devices and to develop a tool to directly apply the corrections on raw data. Due to the abrupt shift in subject addressed in this master study, the state-of-the-art and a part of the experimental methods refer to the initial subject, while the core study refers to the "alternative" subject. This situation can make the structure of the work presented here a bit confusing.

Finally, this work ends on a reflection concerning the sustainability of the materials used to build integrated light emitting device. The sustainability of such materials and their processing is discussed there, on the basis of a simplified sustainability assessment. This chapter refers to the initial subject of this master thesis: strain engineering applied to Si and Ge's opto-electronic properties.

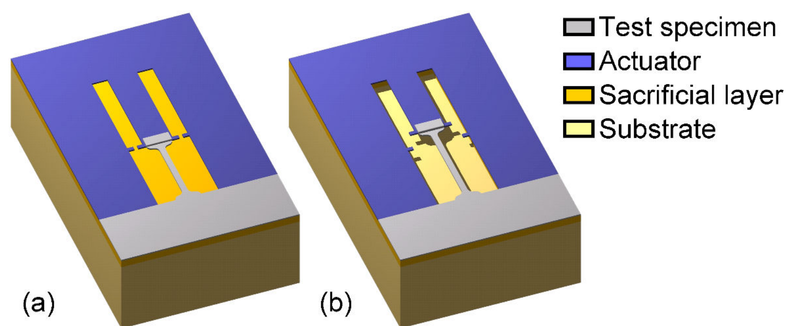

Figure 1.2: An elementary on-chip tensile testing device, a key MEMS-based device for this master thesis. From [2]

Chapter 2

State of the Art

Before delving into the experiments and simulations made in this work, a literature review of semiconductors strain engineering is introduced, along side with a motivation to pursue such a study.

2.1 Motivation: silicon and germanium based photonics

In the following section, some context and incentives towards the study of opto-electronic properties of silicon and germanium are given. Though silicon and germanium share many material properties (see section 2.2), this section focuses more on germanium than silicon. Indeed, despite both materials having been studied to create a photonic platform, germanium has seen more intense research in this domain in recent years. [3]

One of the major motivations to study the opto-electronic properties and light emission mechanisms in strained germanium stems from the field of micro-electronics. In recent years, it has been shown that the most important bottleneck for the scaling down and increase in performance of micro-electronic components comes from a concept known as the **interconnect bottleneck**. One key to solve this interconnect bottleneck would be the switch from the generic electron-based interconnections to photon-based interconnections, also called "optical interconnections". In this framework, many studies highlighted the potential of strained and doped germanium to build **optical interconnections**, which could help solve the interconnect bottleneck. [3, 4, 5, 6]

It has to be noted that optical interconnections and, in a broader sense, photonic integrated circuits, are being developed on a plethora of different material platforms. Each material platform having its advantages. As a matter of fact, silicon-based photonics are considered as one of the most mature photonic platform. [7]
Nonetheless, research on germanium photonic devices have seen a tremendous growth in the past decade, justifying the focus on germanium in the study presented here.

2.1.1 The interconnect bottleneck

The current situation

Transistors are the keystone of microelectronics. They are the smallest active device inside most integrated circuits. Improvements in transistor performances, size, has long been the most important factor behind integrated circuits performance improvement. The creation and development of MOSFET transistors is said to have "birthed" modern electronics. [8]
Today, the current trend in the microelectronic industry is to shrink the size of the transistors inside integrated circuits (ICs). This decrease of size allows for a larger transistor density on chips. Smaller transistor size and larger transistor density are both desirable parameters to build more efficient electronic devices, such as processors, GPUs, etc.

The concept of **technology nodes** is build around this size decrease trend. The technology node is expressed as a physical dimension, ranging from μm to nm. Historically, this dimension expressed the gate length[1] in a MOSFET[2]-type transistor, as shown on figure Figure 2.1.
Nowadays, the technology node now refers to the manufacturing process behind the chip: a smaller technology node usually means that the fabrication process is more recent and that the chip packs more efficient transistors/a higher transistor density. [9]

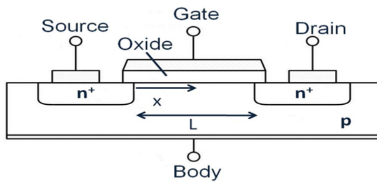

Figure 2.1: Schematic drawing of a MOSFET transistor, where the dimension L designates the gate length.

Performance increase between two technology node is not trivial to quantify. A modern example of performance improvement using a smaller technology node would be the one between the TSMC[3]'s 16nm (2016) and recent (2019) 7nm processors. TSMC claims that, for instance, the 7nm-based CPU offers a 65% power reduction, at the same CPU speed, than the 22nm one. The decrease in size of technology nodes used to be the answer to the requirement of **Moore's law**: doubling the number of transistors on an integrated chip every two years. However, such a decrease in size is not sustainable, as certain physical limitations are starting to hinder the system. [10]

The bottleneck

The major physical limitation to the further decrease in size of transistors stems from the interconnections inside an integrated circuit. It is known as the "Interconnect Bottleneck".

Interconnections (or *interconnects*) are the equivalent of electrical cables, connecting components inside integrated circuits. Transistors are connected together thanks to these interconnects. Interconnections exist on different scales. For instance, interconnection between transistors are said to be "*on-chip*" interconnects, whereas interconnection between chips are said to be "*off-chip*". Connections between distinct chips in multi-core CPUs are an example of "*off-chip*" interconnects. Conventional, modern, *on-chip* interconnects are made from a Cu-low κ layered material. A typical CMOS[4] chip structure is shown on figure Figure 2.2.
Both the *"on"* and *"off"* interconnect scales contributes to the interconnect bottleneck.

On-chip interconnects had to go down in size side-by-side with transistors. Whereas the decrease in size was beneficial to transistor performances, the performances of interconnects collapsed.
As interconnect cross-sections approached 40nm in diameter, surface effects in the Cu wires began to appear and increased their resistivity.
At the 22nm technology node, resistivity in the wires is **4x the resistivity of bulk Cu**. A rise in resistivity in the interconnects causes a catastrophic increase in latency and power consumption for the integrated circuits. [5]

At the same time, the shift toward multi-core architecture in integrated circuits puts pressure on *off-chip* interconnects to be able to connect the cores at high bit rates. Current design using Cu-low κ wires will cause a rise in latency. [5]

The drop in performance of Cu-low κ interconnects with decreasing size at the on-chip scale, coupled

[1] When Intel's MOSFET transistors gate length reached 45nm, the meaning of technology node lost its original sense. Now the technology node, such as today's 10nm or 7nm nodes, only refers to the transistor manufacturing process. [9]
[2] Metal Oxyde Semiconductor Field-Effect Transistor. Most common type of transistor found in today's integrated chips.
[3] Taiwan Semiconductor Manufacturing Company, one of the 4 current leaders in the chip manufacturing.
[4] Complementary Metal Oxyde Semiconductor. It refers to a MOSFET transistor manufacturing process.

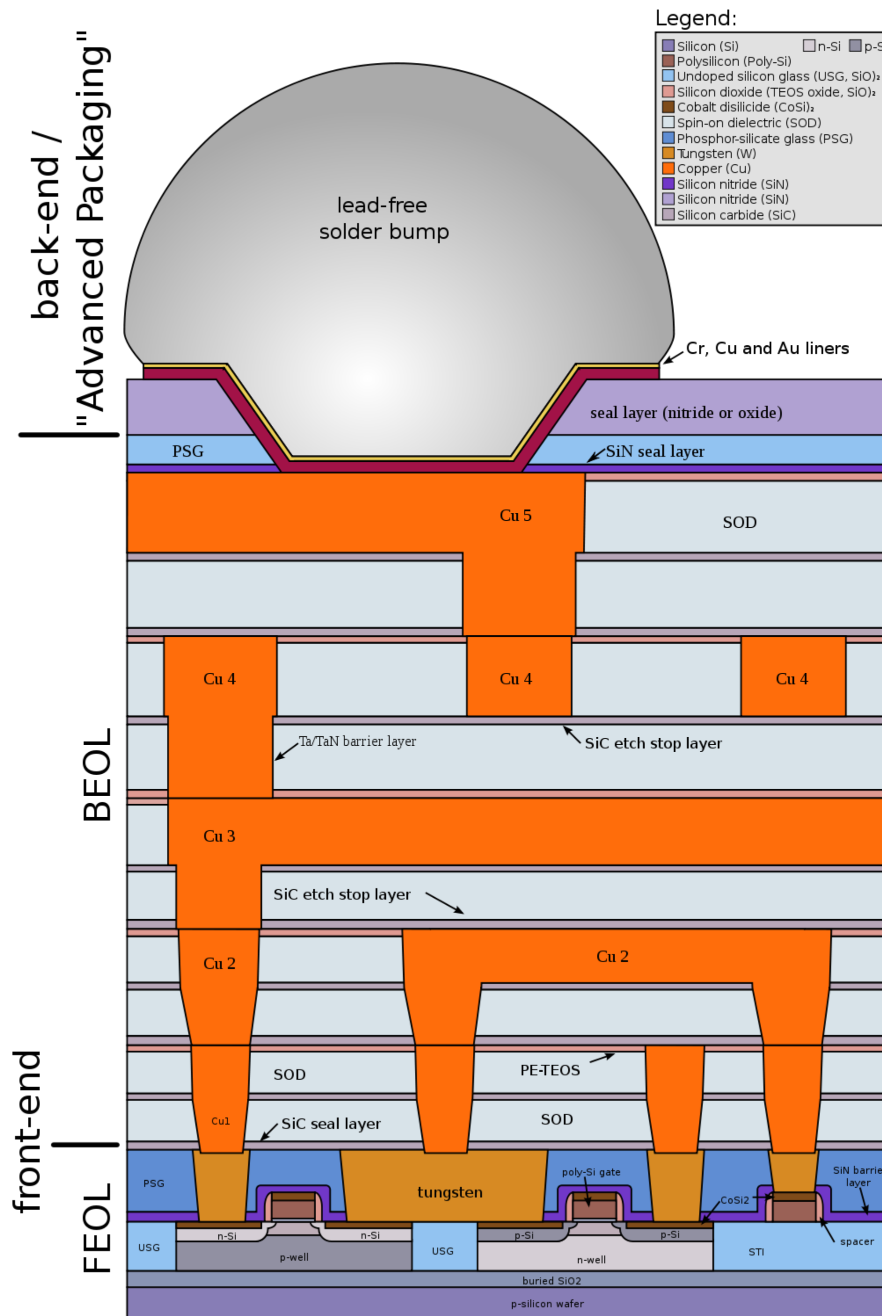

Figure 2.2: Typical CMOS chip structure. The transistors are on the bottom of the structure. Interconnects are the orange channels above the transistors. From [11]

with the demand for higher bit rates connection at the off-chip scale, drives research to find new interconnect materials or architectures.

Solutions to the interconnect bottleneck

From a material science point of view, there are two solutions to the interconnect bottleneck being researched nowadays:

- The use of materials that are more competitive at the nano-scale.
- Shifting from electrical to optical interconnection.

Materials that are more competitive at the nanoscale are, for instance Carbon Nanotubes (CNTs). Optical interconnections are a complete shift from the current architecture of electronic integrated

circuits. A schematic example of optical interconnect design is shown on figure Figure 2.6. Optical interconnection require the use and engineering of specific materials, like Si or Ge, which is the topic of this master thesis. [5, 6]

The graphs on figures Figure 2.4 and Figure 2.3 display the comparison between CNTs, optical interconnects and standard Cu-low κ interconnects, as an evolution with the technology node. Table Table 2.1 sums up this comparison and highlights which interconnect technology is the best in different scenarios. The data on the two graphs comes from theoretical simulation done by *Saraswat et Al. (2008)* and should be taken with a grain of salt, as they are only theoretical and already outdated. [5]

	Interconnect length $\leq 1mm$(on-chip)	**Interconnect length** $\geq 10mm$ (on-chip)	**Interconnect length** $\geq 10mm$ (off-chip)
Power consumption	no data	no data	Optical interconnects
Energy per bit	CNT	Optical interconnect	no data
Latency	Optical interconnect	Optical interconnect	no data

Table 2.1: Best technology for interconnects, according to the power consumption, energy per bit and latency metrics. Comparison between Carbon Nanotubes (CNT), optical and standard Cu-low κ interconnections at the on-chip and off-chip scales. From [5]

In sum, the data provided by *Saraswat et Al. (2008)* highlight optical interconnects as strong candidate to solve the interconnect bottleneck, given that:

- For interconnects length of more than $10mm$ (on-chip scale) optical interconnections are 2 to 3 times better than CNTs or standard Cu-low κ interconnects.
- For interconnects length of 1mm (on-chip scale), optical interconnect still offer slightly better lantecy performance though the energy required per bit is almost 4 times higher than CNTs and Cu-low κ interconnects.
- For the off-chip scale, the improvement in power consumption versus length is considerable for length past the critical length, as shown in figure Figure 2.5.

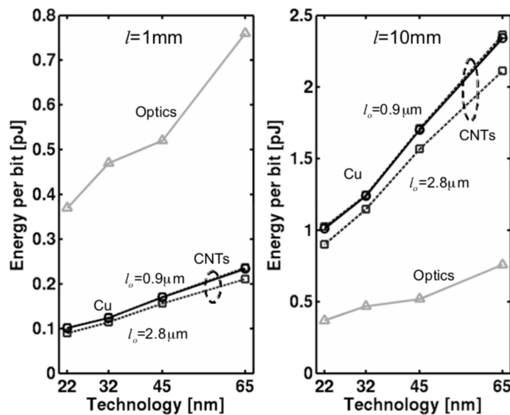

Figure 2.3: Energy required per bit of data versus *on-chip* interconnect length, from [5]

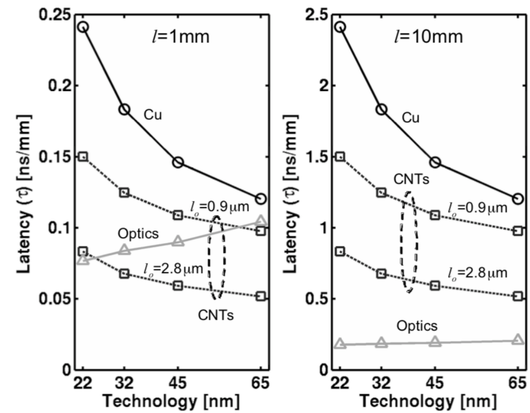

Figure 2.4: Latency versus *on-chip* interconnect length, from [5]

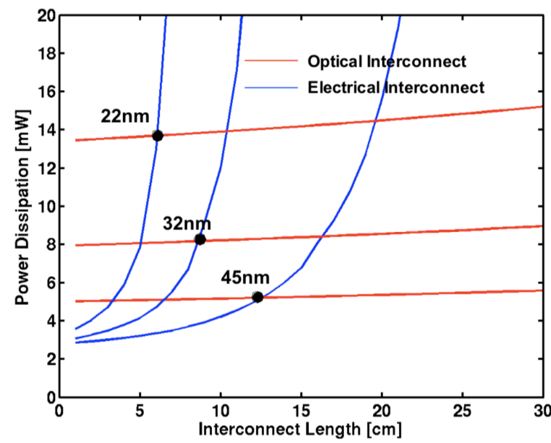

Figure 2.5: Power consumption versus *off-chip* interconnect length, for different technology nodes. The crossing between optical and electrical interconnect curve is called the critical length. From [5]

2.1.2 Optical interconnections: a material science challenge

The previous section highlighted the potential of optical interconnect to solve the interconnect bottleneck. However, they also come with many challenges. From a material engineering point of view, they come in two forms: challenges linked to the material's functionalisation (ie: engineering a material for light emission, passive transmission,...) and challenges linked to the manufacture of the device. The most crucial challenge being the creation of a convenient light source, an **integrated LASER light source**.

Indeed, because they are integrated in a microelectronic environment, optical interconnections require the use of very specific materials. Firstly, the materials need to be able to emit, transport and sense light. At the same time, they have to be compatible with: **i)** microfabrication processes, **ii)** other materials involved in the device and finally **iii)** the environment where the device will be used. To illustrate the complexity of the situation, a diagram of an optical interconnection is drawn on Figure 2.6. On this figure, one can see that the optical interconnection is made out of a mix of various optical and electronic devices at the micro/nano-scale. The components of interest here are the optical components, namely: the light source, modulator, optical waveguide and photodetector (in yellow on Figure 2.6). The components are described on Table 2.2, alongside their respective challenges and the current functionnal materials they are made from. For the sake of comparison, electrical interconnect only require a copper line, insulated in a low κ dielectric

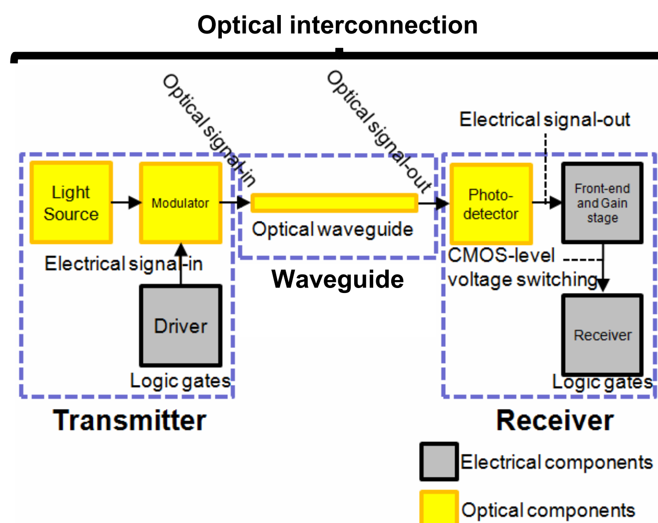

Figure 2.6: Schematic diagram of an on-chip optical interconnect. Modified diagram from [12]

Components	Function	Challenges	Candidates	Sources
Light source	- LASER light source	- Sustain a net positive optical gain - Emission of light in mid-IR wavelengths [5]	- III-V materials: GaAs, InP - Si : porous Si, erbium doped Si,.. - Ge : Strained Ge, GeSn	[3, 4]
Modulator	- Conversion of electrical signals into optical signals by modulating a light source	- Fast optical modulation - Current generation modulators are too chunky - Lower the heat generation	- Si, Ge, SiGe	[3]
Waveguide	- Controlled propagation of optical signal	- Transparent to mid-IR wavelength - High optical confinement and low optical losses	- Si, SiGe - Polymers: epoxy - Glass materials: phosphate glass, chalcogenide glass	[3, 13]
Detector	- Conversion of optical signal back to electrical signal	- Technology is already considered mature for this kind of application	- III-V materials: InP - Ge	[3, 14]

Table 2.2: Description of the components inside an optical interconnection, with their associates challenges and the current materials that are made from.

From the list of components and candidate materials in Table 2.2, one could ask what are the best materials to build optical interconnections with. This section will try and answer that question.

Some materials listed in Table 2.2 can be removed thanks to a single consideration: for an easy and scalable fabrication, **the materials have to be compatible with standard silicon chip fabrication processes**. This condition already removes materials such as glasses and, to an extent, polymers from the list. III-V materials however, are still considered as potential materials for the light source, even though they are chemically incompatible with Si. This is due to the technological maturity of the III-V integrated lasers and the silicon fabrication processes. Indeed, hybrid integration of III-V devices on silicon substrates is already a commercial feature, despite their chemical incompatibility.

Furthermore, the **monolithic**[6] **integration** of optoelectronics and electronics within a single chip is seen as the "holy grail" in silicon photonics. However, monolithic integration requires the use of materials that are compatible with each others. With this consideration in mind, III-V materials have to be ditched as they are chemically incompatible with Si and require hybrid integration. Monolithic integration of optical interconnection consequently require Si or Ge to be used as active materials.

Even though **silicon-based photonics** have been the most studied platform, some challenges have remained unsolved. Briefly, the challenging elements for silicon photonics are silicon light emitters and silicon waveguides. The development of a silicon laser light source has been the toughest challenge in Si photonics, because the lack of sufficient gain to exceed material loss in Si hinders the development of any Si-based light sources.

The recent interest towards **germanium as a material for optical interconnection** applications stems from its potential to surpass silicon's limitations. Indeed, germanium possesses many interesting opto-electronical properties. Ge is a semiconductor closely related to Si, to the point where Ge is considered to be CMOS compatible. CMOS compatibility means that germanium can easily be dealt with using

[5] for easy integration in larger integrated optoelectronic systems using fiber optics

[6] *Monolithic integration is a technique that allows both the electronics and the optical devices to be integrated in a common semiconductor material in a single growth process or by utilizing a re-growth technique*, definition from [15]

microfabrication techniques similar to silicon. However, The semi conducting behavior of Ge is slightly different than silicon, especially its band structure. This is precisely this slight differences in band structure between Si and Ge that is driving the research around Ge-based opto-electronic devices. The most important feature that stems out of this, is **the potential of Ge to be used as a laser device**.

Finally, the potential of Ge as a material of choice for optical interconnection is illustrated in Table 2.3, where Ge-based photonic devices are presented. Figure 2.7 depicts a functionnal optical interconnection where every device except the light source is made from Ge, Si and SiGe. This device was realized as a proof of concept. More will be said about Ge and Si-based photonic device in section 2.4.

Components	Function	Challenges	Germanium-based devices	Sources
Light source	- LASER light source	- Sustain a net positive optical gain - Emission of light in mid-IR wavelengths	- LASER effect has been shown in GeSn alloy. -The indirect band gap of Ge can be turned to a direct bang gap through strain engineering.	[4]
Modulator	- Conversion of electrical signals into optical signals by modulating a light source	- Fast optical modulation - Current generation modulators are too chunky - Lower the heat generation	-High performance Multiple Quantum Well (MQW) Ge/SiGe modulator have been fabricated in tandem with a Ge/SiGe photodetector, see Figure 2.7	[3]
Waveguide	- Controlled propagation of optical signal	- Transparent to mid-IR wavelength - High optical confinement and low optical losses	-Ge is already being added to Si to create SiGe optical channels	[3]
Detector	- Conversion of optical signal back to electrical signal	-	-Ge photodetectors are technologically mature	[3]

Table 2.3: Application of germanium-based devices for optical interconnection.

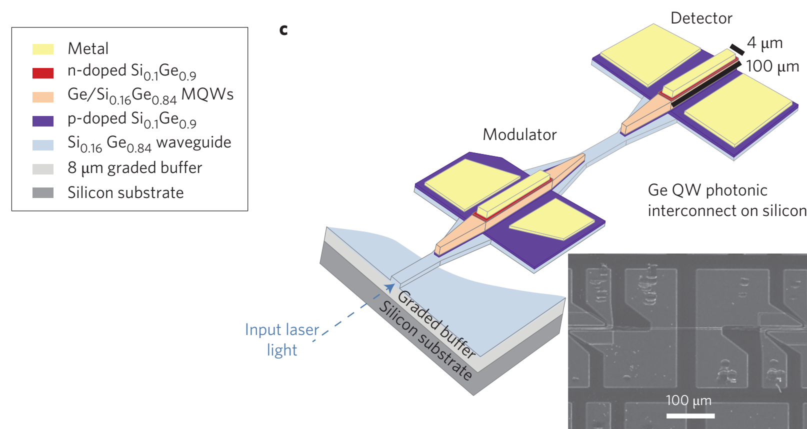

Figure 2.7: Photonic interconnect: SiGe waveguide and Ge/SiGe active MQW modulator and photodetector, from [16]

2.2 Silicon and germanium as opto-electronic materials

Both silicon and germanium are candidate to become the choice material for optical interconnections. The advantages of germanium for that particular application have been listed in the previous section. In this section, the theoretical background of opto-electronic properties in silicon and germanium are presented. The presentation of those opto-electronic properties pave the way for this master thesis's focal point: the band gap engineering of Si and Ge.

2.2.1 Crystalline structure of Si and Ge

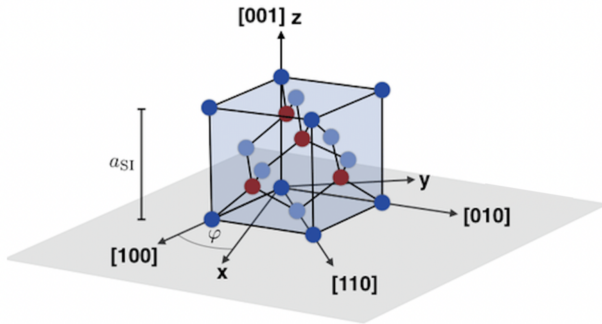

Figure 2.8: Diamond cubic crystal structure of Si and Ge, along with the [1 0 0], [0 0 1], [0 1 0] and [1 1 0] crystalline direction. From [17]

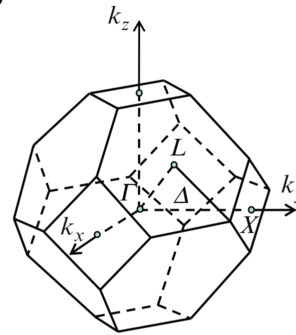

Figure 2.9: First Brillouin zone for a FCC lattice. Corresponds to the Brillouin zone used to describe semiconductor with the diamond cubic crystal structure, from [18].

The main reason why silicon and germanium share so many properties stems from their identical crystalline structure.
Silicon and germanium both belong to the cubic crystal system. They exhibit the **diamond** (octahedron) **symmetry**. The diamond crystal structure is shown on figure Figure 2.8. The diamond system possess 48 symmetry operations.

The **symmetry operations** in the crystalline structure of a semiconductor are critical for the understanding of semiconductors electronic band structure.
For instance, the electronic band structure model called the *The Nearly Free Electron Energy Bands* is build around the symmetry operations in a crystalline semiconductor. This model is described for Si and Ge in section section 2.2.3. Symmetry operations in the lattice can also explain some of the effects of strain on the electronic band structure (degeneracy lifting for instance).

Reciprocal space

The electronic band structures, introduced next, are based on the **reciprocal space** of the material's **lattice**. Usually, the reciprocal space of a cubic semiconductor is represented in the Brillouin zone. The first Brillouin zone of a cubic semiconductor is shown on figure Figure 2.9.
Important points in the first Brillouin zone are the Γ, X and L point. The Γ point represent the center of the Brillouin zone, with wave vector (0,0,0). The X and L points corresponds to the wave vectors with coordinates $\frac{2\pi}{a}(0\ 1\ 0)$ and $\frac{2\pi}{a}(0\ 0\ 1)$, where a is the lattice constant. These are **high symmetry points**. The Δ and Λ directions respectively link the Γ point to the L and X points.

Symmetry in the recirpocal space

Symmetry of crystal *systems*[7] is preserved between the direct and reciprocal space.
For instance, the Brillouin zone of cubic crystals (Ge, Si, GaAs), no matter the crystal *class*[8], has the same cubic symmetry.

Reciprocal space, *crystal systems*, *Brillouin zone* and *high symmetry points* are crucial concepts for the next topic, the electronic band structure. Indeed, electronic band structures are represented in $E-k$ diagram, where the k dimension refers to the first Brillouin zone in the reciprocal space.

2.2.2 Electronic band structure and symmetry

Electronic band structure theory is crucial for this master thesis. Tuning the opto electronic properties in Si and Ge through mechanical strain lies on the behaviour of electronic band structures.

Band structures scope and limitation

The electronic band structure theory is useful to describe semiconductors, as their electronic and optical properties can be well described by the behavior of their valence electrons around the band gap. However, the band structure theory has its limitations: it assumes infinite dimensions and homogeneous composition, it is therefore not applicable when surface and interface effects comes into play, as well as for small systems (small molecule or quantum dot) where bandstructure loses its continuity. Furthermore, the main models do not take dynamic electron-electron interactions into account, which can make band structure theory not applicable for strongly correlated materials. [19]

Band structure representation in $k-$space

In solids, the electronic band structure refers to the allowed energy states of the electrons inside a solid, where the electrons can only have energy state comprised inside a certain range. The range of allowed energy states for electrons are called *energy bands*, while the range of forbidden energy states are called *bandgaps*. The range of allowed and forbidden energy state is dependant on the electron energy and position k in the reciprocal space of the semiconductor's crystalline structure.

Band structure are represented in a diagram of energy and position in the reciprocal space because many of the band structure properties are dependant on symmetry operations in the reciprocal (k-)space of the crystal lattice. This dependances emerges from the fact that electronic wave functions are restricted by the periodicity of a crystal. Indeed, in a crystal, translational symmetry dictates the electronic wave functions in a crystal to be Bloch waves and Bloch waves are modulated by periodic functions $u_k(r)$ whose periodicity follows the crystal periodicity.
Equation Equation 2.1 represents the Bloch function $\phi_k(r)$, where r is a point in the reciprocal lattice.In a crystal, the periodicity condition is expressed as equation Equation 2.2, where R is a vector that is a multiple of the lattice's basis vector.

$$\phi_k(r) = u_k(r)e^{ik\ \cdot\ r} \qquad (2.1) \qquad\qquad u_k(r) = u_k(r+R) \qquad (2.2)$$

As said a in the previous paragraph, symmetry of crystal systems is preserved between direct and reciprocal space. Therefore, combining this statement with the periodicity condition of the electronic wave function, the following statement can be made: crystals with the same *lattice symmetry* have band structures with the same symmetry.
This results in many properties of semiconductors being dictated by their lattice symmetry. As crystal systems are based on the lattice symmetry, semiconductors which belong to the same crystal system will exhibit some similar essential common properties. As a matter of fact, this is

[7] Crystal system are a classification of **lattice** point symmetry
[8] Crystal classes are a classification of **crystals** using their point symmetry, for instance: the tetrahedron (GaAs) or octahedron (Ge,Si) crystal point groups

the case for Ge, Si and GaAs, which belong to the cubic crystal system. Those "cubic" semiconductors exhibit many similarities in the degeneracy of their bands and how they are affected by strain. [18]

Thus, band structure are represented on energy-wavevector ($E - k$) diagrams. An example of $E - k$ diagram is given on figure Figure A.1 for germanium. In the $E - k$ diagram, valence and conduction bands extend around the center of the Brillouin zone, the Γ point. They extend from the Γ point to the high-symmetry points of the first Brillouin zone, the L and X point, through the Δ and Λ directions.

Modeling the band structure through symmetry only: the Nearly Free Electron Energy Bands

This model uses knowledge of symmetry operations in the crystalline lattice of the studied semiconductor to build band structure. The electronic states are classified solely by symmetry properties of the lattice. The band structure revolves around an approximation of the electronic potential $V(r)$ only determined by symmetry and neglects the perturbation of the atoms to the potential. Thus, the NFE model is limited as it cannot differenciate between materials that belong to the same crystalline system (like Si, Ge and GaAs who belong to the cubic crystal system).[18]

In the Nearly Free Electron Energy Bands (NFE), the assumption is made that electrons can move nearly freely through the crystal lattice. It is slightly different from the free electron models in metals, where electrons were assumed to move without any interaction from the lattice. By adding the slight periodic potential from the ions in the lattice, the band structure will change dramatically according to the symmetry characteristics of the material.

In quantum mechanics, wavefunctions are used to describe the electron configuration of atoms. The behavior of electrons in solid-state physics is best described using wavefunctions, using the Schrödinger equation for electron in different conditions. Here, the conditions imposed on the electron is that they are slightly influenced by the periodic potential, emerging from the ions in the crystal lattice. [20]
To determine the band structure, the electrons behavior in those conditions have to be described. This is done by solving the single electron Schrödinger equation:

$$\mathcal{H}\phi_n(r) = \left(\frac{p^2}{2m} + V(r)\right)\phi_n(r) = E_n\phi_n(r) \tag{2.3}$$

Where $V(r)$ is the **effective crystal potential**, $\mathcal{H}_{1e}$ is the electron Hamiltonian, $\phi_n(r)$ the wavefunction of an electron and E_n, its energy.
As the solutions of equation Equation 2.3 have their symmetry defined by $V(r)$, the trick used in the NFE is to develop an expression of the potential $V(r)$ trough group theory. As a result, the effective crystal potential $V(r)$ described by group theory is essentially determined by the crystal symmetry. Therefore, the solutions of the Schrödinger equation, that results in the band structure, are symmetry-determined. [18]

This leads to the band structure shown in figure Figure 2.10. The bands curvatures between points of high symmetry are similar to true bands, however, at the point of high symmetry in the first Brillouin zone, real bands split and form bandgaps[9].

2.2.3 Accurate modelling of Si and Ge electronic band structure

A symmetry-based model is not good enough to describe a semiconductor's band structure. Distinction between semiconductor in the same crystal class is impossible and band gap don't appear. Here, a more accurate way of modelling the band structure is presented. Next section will cover the modification of band structures through the introduction of mechanical strain.

[9]Indeed, electrons interfers the most when their wavelength matches with the crystal lattice wavelength. [21].

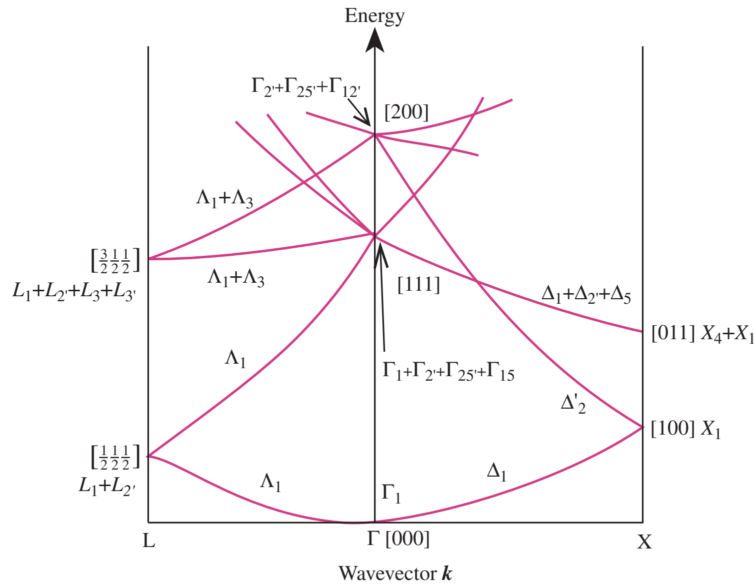

Figure 2.10: Band structure of nearly free electrons for Germanium. The band structure is only shown between the points of high symmetry L, Γ, X, κ in the first Brillouin zone of a diamond crystal structure. From [20]

One "accurate" model that is extensively used in the field of strain engineering of semi conductors is the Tight Binding model. This model can be used to draw precise band structure for semiconductors but also to describe their strain-induced modifications. The Tight-Binding model is presented next. Some other accurate models can be found in the appendix chapter A, namely the Pseudopotential method and the $k \cdot p$ method.

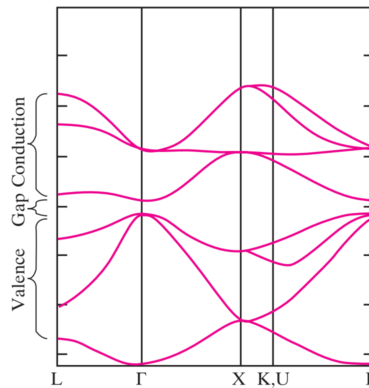

Figure 2.11: Band structure of Ge with the Tigh-Binding model, from [20].

Molecular Orbital Theory

Molecular Orbital Theory (MOT) is a good introduction to the Tight-Binding method. In chemistry, MOT is used to describe molecular and atomic bonds using the molecule's electronic structure.
Molecular Orbital Theory, together with Pauli's exclusion principle, states that two atoms brought together will behave as two potential well, each having some energy ϵ_0 and wavefunction $\psi_1(x)$ and $\psi_2(x)$. By bringing those potential well together, their energies will split and two new states will be created, one with energy $\epsilon_- = \epsilon_0 - \Delta$ and state $\psi_+ = \frac{1}{\sqrt{2}}(\psi_1 - \psi_2)$, the other one with energy $\epsilon_+ = \epsilon_0 + \Delta$ and state $\psi_- = \frac{1}{\sqrt{2}}(\psi_1 + \psi_2)$[10]. Similarly, when two hydrogen are brought together, each

[10] The *amount* of energy change Δ between the single-atom orbital and the bonding and anti-bonding orbitals are determined by the interaction Hamiltonian H. The full description of the interaction Hamiltonian and its application on Molecular Orbital Theory will not be discussed here.

having 2 $1s$ orbitals (one for each spin state), with energy ϵ_0, they form two higher energy states and two lower energy states. The higher energy states becomes the anti-bonding orbitals, while the lower energy states forms the bonding orbitals. This forms a σ atomic bond. In the hydrogen example, the two atoms have 2 electrons, which will fill the bonding orbital, as this configuration lowers the total energy of the system, forming the H_2 molecule, as shown on figure Figure 2.12. This is the basis of a covalent bond.
The same process occurs for $1p, 2s, 2p, ..$ orbitals, as shown on figures Figure 2.13.

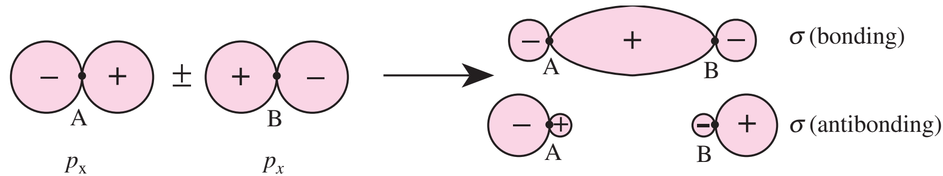

Figure 2.13: Overlap of the p_x orbitals, forming a bonding and antibonding σ orbitals, from [20]. p_y and p_z orbital overlap perpendiculary to the direction of the bond, forming π orbitals

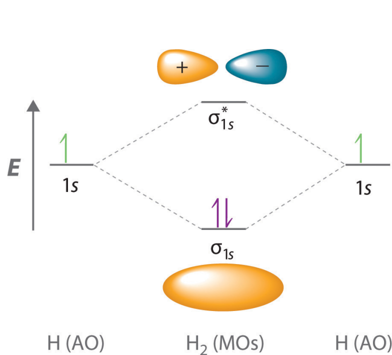

Figure 2.12: Result of the molecular orbital bonding in the H_2 molecule. The bonding orbital is the σ_{1s} and is filled with two electrons, from [22].

This theory can be extended to any type of atom combination[11] and to crystals composed of a number N of atoms. The extension to crystals is based on the approximation that the orbitals of each atom in the crystal overlap **only** with the orbitals of their direct neighbors, which is reasonable for most solids.
The results of that extension to crystals is that the bonding and anti-bonding orbitals are multiplied, as many neighbouring atoms' orbitals interact together, to the point where the discrete energy levels of the bonding and anti-bonding orbitals turn into **bands**. This broadening of the discrete energy levels to bands is illustrated on the figure Figure 2.14. On this figure, it can be seen that bonding orbitals turn into valence band and anti bonding orbitals turn into conduction band. It is not representative of every crystal's band structure, as sometimes valence bonds are formed from antibonding orbitals, conduction band from bonding orbitals,... etc. It strongly depends on the electronic configuration of the material.

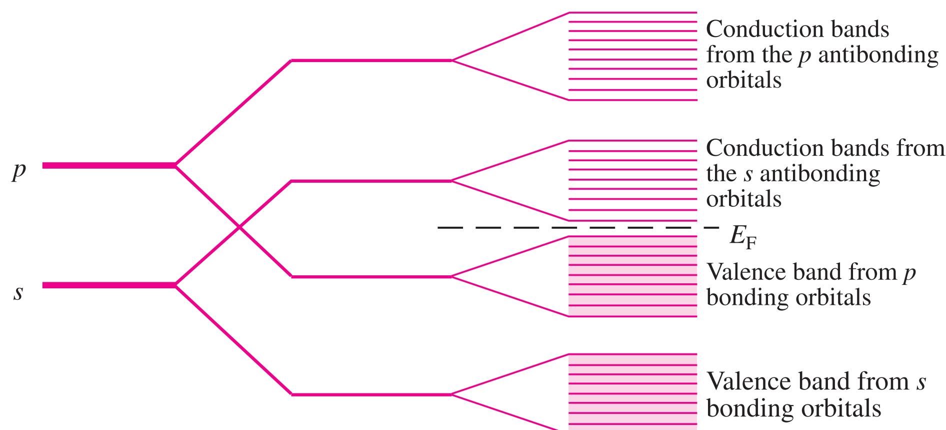

Figure 2.14: Evolution of s and p atomic orbitals into valence and conduction bands, in the case of a semiconductor, from [20]. $E_f = \epsilon_f$ is the Fermi energy in the crystal.

[11] If we consider ionic and metallic bonds to be "extreme" cases of covalent bonds, with varying binding strength of the electrons and atoms, but still following the same bonding and antibonding orbitals mechanisms. This might be a broad approximation, but it is commonly used to describe semiconductors. [23, 20]

Although simplified, the representation appearing in figure Figure 2.14 is useful to describe some important characteristics of intrinsic semiconductors, like pure germanium and silicon.
One of such characteristic is related to the Fermi level ($E_f = \epsilon_f$, notation may vary) in the crystal. If the Fermi level is **inside** a band, then it is easy to move electron in excited states, since these states are "allowed". However, if the Fermi level is **in between** two bands, then more energy is required to move electrons to an excited state, since the closest excited states are forbidden. In those materials, the band below the Fermi level is the valence band, the band above is the conduction band.
Materials with a Fermi energy inside the bandgap are insulators and semiconductors (if the bandgap is around $1eV$)[12].
Fermi distribution can also be applied to describe the population of excited electrons and valence holes in their respective band. Thus, some other characteristics of semiconductors can be derived from this simple representation, such as the modification of charge carrier occupation, with the adding of impurities (doping) and some of its effects (increased electric conduction,..).

This approach is the basis of the **Tight-Binding** method. The main result of this concept is the 1D representation of the band structure, shown in figure Figure 2.14. From this 1D representation, distinction between metals, semiconductors and insulators can be made. Alongside the band structure of figure Figure 2.14, some other interesting conclusions about semiconductor behavior can be drawn, such as the possibility of doping semiconductors.
However, real and rigorous band structures are not represented in 1D, like they are in this model, as they depend on the crystal orientation. They are represented in $E - k$ diagrams. Next paragraph develops the Tight-Binding approach to energy bands, a complete model of band structures, which is built on the Molecular Orbital Theory.

The Tight-Binding approach to energy bands

The fundamentals of the tight binding approach have been explained through the Molecular Orbital Theory approach of band structure. Now, the quantitative calculation of the electronic band structure is made using the Method of Linear Atomic Orbitals (LCAO).
In this approach, atoms are brought together, to the point where their separation becomes comparable to the lattice constant in solids, their wave function will overlap. Then, electronic wave function will be approximated by linear combination of those atomic wave functions. This approach is the opposite of the Nearly Free Electrons point of view, where electrons only had a slight influence from the atoms in the lattice.
This model assumes that a linear combination of atomic orbitals $\phi_n(r)$ is a good approximation of the time-independent, single electron, Schrödinger equation:

$$\Psi(r) = \sum_{n,R} b_{n,R} \phi_n r - R \tag{2.4}$$

Where indexes n and R refers to atomic energy levels and R to an atomic site. $\Psi(r)$ is the electron wavefunction, expressed in terms of atomic orbitals. [19]
In such a model, the Schrödinger equation is not used to describe the electron behavior, only its solution is approximated by the linear combination of atomic orbitals. This differentiates it with the NFE approach and the pseudopotential method for electronic band structure, where the Schrödinger equation is used through some simplifications.

The use of such a model allows to draw the band structure for germanium, presented in figure Figure 2.11. This model has a few shortcomings: overlap parameters are necessary for more accuracy and, in figure Figure 2.11, only four conduction bands are shown. To show more conduction bands, additionnal orbitals[13] and overlap parameters are required but this causes the model to become much

[12] If the bandgap is $\approx 1eV$, thermal excitation at room temperature is sufficient to excite a non-negligible number of electrons to the base of the conduction band, drawing the line between insulator and semiconductors. [23]
[13] In the figure Figure 2.11 from [20], only $4s$ and p orbitals are taken into account.

more complicated. However, if the wish is to study the behavior of semiconductors around their bandgap, this model should work fine.

2.2.4 Light absorption and emission in Si and Ge

Creating a LASER light source from silicon or germanium has been highlighted as the motivation to study the opto-electronic properties of strained semiconductors. Furthermore, the experimental work carried out as part of this master thesis planned to study germanium and silicon's indirect band gap shift with uniaxial tensile strain. This shift is measured through photoluminescence experiments. Within this framework, this section will give a basic review of light emission mechanisms in Si and Ge.

As shown on the electronic band structures, Figure A.1 for Si and Figure 2.11 for Ge, both of these semiconductors exhibit an **indirect** band gap.
The size and indirect character of Si and Ge's bandgap are critical features for their optical properties, as light absorption and emission are band-to-band recombination mechanism.
Light absorption and emission in Si are represented in a schematic way in Figure 2.15.
Band gaps of Si and Ge, measured between different points in the $E-k$ diagram, are given in Table 2.4

	Ge	Si
E_0^{Γ}	0.796	4.09
E_i^{L}	**0.655**	1.930
E_i^{Δ}	0.900	**1.120**

Table 2.4: Band gaps in Si and Ge measure at different locations. E_0^{Γ} is the direct band gap, E_i^{Δ} and E_i^{Δ} are the indirect band gaps. When talking about the band gap of silicon, it refers to the E_i^{Δ} and for germanium, E_i^{L} . From [24]

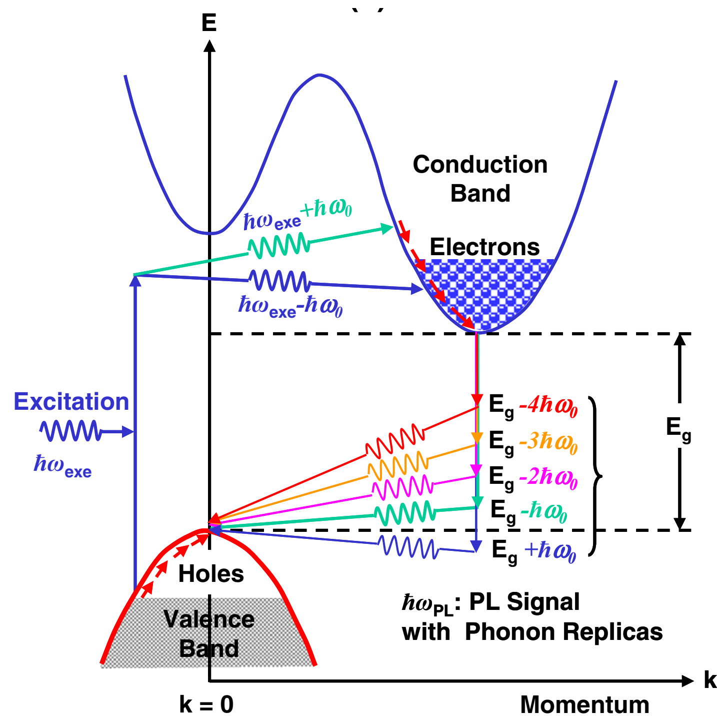

Figure 2.15: Schematic representation of recombination mechanisms in Si, absorption and phonon-associated emission. E_g is the indirect band gap in this figure (in eV). From [25]

Light absorption involves an incident photon exciting an electron from a valence state to a state inside the conduction band.
The right part of figure Figure 2.16 shows the absorption coefficient versus the incident light energy in silicon. The absorption begins at $1.12eV$, the indirect band gap of Si at 300K. The peaks in absorption at energy E_1 and E_2 arises from the parralelism[14] between the conduction and valence bands at the E_1 and E_2 points, shown on the left part of figureFigure 2.16. Absorption in germanium is similar, the only notable differences being the band gap size and location in reciprocal space.

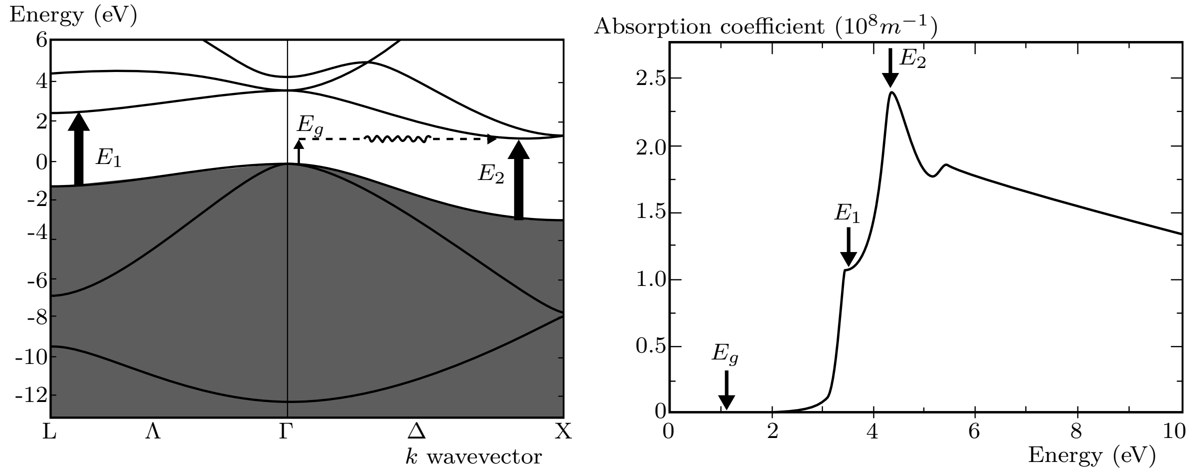

Figure 2.16: **Left:** Bandgaps in Si, E_2 denotes the position of the indirect band gap with the lowest transition energy (Δ valley). E_1 represents the second indirect band gap with transition energy lower than the direct band gap E_g. **Right:** Absorption coefficient in Si. The peaks in absorption coincide with the transition energy of the E_2 and E_1 indirect bandgaps. From [26]

Light emission involves the recombination between an electron in an excited state inside the conduction band and a hole in the valence band.
In direct band gap materials, electrons sitting in the direct conduction valley recombine with holes in the valence band peak, directly below. In semiconductors with band gap $> 0.5eV$, the assumption is made that the direct recombination mechanism is radiative (emits a photon).
In indirect band gap materials, the recombination also involves the emission or absorption of a phonon. Without a phonon, the indirect recombination process would violate the conservation of crystalline momentum k. This mechanism is shown on figure Figure 2.15. The indirect recombination is much slower than the direct one. It is therefore in competition with non-radiative recombination processes. This means that silicon and germanium have low luminescence intensity. [26]

A comparison between Ge and a direct band gap material (InGaAs) is drawn on figure Figure 2.17, where electrons are injected in the conduction bands of Ge and InGaAs. Two important light emission mechanism in silicon and germanium are the photoluminescence and the LASER effect. They are described in the next paragraphs.

Photoluminescence

Photoluminescence occurs when electrons are being continuously excited (*pumped*) in the conduction band by an incident light source, such as a laser with wavelength ω_{exe}, as represented in figure Figure 2.15.
Once the electrons have been excited, they relax to the bottom of the conduction band, the L valley in Ge and the Δ valley in Si, through non-radiative mechanisms (phonon emission).

[14] High absorption occurs when valence and conduction bands are parallel because of the Joint Density of States behavior. If the occupied and unoccupied bands are parrallel, the JDOS will be large, resulting in high absorption. [26].

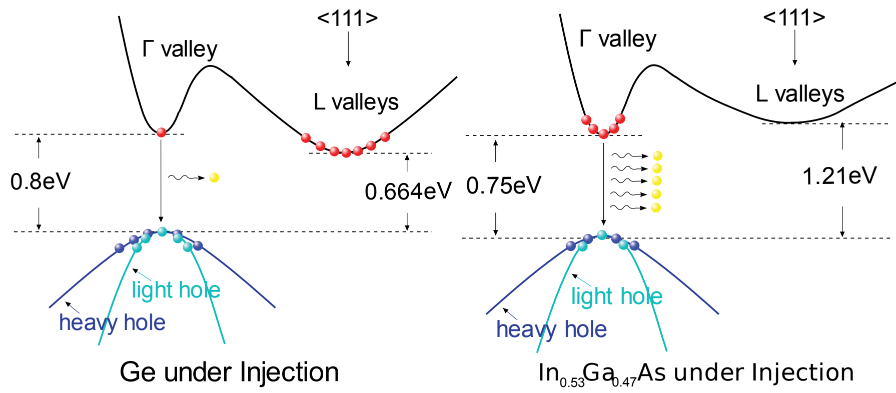

Figure 2.17: Comparison of carrier distribution and light emission between Ge (left) and InGaAs (right). From [4]

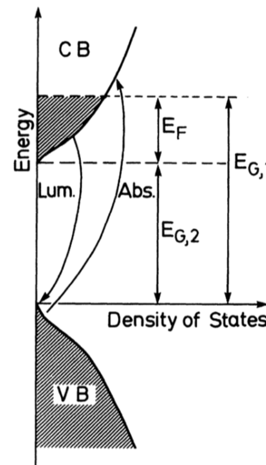

Figure 2.18: Photoluminescence in density Of States vs energy representation of the band structure. From [27]

Once the electrons have relaxed to the bottom of the conduction band, they recombine through the slow, phonon mediated, indirect recombination process.
The emitted photon doesn't have the exact band gap energy. Two major factors are responsible for the difference between the emitted photon energy and the band gap:

- The electron's excited state is not always the bottom of the conduction band. This phenomenon is illustrated in figure Figure 2.18, where the Fermi energy is raised above the conduction band through $n-$type doping in Si. Excited electrons with energy between the Fermi energy and the bottom of the conduction band can recombine with hole. The *optical* band gap, $E_{G,2}$ is given by $E_{G,1} = E_{G,2} + E_F$, with $E_G, 2$ the standard band gap and E_F the fermi level.[27]

- The absorption or emission of phonons for the indirect transition has to be taken account in the recombination's conservation of energy. $E_{photon} = E_g + x\hbar\omega_0$, with ω_0 the phonon energy and x a positive/negative integer representing the number of absorbed/emitted phonons. The order of magnitude of a phonon energy is about 0.02 to 0.06 eV for TA, LA, TO and LO phonons[15], which is about 1-2 orders of magnitude lower than the photon energies. [25]

To sum up, photoluminescence in silicon or germanium gives an indication about the band gap, however the photons are weakly emitted and their energy is not a direct representation of the band gap.

[15]Transverse Acoustic, Longitudianl Acoustic, Transverse Optic and Longitudinal Acoustic. Acoustic phonons are coherent movement of the ions inside a crystal structure, Optical phonons are out-of-phase ion movements in the crystal lattice.

LASER effect

As said earlier, an integrated laser would be the ideal light source for optical interconnections. Laser devices emit light through the Light Amplification by Stimulated Emission of Radiation (LASER) mechanism.
Every material cannot exhibit the LASER effect. First, the material has to have a direct band gap, since indirect band gap material have weak light emission intensity.

Lasing requires more electrons in the direct conduction valley than in the ground state (valence band). This state is called **population inversion** and is the first requirement for the LASER effect. The mass excitation of electrons can be caused by absorption of an incident light (*optical pumping*) or by running a electrical current through an heterojunction (*electrical pumping*).
Moreover, to achieve population inversion, the density of states in the direct conduction band must also be substantial. If a direct band gap material exhibits an indirect conduction bands with an effective DOS order of magnitudes larger than the effective DOS of the direct band gap, a larger share of excited electrons will end up in the indirect band gap anyway, disrupting the population inversion".

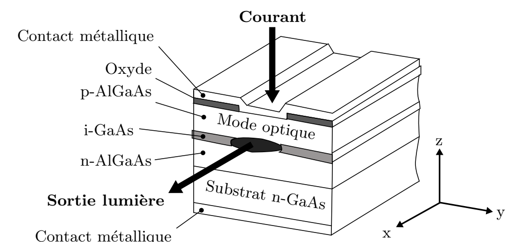

Figure 2.19: GaAs diode laser. The *p*AlGaAs-GaAs-*n*AlGaAs structure forms the heterojunction. From [26]

The next step is the **stimulated emission of photons**. Through its interaction with surrounding atoms, an incident photon will cause the electrons in the excited state to relax, emitting another photon. The emitted photon will have the same wavelength, phase and polarisation as the incident photon. As more electrons are being continuously pumped in the conduction bands, each emitting photon will trigger the relaxation of other excited electron, causing a cascade of stimulated emission. The material exhibit a **net optical gain** when more photon are being emitted than absorbed. Thus, the population inversion is a sine quae non condition for net optical gain. Other effects, such as interaction with defects, can be obstacles to reach net optical gain.

Semiconductor lasers are often made out of GaAs, a common semiconductor in optoelectronics. GaAs has a direct band gap, and GaAs laser are of made using an **heterojunction**: the active GaAs layer is sandwiched between two wide band gaps AlGaAs layers. The heterojunction confines carriers in the GaAs layer, which is vital for laser operation. When current runs through the heterojunction, population inversion occurs and the light produced is confined in the GaAs layer. Figure Figure 2.19 is a typical example of GaAs diode laser. Such devices can be made at scale small enough to be constructed on integrated circuits (they become Quantum Well lasers though). GaAs lasers on Si wafers are called "hybrid" integrated optoelectronic devices.

The description of photoluminescence and the LASER effect highlight important optical material properties. The qualitative concepts of *optical band gap, phonon interaction in indirect band gap transition, population inversion, heterojunction, net optical gain* are important to understand the band engineering of Ge or Si light emitting devices.

2.3 Strain engineering in Si and Ge

As highlighted in the previous section, due to their indirect band gap, silicon and germanium are poor light emitting materials. Nevertheless, both Si and Ge can theoretically be transformed into direct band gap material through the application of mechanical **strain**.

Strain applied to semiconductors will deform their crystalline structure. A general strain tensor can be decomposed into an **hydrostatic** and two **shear** strain tensors:

$$\begin{bmatrix} \varepsilon_{xx} & \varepsilon_{xy} & \varepsilon_{xz} \\ \varepsilon_{yy} & \varepsilon_{yy} & \varepsilon_{yz} \\ \varepsilon_{zz} & \varepsilon_{zy} & \varepsilon_{zz} \end{bmatrix} = \frac{1}{3}\begin{bmatrix} \varepsilon_{xx}+\varepsilon_{yy}+\varepsilon_{zz} & 0 & 0 \\ 0 & \varepsilon_{xx}+\varepsilon_{yy}+\varepsilon_{zz} & 0 \\ 0 & 0 & \varepsilon_{xx}+\varepsilon_{yy}+\varepsilon_{zz} \end{bmatrix} + \frac{1}{3}\begin{bmatrix} 2\varepsilon_{xx}-(\varepsilon_{yy}+\varepsilon_{zz}) & 0 & 0 \\ 0 & 2\varepsilon_{yy}-(\varepsilon_{xx}+\varepsilon_{zz}) & 0 \\ 0 & 0 & 2\varepsilon_{zz}+(\varepsilon_{yy}+\varepsilon_{xx}) \end{bmatrix} + \begin{bmatrix} 0 & \varepsilon_{xy} & \varepsilon_{xz} \\ \varepsilon_{yy} & 0 & \varepsilon_{yz} \\ \varepsilon_{zz} & \varepsilon_{zy} & 0 \end{bmatrix} \tag{2.5}$$

If the strain is applied to a cubic crystal unit cell, the first tensor accounts for the volume change of the cell (hydrostatic strain) and the two latter tensors describe the shape deformation of the reference cubic cell (shear strain). The [1 1 0] uniaxial strain, an important strain for the experimental part of the master thesis, has both hydrostatic and shear components.

Both shear and hydrostatic strain can deform a semiconductor's band structure. In simple words, a tensile/compressive strain will **reduce/widen** the semiconductor's bandgap, whereas a shear strain will cause the **degeneracy lifting** of the valence and conduction bands.

2.3.1 Strain effects on symmetry

Some effects of mechanical strain on a semiconductor can be understood trough the deformation of its crystalline structure.
Though hydrostatic strain has no impact on the crystal symmetry, the application of shear strain on a crystal reduces its symmetry. For instance, applying a [110] uniaxial stress on a cubic crystal[16] transforms it to a orthorhombic crystal. As the band structure has the same symmetry as the crystal lattice, the transformation to a crystal system with less symmetry will transform the band structure. Furthermore, as explained in the previous section, Si, Ge (and GaAs) have the same lattice symmetry (cubic). Thus, their band structure, despite being different, have the same symmetry. Therefore, they show some similarities when they are exposed to strain.

Degeneracy lifting in the valence band

The effect on strain on the valence bands is studied at the Γ point, which is the valence band peak for Si, Ge and GaAs.
These semiconductors show a cubic symmetry (*cubic semiconductors*), they have two doubly degenerate valence bands, excluding spin-orbit interactions. Those two valence bands are called the Light-Hole (LH) and Heavy-hole (HH). Shear strain induces degeneracy lifting in those LH and HH bands, as

[16] Cubic crystal = Crystal belonging to the cubic crystal system = **lattice** with cubic symmetry

depicted on figure Figure 2.20.

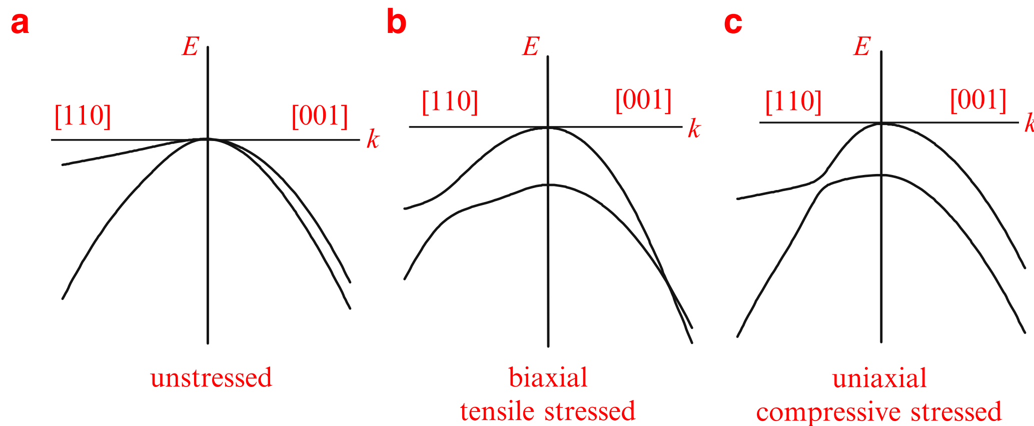

Figure 2.20: Representation of strain-induced degeneracy lifting at the Γ point in the valence band of Si. **a,b** and **c** refers to, respectively, the unstressed, biaxially tensile stressed and unixially compressive stressed cases. From [18]

Degeneracy lifting in the conduction band

Unlike the valence bands and the Γ point, conduction band minima can be found at different locations in the Brillouin zone. As shown on figure Figure A.1, silicon has its **indirect** conduction band minimum[17] in a Δ valley, at about $0.85X$. At this minimum, silicon conduction bands have a sixfold degeneracy. In contrast, Ge has its **indirect** conduction band minimum at the L point, where the bands have a fourfold degeneracy.

These degeneracies result from the *star*-type degeneracy, where the k-points in the Brillouin zone that can be transformed into each others and become equivalent trough the band structure symmetry must have the same energy. This star-degeneracy causes the sixfold degeneracy in the Δ-valleys in Si and the fourfold degeneracy in the L-valley in Ge.
Ge and Si have their conduction band minima at different locations in the Brillouin zone, which differentiate their strain-induced band splitting. For instance, under biaxial strain in the x and y direction, Si Δ-valleys are split into to the Δ_2 and Δ_4-valleys. However, the L-valleys in Ge are homogeneously affected by such strain and the conduction band does not split.
On the other hand, the **direct** Γ-conduction band in both Ge and Si is singly degenerate and thus, does not split under shear strain.

Sum up of strain effect on crystal symmetry

The qualitative description of the strain effects is summed up in the figure Figure 2.21. It shows the effect of hydrostatic strain, which widens or reduces the band gap and the shear strain, which lifts the degeneracy of valence and conduction bands.
The description of strain-induced band gap modifications are qualitative. They only describe the band splitting caused by shear strain and the direction of band gap widening/reducing cased by hydrostatic strain. Because symmetry doesn't take into account the real electrical potential distribution, it can't describe crucial features such as the band energies, curvatures,..
However, quantitative modelling of such phenomena are necessary for the the work done in this master thesis. Therefore, the next section will introduce more complete models used to describe the strain engineering of semiconductor's electronic band structure.

[17] A band minimum is also called a "valley".

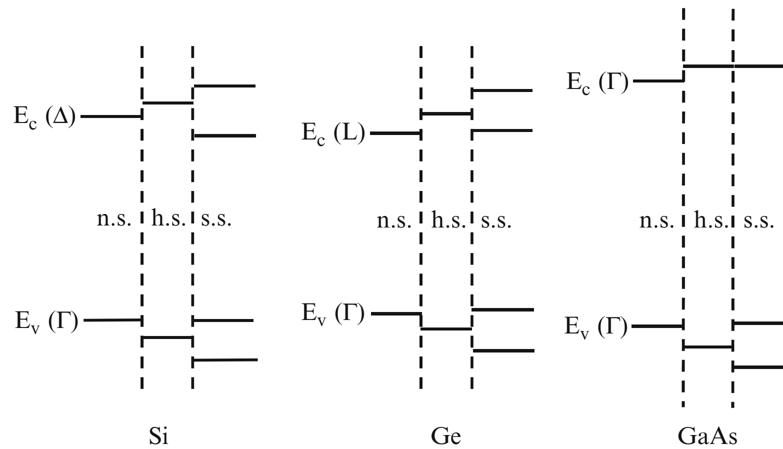

Figure 2.21: Qualitative effect of strain on band gap, for Si, Ge and GaAs in different stress/strain configurations. From [18]

2.3.2 Strain engineering of the band gap: the Deformation Potential model

The study of opto-electronic properties of semi conductor cannot be based on the qualitative description given in the previous section. Symmetry considerations certainly bring essential information about the semiconductor behavior, but it lacks any quantitative description of the strain effect on band structure. Therefore, this section's purpose is to introduce a model that can be used to precisely (to a certain extent) study the effects of strain on opto-electronic properties of Si and Ge.

Precise strained band structures can be obtained through the use of complex dedicated methods. To name a few, one could use a strain-modified k · p method, or the Pikus-Bir strain hamiltonian, in the framework of the k · p method, or even ab-initio pseudopotential calculations that takes strain into account. [4, 18]

However, full band structure simulation is not required for the study of opto-electronic properties. In the framework of this master thesis, the only relevant feature is the band gap modification induced by mechanical strain.

Therefore, here, the best way to predict the effect of strain on Si and Ge's band gap is to use the **Deformation Potential** theory. Using deformation potentials, band energy shift and strain are related by:

$$\varDelta E = \sum_{ij} \varXi_{ij} \varepsilon_{ij} \tag{2.6}$$

Where $\varXi_{ij}$ are deformation potentials and ε_{ij} the strain tensor components.

By applying this band shift calculation to the band edges[18], one can compute the altered band gap. With this model, it is possible to compute separately the direct and indirect band gap dependence to strain. This allows, for a given strain configuration, to get an estimation of the required strain to have a transition from indirect band gap to direct band gap behavior in Si and Ge. One example of such calculation is given in figure 2.25.

Deformation potentials

The deformation potentials, $\varXi_{i,j}$, are given for specific conditions. They have given values for specific strain configurations and locations in the first Brillouin zone. Deformation potentials can be extracted from simulated or experimental plot of of band gap versus strain. The linear nature of the band gap dependence to strain limits this theory to small values of strain. When the strain in the semi-conductor is more than a few %, correction have to be made, or other model have to be used. [28]

[18]Band edges = valleys in the conduction band or peaks in valence band

An example of deformation potentials values (eV), along with the unstressed band gaps of Si and Ge is given in Table 2.5.

	Ξ_d	Ξ_u	a
Si	-6.0	7.8	-2.46
Ge	-9.1	15.9	-1.24

Table 2.5: Deformation potential of Si and Ge. Ξ_d and Ξ_u are given for the lowest indirect conduction band. [18]

Band splitting in deformation potential calculations

However, to evaluate the band gap of a strained band structure, it is crucial to apply the band shift calculation of 2.6 on the correct band edge. Indeed, when strain is applied, electronic bands are shifted *and* split.
In the case of silicon, as explained in subsection 2.3.1, a [110] uniaxial strain splits the Δ-valleys of the conduction band. The [110] uniaxial strain is chosen as example because it the type of strain obtained in the experimental part of this work.
Therefore, to compute the altered band gap, one must apply the energy shift of Equation 2.6 to the the lowest split conduction band, and the valence band. This process is graphically shown on figures 2.22 and 2.23. The same applies reflection applies to the splitting of the valence band at the Γ point.
Strain engineering of germanium follows the same logic, the only difference being the location of Ge's conduction valleys at the L conduction band edge.

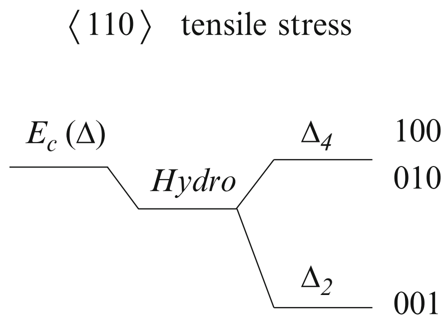

Figure 2.22: Schematic representation ofΔ valley splitting in Si under [110] uniaxial tensile stress. The Δ valleys split into the Δ_2 and Δ_4-valleys, from [18]

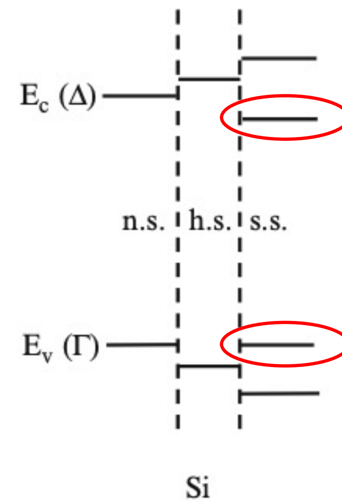

Figure 2.23: Band edges to be considered in the deformation potential calculation of band gap. Modified figure from [18].

Energy shift of the conduction bands

The shift in energy of the conduction band is required to compute either the direct or indirect band gap under strain. For **silicon**, two strain-induced shifts are interesting here, the shifts in the direct Γ-conduction and indirect Δ-valleys. The application of a [110] uniaxial tensile strain is considered in the developments below.
The direct Γ-conduction conduction valley is only singly degenerated, it doesn't split under strain.

Therefore, only the hydrostatic contribution of the strain has to be taken into account. Its enegy shift is given by:

$$\Delta E_{c,\Gamma} = \left(\Xi_d + \frac{1}{3}\Xi_u\right)(\varepsilon_{xx} + \varepsilon_{yy} + \varepsilon_{zz}) \tag{2.7}$$

Where Ξ_d and Ξ_u are the hydrostatic and shear deformation potential respectively.
The **indirect Δ conduction valleys** are shifted and split by a [110] uniaxial strain. Therefore, the total energy shift of the Δ-valleys is the sum of the contributions of hydrostatic and shear strains. To compute the band gap, the shift of the Δ_2-band is considered (see Figure 2.22 and Figure 2.23):

$$\begin{aligned} \Delta E_{c,\Delta_2} &= \Delta E_{c,hydr.} + \Delta E^{110}_{c,split.} \\ &= \left(\Xi_d + \frac{1}{3}\Xi_u\right)^{\Delta}(\varepsilon_{xx} + \varepsilon_{yy} + \varepsilon_{zz}) - \frac{1}{3}\Xi^{\Delta}_u(\varepsilon_{zz} - \varepsilon_{xx}) \end{aligned} \tag{2.8}$$

Where Ξ^{Δ}_u is the shear deformation potential in the <110> direction, corresponding to the Δ_2-band.[29]

The same calculation holds for **germanium**, where the only difference being that the indirect conduction valley is located at the L point in the Brillouin zone.

Energy shift of the valence bands

The shift in energy of the valence band is the second element required to compute the strain-altered band gap of a semiconductor.
For Si and Ge, the peak of the valence band is always at the Γ point in the first Brillouin zone.
The hydrostatic contribution of the strain to the Γ valence peak is given by:

$$\Delta E^0_v = aI : \bar{\bar{\varepsilon}} \tag{2.9}$$

where a is a deformation potential, I the unit, second order tensor and $\bar{\bar{\varepsilon}}$ the strain tensor.
A description of the valence band split in LH and HH valence bands using deformation potentials has not been found.

Strained band gap calculation

Thanks to the deformation potentials, the energy shifts of the strained conduction and valence band can be computed. Therefore it is possible to calculate the strain-altered direct and indirect band gap. In sum, equations to compute the direct and indirect strained band gap in Si and Ge are given in Table 2.6. Examples from the scientific literature of deformation potential-based, strained, band gap calculation are given on Figure 2.25 and Figure 2.24. In Figure 2.24, the authors have developed a modification of the band energy shift calculation from deformation potential. This modification includes a second order term to be added to the direct and indirect band gap calculation. This results in a more precise model for large strains. [28]

	Silicon	**Germanium**
Direct band gap	$E_{bandgap,d} = (E_{c.,\Gamma} + \Delta E_{c.,\Gamma}) - (E_{v.} + \Delta E_v)$	$E_{bandgap,d} = (E_{c.,\Gamma} + \Delta E_{c.,\Gamma}) - (E_{v.} + \Delta E_{v.})$
Indirect band gap	$E_{bandgap,i} = (E_{c,\Delta} + \Delta E_{c,\Delta_2}) - (E_v + \Delta E_v)$	$E_{bandgap,i} = (E_{c,L} + \Delta E_{c,L}) - (E_v + \Delta E_v)$

Table 2.6: Strain-alterd band gap calculation. The $\Delta E_{x,y}$ refers to the strain-induced energy shift of the x band at the y location of the Brillouin zone. These shift are calculated from the deformation potentials.

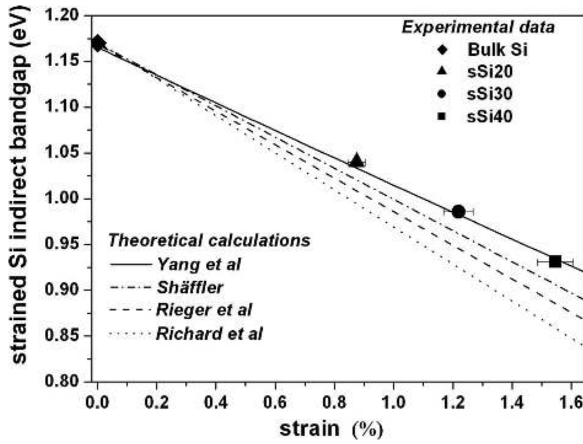

Figure 2.24: Theoretical calculation and experimental measures of the strained Si indirect band gap for a biaxially tensile strained sample. Theoretical calculation where made using deformation potentials. From [30].

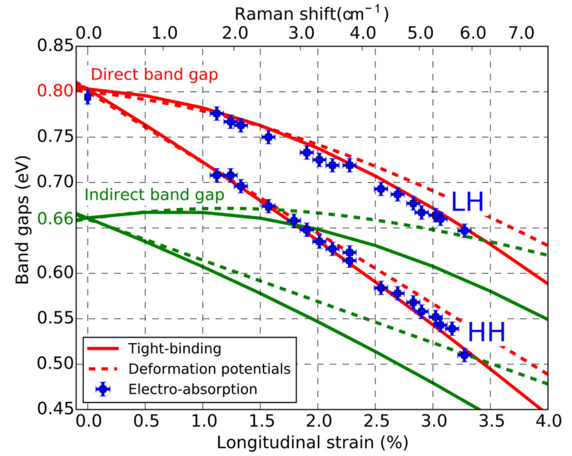

Figure 2.25: Comparison between theoretical calculation and experimental data of the strained direct and indirect band gap in Ge, for a [110] uniaxial tensile strain. Theoretical data are obtained from tight-binding and a modified deformation potential methods. From [28].

2.3.3 Indirect to direct band gap transition in Si and Ge

Strain-induced transition from an indirect band gap to a direct band gap behaviour in silicon and germanium happens because the direct band gap (Γ conduction valley) becomes smaller than the direct band gap. This phenomenon occurs because, under certain loading condition, the direct Γ conduction valley decreases in energy faster than the indirect Δ valley in the case of Si, or the L-valley for Ge. The phenomenom is illustrated on Figure 2.26 and Figure 2.28

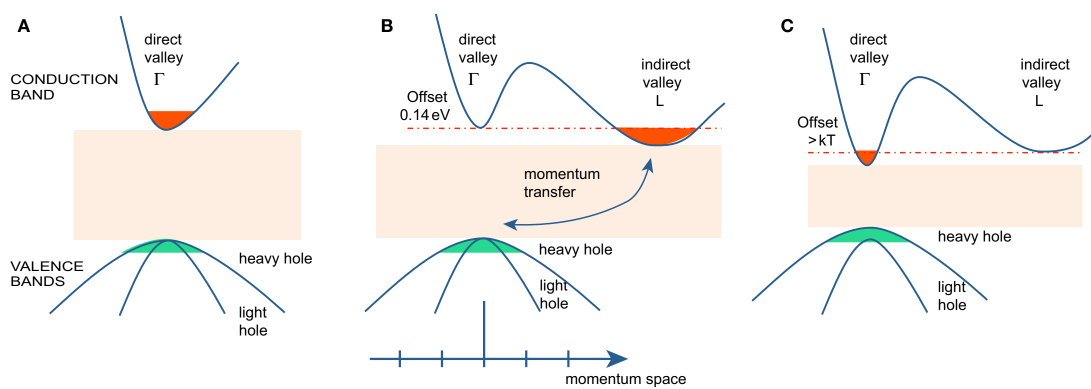

Figure 2.26: Diagrams of band structures in momentum space. **(A)**: Reference, band structure of a direct band gap material such as GaAs. **(B)**: Unstrained Ge, excited electrons occupy the conduction band at the L-valleys, radiative recombinations of electrons are hindered by the momentum mismatch in the k-space. **(C)**: Band structure of Ge that has been strained to a sufficiently high value or has been alloyed with Sn. The balance of electron population between the Γ and L points are inverted and Ge behaves as a direct band gap material. From [1]

In the scientific literature, simulations have been carried out to determine, for specific loading conditions, how much strain is required for this transition to happen.

Indirect to direct band gap transition in Si

For silicon, most recent research points to the following results. Using first principle calculations, based on an ab-initio (Vienna ab initio simulation package) band structure calculation method, *Li et Al.*

(2019) [31] demonstrated that for [110] uniaxial strain, a loading of only 4% is sufficient to achieve the transition. Moreover, the author showed that a [111] uniaxial strain require 14% strain.
Another work performed by *Shi et Al. (2019) [32]* indicates a direct band gap transition for silicon under the loading: $\varepsilon_1 = \varepsilon_2 = \varepsilon_3 \geq 9.3\%$

Indirect to direct transition in Ge

According to the deformation potential theory, the indirect to direct band gap transition in germanium is theoretically expected at $4.3 - 4.6\%$ uniaxial strain in the [100] direction, as well as at 1.7% for in-plane biaxial strain on a [100] Ge wafer. [29, 33, 3]

Tight-binding simulations place the transition point towards 5.7% uniaxial tensile strain and 1.9% biaxial strain. Experimental proof has the tendency to prove the deformation potential results right over the tight-binding ones. However, it has recently been proven that the, linear, strain-Raman shift relation, used to measure the strain in Ge samples, suffers from non-linearity when the strain grows larger (from 2% strain in [100] unixaial tensile strain). Thus, the $4.3 - 4.6\%$ uniaxial tensile strain value should be taken with a grain of salt. [34]

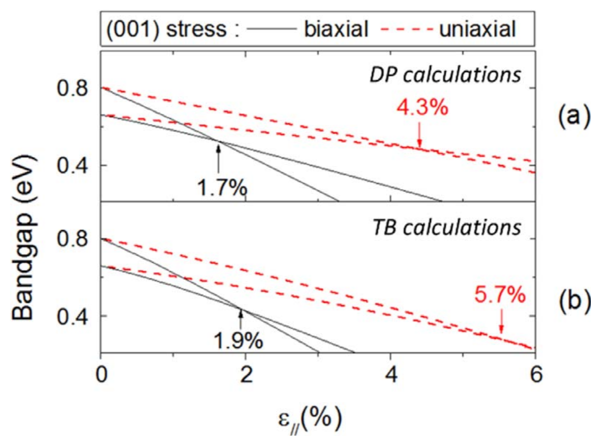

Figure 2.27: Direct and indirect band gaps of Ge as a function of [100] uniaxial tensile strain (a), using deformation potentials and tight binding models (b). From [3]

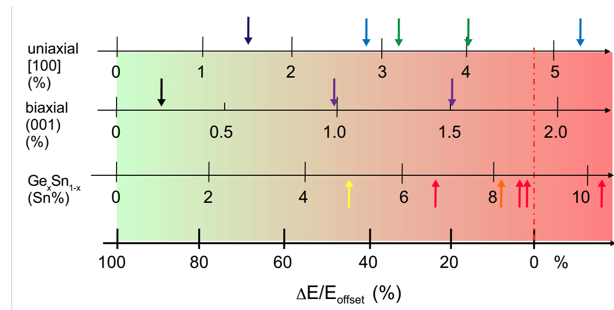

Figure 2.28: Relative offset of the Γ- and L-conduction bands in Ge that is either strained or alloyed with Sn. An offset below 0% means that the band gap is direct. Coloured arrows represent the offset experimentally achieved in the literature. From [1]

2.3.4 From direct band gap transition to population inversion

The indirect to direct band gap transition in Ge (and Si) is a necessary step to achieve the condition of population inversion of the LASER effect, but not sufficient. Another crucial contribution to take into account is the relative population of the direct band gap valley and the indirect valleys. Due to the characteristics of the indirect L valleys in Ge, the density of states is much higher in the indirect valleys than in the direct valley, resulting in a favourable population of the indirect valleys even at the indirect to direct band gap transition. For Ge, the indirect to direct transition is estimated to be achieved at around 4.6% uniaxial strain. At room temperature, 4.6% strain translates roughly to less 2% of excited electrons residing in the direct valley, which is not enough to satisfy the condition of population inversion. The electron distribution between direct and indirect valleys varies with temperature and is more favourable when T decreases, as illustrated in figure 2.29. [35]
A 50% of electron distribution in the direct valley is a good reference to enable the population inversion, a condition only met for strain superior to 8.0% at room temperature. [35]
Whilst this 8.0% uniaxial strain condition is not cast in stone, it highlights the need for an excess of strain to reach the first condition of the LASER effect, population inversion.

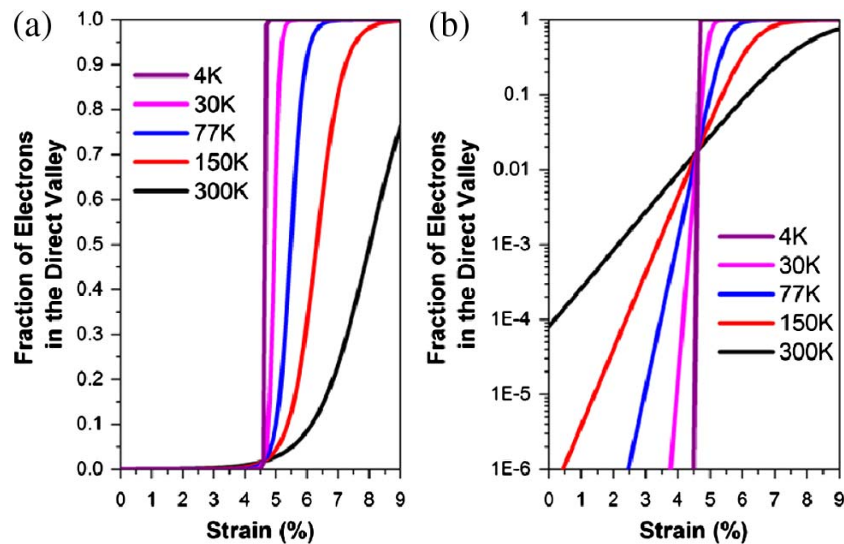

Figure 2.29: Fraction of electrons present in direct valley rather than in indirect valley vs. temperature, theoretically calculated from the deformation potentials of Ge. a) Linear scale, b) log scale, from [35].

2.4 Review of strained Si and Ge opto-electronic devices

This section explores the current landscape of strained Si and Ge opto-electronic devices, as well as some important results coming from simulations. Such simulation results are, for instance, the strain required for a indirect to direct band gap transition. The strained devices explored in this section range from "simple" strain-inducing devices, to laser devices.

2.4.1 Strained Si devices

As highlighted just above, improving optical performances of silicon and germanium requires strains as large as a few percent to more than 10%.
Some devices have been designed with sole purpose to induce large strains in silicon micro-structures. The **lab-on-chip** devices, developped at the UCLouvain, have been used to load silicon beams to up to 3.6% in uniaxial tensile strain. These devices use micro-structures to induce strain in hundreds of suspended Si beams at the same time. A lab-on-chip microstructure is shown on Figure 2.30 and are extensively described in section 3.2 and chapter 4

Ultra-large, 16% uniaxial tensile strain has been reported by *Zhang et Al. (2016) [36]* in nano-scale silicon sample. This research used vapor-liquid-solid–grown single-crystalline Si nanowires with diameters of 100 nm to achieve this ultra large, fully reversible (elastic), strain. The nanowire was grown along the <110> direction and stress was applied in the same direction.
The size and defect-free characteristic of nanowire grown with this method allows it to be strained to such values. The experimental set up is presented in Figure 2.31.

2.4.2 Strained Ge devices

Strain in germanium has received substantially more attention than Si in recent years, leading to numerous devices developments.

GeOI wafers

The introduction of Germanium-On-Insulator (GeOI) wafers had a key impact on the strained Ge research. These wafer have a special top Ge thin film that is defect-free that can withstand much more strain than any other type of thin-film Ge. GeOI wafers are the Ge-variant of the more mature Silicon-On-Insulator (SOI) wafers technology. They have a similar structure: the wafer is made up from

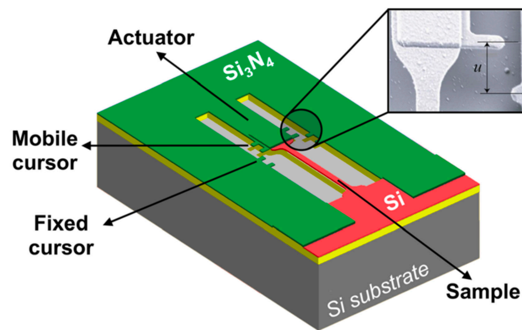

Figure 2.30: Actuator and sample of a lab-on-chip device. A mobile cursors moves with the actuator, while a fixed cursor on the sidewall acts as a reference for the direct measurement of displacement. From [37]

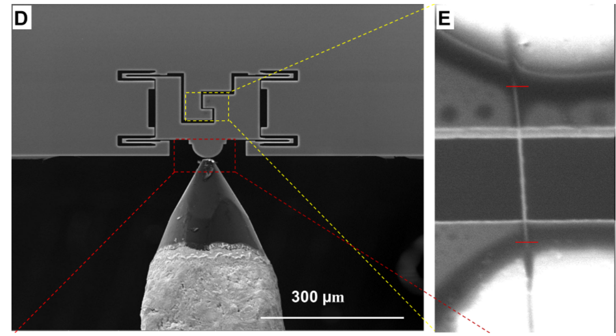

Figure 2.31: VLS grown silicon nanowire, strained using a push-to-pull mechanism. From [36]

3 layers of materials, a thick Si substrate topped with a high quality oxyde layer, called the Buried Oxyde layer (BOX) and a thin Si or Ge film on the top. The SOI and GeOI wafers are designed so that the top layer is the purest and has the least amount of defects, such as dislocations. An illustration of the quality of the top Ge film that can be achieved with a GeOI wafer has been illustrated by *Reboud et Al. (2017)* on figure 2.32. On this figure, the interface between a) Si and Ge in a thick film of Ge grown on a top of a SOI wafer b) Ge and SiO_2 (BOX) in a GeOI wafer are shown. Visually, one can tell that there are more misfit dislocations at the Si-Ge interface than at the BOX-Ge interface. Dislocations are harmful for photoluminescence as they behave as recombination centers, and for mechanical resistance to high strain.

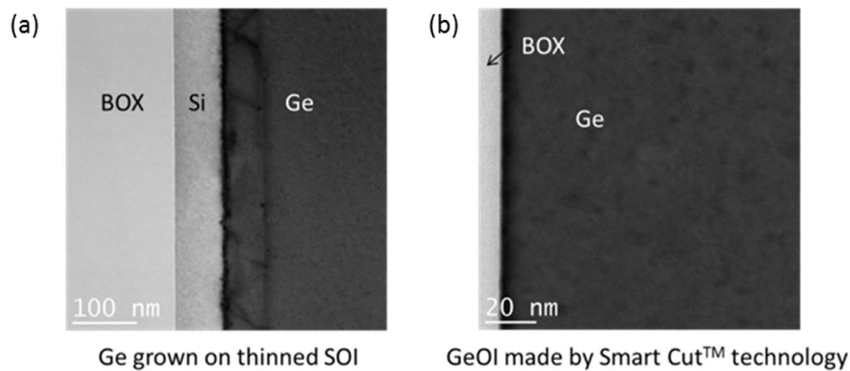

Figure 2.32: Cross-sectionnal TEM image of the interface between a) Si and Ge in a thick film of Ge grown on a top of a SOI wafer b) Ge and SiO_2 (BOX) in a GeOI wafer. The TEM image show a lot more misfit dislocations in the thick Ge film grown on the SOI. From [3]

GeOI and SOI wafers can be fabricated using a wafer-bonding method. The GeOI wafers studied by *Reboud et Al. (2017)* were fabricated using the SmartCut^{TM} process, developed by Soitec. This wafer-bonding based process is illustrated on figure 2.33. However, one big issue concerning the GeOI wafers is their availability. When working on this master thesis, no GeOI wafers were commercially available, which hindered the study reported in this work.

Devices not related to light emission

Most devices of interest are linked to light emission has Ge lasers are the missing piece of integrated light-emitting devices. Despite this, some device are worth some attention, especially the standalone modulator-passive waveguide-photodetector system developped by *Chaisakul et Al. (2014)* [16]. This

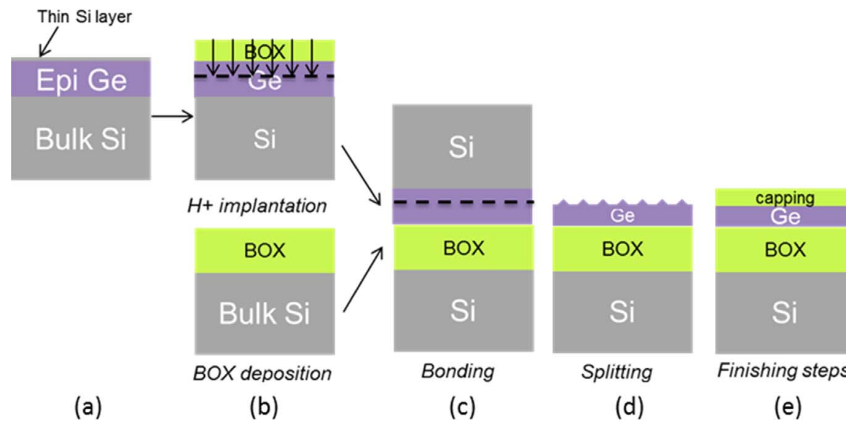

Figure 2.33: The SmartCut^{TM} process applied to GeOI wafer fabrication. From *Reboud et Al. (2017)*: "*Process flow to obtain optical GeOI substrates using the Smart Cut™ technology: (a) Ge growth on Si wafer, (b) Oxide deposition and H+ ion implantation, (c) Bonding onto a SiO2-Si handle, (d) Splitting of bonded wafers, (e) Surface cleaning by reactive ion etching and chemical mechanical polishing, then capping by 10 nm of deposited oxide.*"[3]

partial Ge optical interconnect, presented in figure 2.7, includes 3 of the 4 essential devices needed to build an integrated light-emitting device, with the exception of the light source. It is made from a Ge/SiGe Multiple Quantum Well (MQW) modulator, a SiGe passive waveguide and a Ge/SiGe MQW photodetector. The partial optical interconnect is a few hundred μm long for a few μm in width and was build on bulk Si wafer as a proof of concept. Its performance are not discussed here has they stretch beyond material engineering.

Ge nanomembranes strained by high pressure gaz.

Ge nanomemebranes strained by means of flexible polymer films and high pressure gas are a more archaic set up. In the work of *Botzug et Al. (2011)*, a 40nm thick Ge nanomembrane (NM) was biaxially stretched to around 2% of strain. The Ge nanomembranes comes from a (001) oriented GeOI top-Ge film, which was etched away from the BOX of the wafer to be deposited on a flexible polyimide (PI) film. The experimental set up is showed on figure 2.34. Whilst the authors claim to have reached a strain high enough for a direct to indirect transition, they based their results on Raman shift measurements. However, strain measurement in Ge through Raman shift measurements suffers from non-linear contributions that were highlighted a few years after this study. This issue is addressed in section 3.1.2. Moreover, the authors claim that population inversion is achievable for such strain, without an actual experimental proof. However as discussed in section 2.3.4, an excess of strain is needed to overcome limitations linked to the DOS difference between the direct and indirect valleys, which the authors seem to ignore. While this experimental configuration is not convenient for integrated circuit fabrication, this 2011 work paved the way to Ge micro bridges and micro crosses.

Microbridges

Various types of train inducing devices have been fabricated. To induce high uniaxial tensile strain, the suspended micro-bridge design can be used, see figure 2.35. This micro-bridge design uses strain redistribution from pre-existing internal stress. The strain is elastically redistributed between different regions of the liberated membrane, depending on their size, creating localised high-strain region similar to the necking process (while remaining in the elastic regime). These devices are fabricated using classical microfabrication techniques, such as E-beam lithography, etching on GeOI wafers. Strain valueup to 5.7% have been reported using this design on GeOI wafer in the study made by *Sukhedo et Al. (2014)*. [35].
This is currently the most popular design of Ge straining at the micro/nanoscale, due to their easy fabrication process and the high uniaxial strain achievable. A similar process is used to induce biaxial tensile strain, where micro-crosses are used. Record 2.3% biaxial strain was measured on a cross setup

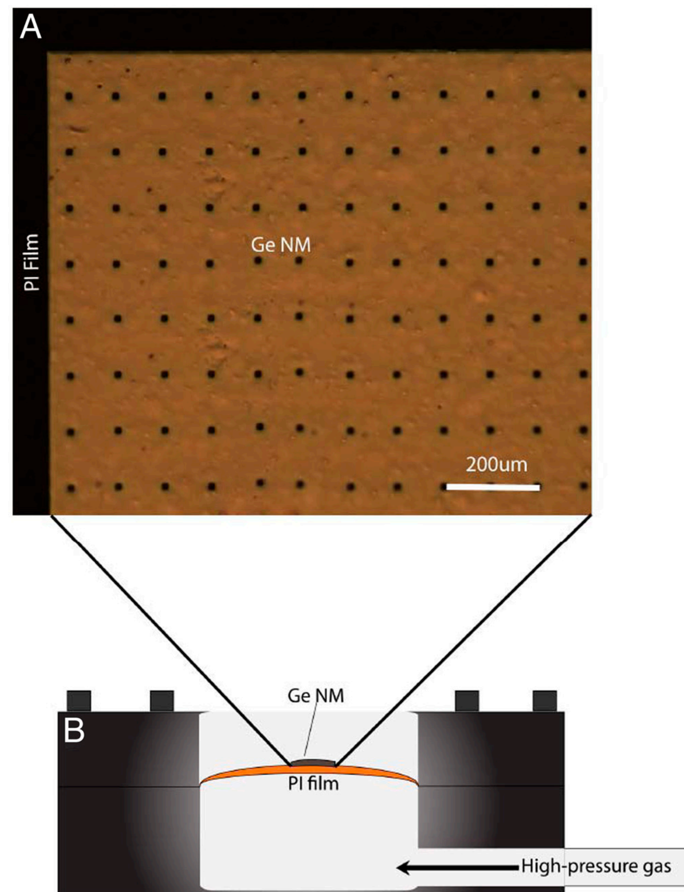

Figure 2.34: Top (A): Ge NM resting on a PI film, with holes used to introduce the etchant that allowed the top-Ge film to be removed from a GeOI wafer. Bottom (B): experimental set-up, with sample mount and high pressure gas chamber. From [38]

similar as the one showed on figure 2.36 by *Reboud et Al. (2016).* [39]

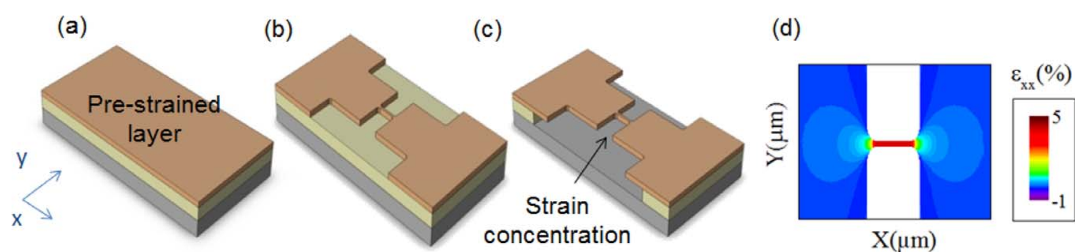

Figure 2.35: Fabrication steps of the suspended micro-bridge design, to induce uniaxial strain in Ge nanowires. From [3]

Heterostructures

Inducing strain inside a Ge sample is one thing, turning it into a functioning light emitting device is another. In this regard, systems such as heterostructures are a missing piece of the equation. Heterostructures are often required to create efficient opto-electronic device such as LEDs and lasers. Heterostructure sandwiches a narrow band gap region between two wide band gap regions, so that charge carriers are readily confined in the narrow band gap region. Carrier confinement is vital for efficient laser operation. The standard structures achieving this effect are the "double heterojunctions" structures, which requires multiple layers of materials showing substantial band gap offsets. However,

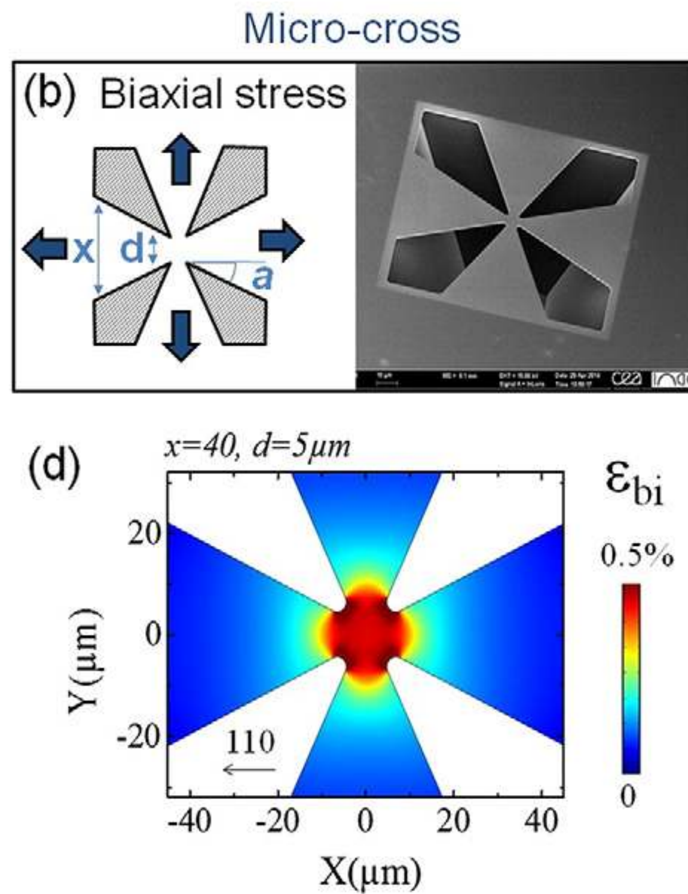

Figure 2.36: Micro cross design to induce biaxial strain in Ge. From [34]

their fabrication can be too complex or costly to be widely fabricated in integrated circuits. *Nam et Al. (2013)* have reported the fabrication of a Ge **pseudoheterostructure**, which performs the same task as a standard double heterostructure. Using strain distribution in a nanowire, the bandgap of Ge is modified to form a single-material heterostructure (the pseudoheterostructure). The band gap offset created by this technique is sufficient for the device to work at room temperature. A schematic representation of the strained Ge pseudoheterostructure is shown on Figure 2.37. [40]

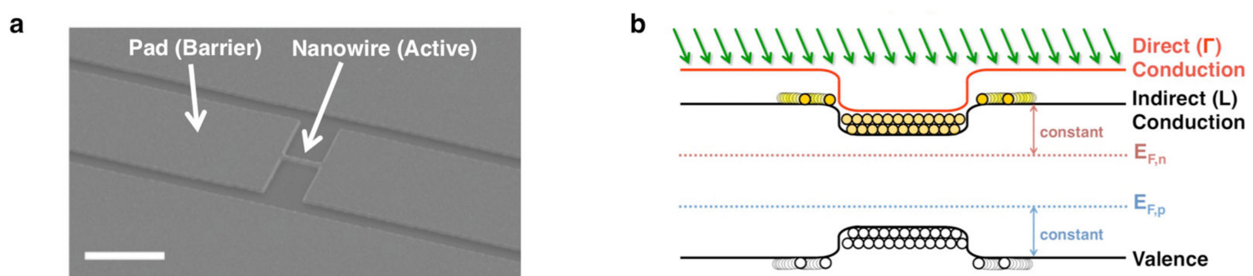

Figure 2.37: (a): SEM image of the suspended strained Ge pseudoheterostructure. (b): schematic representation of the band structure in the pseudoheterostructure. From [40]

The strained Ge pseudoheterostructure has been readily used to create a **device close a functionnal nano-scale laser**. *Petykiewicz et Al. (2016)* showed a device capable of enhanced direct-bandgap light emission, from a doped and strained Ge nanowire-based optical resonator. The device uses the pseudoheterostructure design described above with 2.3% uniaxially strained Ge, and distributed Bragg reflectors (DBR) as mirrors. The device is shown on figure 2.38.

Lasing is this device was not reported, however the direct band gap photoluminescence is improved 3 to 4 times over unstressed Ge (for similar doping), as can be observed on the spectra presented on Figure 2.39. [41]

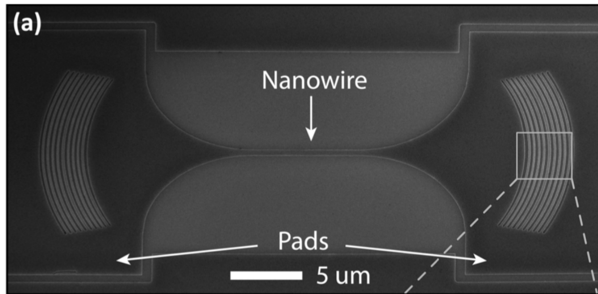

Figure 2.38: SEM image of the device: strained Ge pseudoheterostructure and DBR mirrors. From [41]

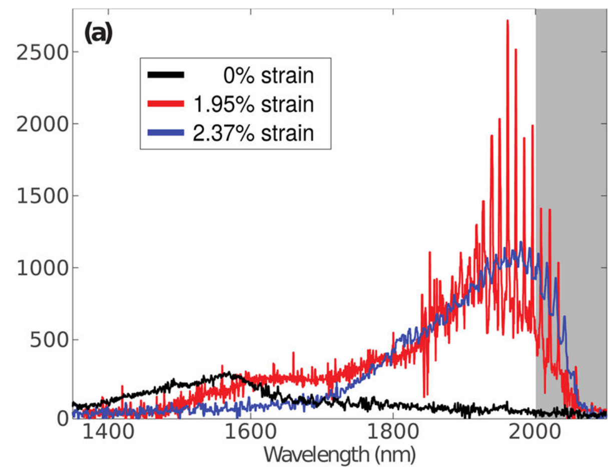

Figure 2.39: PL spectra for devices with 0%, 1.95% and 2.37% tensile strain. The direct-gap emission intensity increases greatly at higher strain [41].

LEDs

While not reaching the performances of lasers, LEDs based on strained Ge are under development and the research arond these devices help pave the way towards strained Ge lasers.
A germanium LED with a pseudoheterostructure similair to the one introduced previously has been studied by *Zhou et Al. (2017)*. Simulations on this design, using a k · p method and deformation potentials, have been carried out. For a 4% uniaxial tensile strain and $5.10^{18} cm^{-3}$ n-doping level, the simulations point to an internal quantum efficiency[19] of the diode around 9%.

Simulation of the quantum efficiency inside a strained Ge LED has also been performed by *Sukhedo et Al. (2014)*. In this study, the relation between internal quantum efficiency and uniaxial strain has been plotted, for various minority carrier lifetimes in a $10^{19} cm^{-3}$ n-type doped Ge. From this graph, showed on figure 2.40, *Sukhedo et Al. (2014)* observes that radiative recombination becomes dominant even for strain $< 2\%$ if there are fewer defects (higher τ_{defect}) in the Ge. This study therefore highlights the importance of GeOI wafers, where the reduced defect density enables higher deformations in Ge while also boosting the theoretical internal quantum efficiency of strained Ge LEDs.

[19] The internal quantum efficiency of a LED is the fraction of diode current that will produce luminescence.

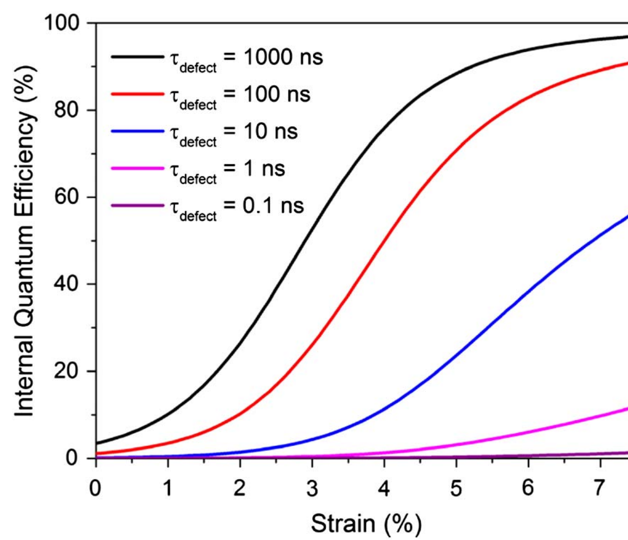

Figure 2.40: From [35]: "*Theoretical internal quantum efficiency of a Ge LED as a function of strain for various defect-limited minority carrier lifetimes at room temperature (300 K), assuming* $10^{19}cm^{-3}$ *n-type doping and 1017* cm^{-3} *carrier injection.*"

Chapter 3

Experimental methods

3.1 Raman spectroscopy

3.1.1 Basics of Raman spectroscopy

Raman spectroscopy studies the excitation of vibrationnal modes of a molecule or crystal lattice by a laser beam. Raman scattering requires the studied material to be polarisable. When a laser beam is shined on the surface of a sample, while most of the light is reflected or transmitted, some scattering of the incident light also occurs in the sample. When the scattered radiation is analysed, in addition to the initial light wavelength ν_0, a pair of new wavelengths appears $\nu' = \nu_0 \pm \nu_M$. This is the results of two types of scattering happening in the sample, Rayleigh and Raman scattering. In solid materials, for instance semiconductors, Rayleigh scattering is straightforward, an incident photon excites the crystal lattices to a virtual energy level and a photon of the same energy as the incident photon is emitted when the lattice relaxes to the base level. In Raman spectroscopy, another phenomenon occurs: the crystal lattice excited by the incident photon first relaxes to a lower virtual energy states by emitting a phonon, then relaxes to the initial energy state and emits a photon of lower energy than the incident photon (Stokes Raman scattering). Alternatively, the crystal lattice is already in an excited vibrationnal state before being excited further by the incident light, thus when the lattice relaxes to its initial state, a photon of higher energy than the incident photon is emitted (Antistokes Raman scattering). Therefore, when Raman scattering occcurs, the scattered photon shows a different wavelength than the incident light and the difference between these wavelength corresponds to the energy of the emitted (Stokes) or complementary (Antistokes) phonon $\hbar\Omega$:

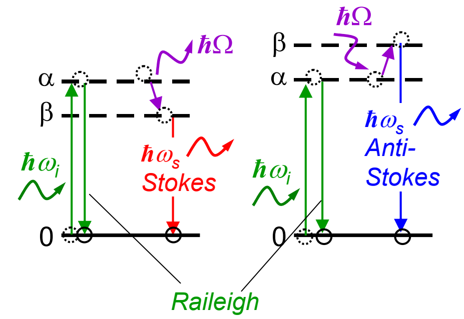

Figure 3.1: Basic principle of the Raman spectroscopy: Rayleigh vs. Raman (Stokes and antistrokes) scattering in crystals, from [42]

$$\hbar\Omega = \pm(\hbar\omega_i - \hbar\omega_s) \tag{3.1}$$

Phonons that can be activated by Raman scattering are called Raman-active phonons and have specific energies ($\hbar\Omega$ in equation (3.1)) correlated to the studied material's crystal lattice. The orientation of Raman-active phonons can be described from the Raman tensors, which are themselves determined from the crystal structure of the material. For silicon and germanium and their cubic structure described in the x=[100], y=[010], z=[001] coordinate system, the Raman tensors are:

$$\Delta_1 = \begin{bmatrix} 0 & 0 & 0 \\ 0 & 0 & d \\ 0 & d & 0 \end{bmatrix} \qquad \Delta_2 = \begin{bmatrix} 0 & 0 & d \\ 0 & 0 & 0 \\ d & 0 & 0 \end{bmatrix}$$

$$\Delta_3 = \begin{bmatrix} 0 & d & 0 \\ d & 0 & 0 \\ 0 & 0 & 0 \end{bmatrix} \qquad (3.2)$$

Where d is a non-zero parameter. Δ_j are used to define the total scattering intensity of the phonon modes, along with the polarisation vector of the incident e_i and scattered light e_s:

$$I = C \sum_j |e_i \cdot \Delta_j \cdot e_j|^2 \qquad (3.3)$$

Where C is a constant. Equation 3.3 illustrates the selection rule for Raman scattering, the material needs to be polarisable (ie: $\Delta_j \neq 0$) to have a non-zero Raman scattering intensity. Furthermore equation (3.3) can be used to describe which phonons (LO or TO) are active under different experimental configurations, as both the semiconductor's surface crystalline orientation (through Δ_j) and the polarisation of the light influences the intensity. Raman-active phonon are either longitudinal or transverse optical phonons (LO, TO), as acoustic phonons can't be excited by EM radiation. In unstrained silicon, the phonons are triply degenerated which means they all have the same energy, resulting in a single peak in a intensity vs wavenumber graph (typical graph obtained from a Raman spectroscopy instrument). For silicon this peak is around 520 $[cm^{-1}]$. [43, 44, 42]

3.1.2 Raman and strain

Raman spectrometers mesures the difference between incident and scattered electrons to deduce the energy of phonons associated to Raman scattering. These Raman-active phonons have specific energies correlated with the sample's crystal lattice. [43]

Strain has two major effects on the peaks observed by Raman spectroscopy:

- When the sample is strained (ie: strained Ge or Si thin films), the Raman active phonon's energies shift, just like a guitar strings's tone changes during the tune of the instrument. The energy change of the active phonon translates to a change of measured scattered light wavelength ω_s, thus a shift of the Raman peaks proportional to the amount of strain in the sample.
- Strain has another effect on the Raman scattering, it lifts the degeneracy between the LO and TO phonons in Si. This allows to differentiate LO and TO phonons in the intensity peaks of a Raman measurement.

The shift and splitting in intensity peak is proportional to strain and is described through the frequency of each active phonon modes j, $j = 3$ (2 TO, 1 LO):

$$\omega_j^2 = \omega_0^2 - \lambda_j \qquad (3.4)$$

Where ω_0 is the frequency of the triply degenerate phonons in unstrained Si, and λ_j are the eigenvalues of the following equation:

$$\begin{vmatrix} p\varepsilon_{11} + q(\varepsilon_{22} + \varepsilon_{33}) - \lambda_1 & 2r\varepsilon_{12} & 2r\varepsilon_{13} \\ 2r\varepsilon_{21} & p\varepsilon_{22} + q(\varepsilon_{11} + \varepsilon_{33}) - \lambda_2 & 2r\varepsilon_{23} \\ 2r\varepsilon_{31} & 2r\varepsilon_{32} & p\varepsilon_{33} + q(\varepsilon_{11} + \varepsilon_{22}) - \lambda_3 \end{vmatrix} = 0 \qquad (3.5)$$

The parameter p, q, r are material parameters called the Phonon Deformation Potentials (PDPs). The precise knowledge of these parameters depends on surface orientation and scattering geometry. [45] For simple configurations (ex: uniaxial tensile stress), this system can be simplified and solutions in the form of $\Delta\omega_j = f(\varepsilon_{k,l})$ can be found. Therefore, the strain in a sample can be precisely measured

through the Raman shifts $\Delta\omega_j$ and a few material parameters only.

However, a study made by *Gassenq et Al. (2016)* [34] revealed that this method of calculating strain from Raman shifts measurement is subject to errors when the strain grows larger than 1.2%, for uniaxial stress in Ge samples. This study highlighted a non-linear contribution, in the form of a second order Raman shift term:

$$\Delta\varepsilon_{100} = a\Delta\omega - b\Delta\omega^2 \tag{3.6}$$

Where $a \approx 0.68$ and $b \approx 0.019$ for Ge.

3.1.3 Raman spectroscopy applied to measure photoluminescence

Furthermore, a Raman spectroscopy instrument can also be used to perform photoluminescence experiments. Since the Raman spectrometer present in the Welcome facilities at UCLouvain uses a CCD sensor, a simple software trick can turn the relative measurements of the Raman peaks (equation (3.1)) into the absolute measurement of the scattered photons energies. If the laser produces photons with more energy than the sample material's optical band gap, scattered photon that have energy equal to the studied materials's bandgap can be observed. With such a set up it is then possible to measure the optical band gap of strained samples.

Sadly, due to the exceptional confinement measures linked to the Covid19 crisis in Belgium, no Raman mesurements or Raman-based photoluminescence measurments were performed in this work.

3.2 Lab-on-chip devices

Applying strain to silicon or germanium at the micro/nanoscale is at the core of this master thesis. This section describes the device used to strain silicon and germanium samples and its application to defect-free silicon specimens. On a side note, the word specimen is often replaced by "sample" in figures and graphs, they still refers to the same thing.

In order to apply strain on microscopic semiconductor specimens, one needs a dedicated straining device. Fortunately, an on-chip mechanical behaviour testing device has been under development at UCLouvain since 2007-2008. This device acts as a versatile MEMS-based mechanical testing platform and can apply strain to multiple microscopic specimens simultaneously. They are commonly referred to as "lab-on-chip devices" or "on-chip testing devices" throughout the rest of this document. The typical dimensions of their specimen are between 50-1000[μm] in length, a width around $\approx 1-5[\mu m]$ and a thickness $< 1[\mu m]$.

These devices, whose first purpose is to characterise microscopic specimens, can also be used to generate strain in multiple Si or Ge microscopic specimens. Moreover, by their design, the stress and strain inside the specimen can be easily extracted through the measurement of displacements.

The lab-on-chip devices rely on micro-fabrication techniques and offers a variety of mechanical tests, such as fracture tests or micro scale tensile tests. Lab-on-chip devices oriented towards micro uniaxial tensile tests are the device of interest here. They can theoretically deform multiple Si or Ge specimens to a few %, which would create a very interesting set of specimens to study the relation between strain and band gap shift in Si and Ge.

3.2.1 Design and concet

The core concept behind the on-chip testing technique is to use the internal stress inside an "actuator beam" to pull on a long, thin specimen. The internal stress in the actuator beam comes from the difference in thermal dilatation coefficient between the actuator material and the substrate on which it is deposited (Si_3N_4 for instance is deposited at $T \approx 800°C$). The specimen is deposited over the same substrate and is strongly anchored on one side and tied on the actuator on the other side. When the sacrificial layer is etched away, the actuator and specimen become free-standing and the actuator is free to unload its internal stress. Therefore, the actuator retracts, strongly pulling on the specimen in an unidirectional fashion. When the tensile force of the actuator and the retraction force of the specimen reach equilibrium, the strain and stress inside the specimen is extracted from the measurement of the specimen's displacement u. One elementary test yields one stress-strain point on the material's micro-scale stress-strain curve. This core design is presented on figure 3.2. [46]

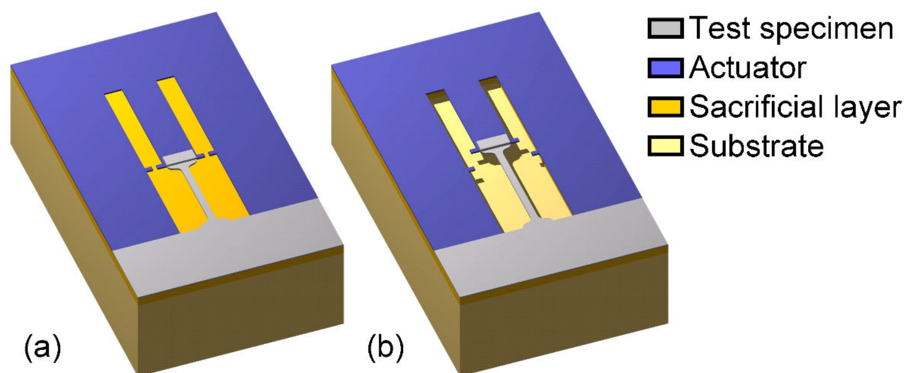

Figure 3.2: *"Elementary internal stress actuated uniaxial tensile test structure, (a) before release, (b) after release"* from [2]

One compelling advantage of the on-chip testing devices is the number of different elementary structures that can be created in a few microfabrication steps. As these kind of structures are often fabricated on top of a silicon wafer, well-established microfabrication techniques can be used to build hundred of elementary units on the same wafer, with varying geometries. Varying geometries implies various stress-strain states inside the specimen, with the ambition of covering the full micro-scale stress-strain curve of the specimen. Therefore, it could be possible to study the evolution of the band gap in silicon or germanium versus strain, from many specimens containing various amount of strains. Furthermore, the whole set of strained structure would fit on a single 3inch. wafer.

One drawback is that the specimen cannot be released *in situ*. The measurement of the displacement often takes places inside an electron microscope, which leaves time for some relaxation to occur inside the specimen. Another drawback is the presence of intrinsic errors in the measurement of the specimen displacement. This issue is addressed in chapter 4.

There is no standard fabrication process for lab-on-chip devices, as they vary with the material studied. Still, one common fabrication process is illustrated on figure 3.3. The starting silicon wafer is covered by a sacrificial layer, then the actuator material is deposited on top of the sacrificial layer and subsequently patterned into a beam using photolithography. The specimen is then deposited on top of the actuator and, in turn, is patterned by means of photolithography. Finally, the sacrificial layer is etched away and the actuator-specimen structure is released. As mentioned earlier, the actuator then unloads its internal stress, until force equilibrium.

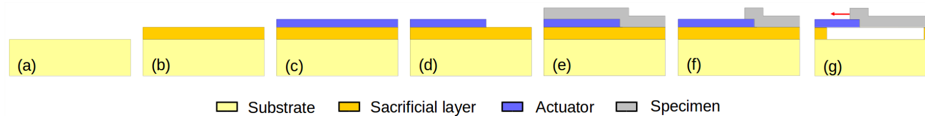

Figure 3.3: From [2]:"*Processing steps used to prepare tensile structures. (a) substrate, (b) deposition of the sacrificial layer, (c) deposition of the actuator, (d) patterning of the actuator, (e) deposition of the specimen layer, (f) patterning of the specimen and (g) release*"

The material of choice for the actuator beam should: **i)** a though material, to only deform elastically and avoid plastic, viscoplastic effects during the release and **ii)** generate a high level of internal tensile stress after its deposition on top of the sacrificial layer, ie: a thermal dilatation coefficient larger than the sacrificial layer material and high young's modulus. SiN is a material of choice for the actuator, as it is a good fit within those requirements. In the other hand, the specimen material can be freely chosen, as long as it is compatible with microfabrication processes.

3.2.2 Mechanical analysis of lab-on-chip devices

The stress σ_s and strain ε_s in the specimen can be extracted from the measurement of the specimen displacement u. This calculation requires the prior knowledge of the actuator's Young modulus E_a and the actuator and specimen's mismatch strain, respectively $\varepsilon_{mis,a}$ and $\varepsilon_{mis,s}$. Mismatch strain is the deformation caused by the accommodation of a film on its substrate during the deposition step. In the case of the lab-on-chip devices, the substrate is the sacrificial layer. On a side note, a more precise method, that accounts for errors made when calculating stresses and strains from the displacement u measurement is presented in chapter 4.
The displacement u is measured between a moving and a fixed cursor using electron microscopy, as highlighted on figure 3.4. By convention, u is positive for a displacement associated to the contraction of the actuator.

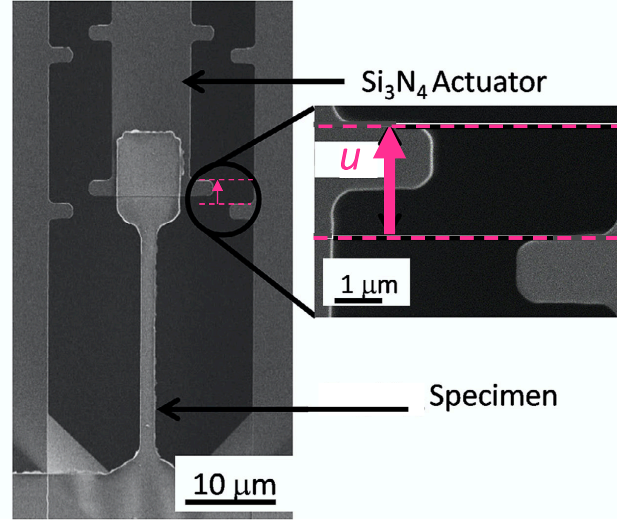

Figure 3.4: SEM image of a released structure, displacement u highlighted in magenta. Modified image from [47]

Stress-strain state at equilibrium in the actuator

When the structure reaches force equilibrium, the strain inside the actuator ε_a is the sum of the mismatch and mechanical strains:

$$\varepsilon_a = \varepsilon_{mech,a} + \varepsilon_{mis,a} \tag{3.7}$$

$$\varepsilon_a = ln\left(\frac{L_{a,0} - u}{L_{a,0}}\right) \tag{3.8}$$

Where $L_{a,0}$ is the initial length of the actuator, before release. Thanks to the elastic behaviour of the actuator, the stress is derived from Hooke's law:

$$\sigma_a = E_a \varepsilon_{mech,a} \tag{3.9}$$

In the end, the tensile force F can be derived from the previous equations:

$$F = A_a \sigma_a = A_a E_a \varepsilon_{mech,a} A_a E_a \left[ln\left(\frac{L_{a,0} - u}{L_{a,0}}\right) - \varepsilon_{mis,a} \right] \tag{3.10}$$

Which can be further simplified if one assumes that the small strains approximation is valid for the actuator:

$$F = A_a E_e \left(\frac{-u}{L_{a,0}} \varepsilon_{mis,a}\right) \tag{3.11}$$

Stress-strain state at equilibrium in the specimen

Again, strain inside the specimen is described by the sum of mechanical and mismatch strain:

$$\varepsilon_s = \varepsilon_{mech,s} + \varepsilon_{mis,s} \tag{3.12}$$

$$\varepsilon_s = ln\left(\frac{L_{g,0} - u}{L_{g,0}}\right) \tag{3.13}$$

Where $L_{g,0}$ is the initial length of the specimen, before release. From the force equilibrium $F_a = F_s = F$, one can write define the stress inside the specimen as:

$$\sigma_s = \frac{F}{A_s} = \frac{E_a A_a}{A_s} \left[ln\left(\frac{L_{a,0} - u}{L_{a,0}}\right) - \varepsilon_{mis,a} \right] \tag{3.14}$$

Or, if the small strains approximation is still considered valid:

$$\sigma_s = \frac{F}{A_s} = \frac{E_a A_a}{A_s}\left(\frac{-u}{L_{a,0}} - \varepsilon_{mis,a}\right) \tag{3.15}$$

As one elementary structure yields one $(\sigma_s, \varepsilon_S)$ point on the specimen's microscopic stress-strain curve, it is possible to obtain other $(\sigma_s, \varepsilon_S)$ points by using structures with different geometries, ie: different $L_{a,0}, A_a$ and $L_{g,0}, A_s$.

3.2.3 Fabrication steps for Si lab-on-chip devices

Disclaimers:

- The initial study should have been performed on germanium specimens. A GeOI wafer should have been processed to create strained Ge specimen using the lab-on-chip devices. However, no GeOI was available to purchase at the time of the experiment. Consequently, the study has been shifted to silicon. This section covers the experimental method required to obtain a set of strained, high-purity Si specimens using the lab-on-chip devices.

- Due to the combination of a temporary breakdown of an irreplaceable plasma etching equipment followed by the Covid-19 crisis and its subsequent confinement measurements, the experimental fabrication process was cut short at an early stage.

In order to study the evolution of the band gap in silicon with strain, defect-free silicon specimens are required. Indeed, the measurement of electronic transition around the band gap, performed with photoluminescence spectroscopy, is very sensible to defects. If a common lab-on-chip device were to be used, with a fabrication similar to the one described on figure 3.3, low quality Si sample would be created. Indeed, the silicon specimen would be deposited on top of a Si substrate, which would have resulted in low-quality, polycrystalline silicon specimen. The best way to circumvent this issue is to adapt the fabrication process of the lab-on-chip device presented onfigure 3.3, so that the specimen is not deposited, but rather patterned from the top film of a SOI wafer. As a matter of fact, the top film of a SOI wafer is a monocrystalline Si thin film with very low mechanical defect density, thus the best starting point to fabricate defect-free silicon specimens. SOI wafers were introduced alongside GeOI wafers in section 2.4.2. Nonetheless, adapting the lab-on-chip device fabrication to a SOI wafer alters the process shown on figure 3.3. Instead, the fabrication process mostly follows the steps developed by *Bhaskar et Al. (2012)*, depicted on figure 3.5. Some of the steps described by *Bhaskar et Al. (2012)* are missing in the diagram found in figure 3.3, found in the article.

Patterning the silicon specimen from the SOI top film

The first step is to carve the specimens out of the top film of a SOI wafer. This step already differs from the more "standard" lab-on-chip fabrication process depicted on figure 3.3 where the actuator is fabricated before the specimens. The process described here is not entirely represented on figure 3.5, but ends up at the top right corner step of the figure. The starting SOI wafers were prepared with a standard cleaning. A $20nm$ oxyde layer was grown on top of the top silicon of the SOI wafer at 900°C in a KOYO oven. After the oxidation, the thickness of the SiO_2 layer was measured by ellipsometry and the internal stress of the deposited layer was indirectly measured[1] by profilometry (Dektak machine). The measured oxide layer thickness was $12[nm]$, over a $136[nm]$ top Si film and a $1000[nm]$ BOX. Afterwards, a photolithography step was performed to carve the top SiO_2 into a mask. The photolithography mask "Gen6mod" was used, along with a positive photoresist. The SiO_2 was then etched away using a buffered HF (BHF) solution and the remaining photoresist was disposed of

[1] The internal stress was extracted through the Stoney formula, from curvature measurements made on Si test wafers. The Si test wafers were processed alongside the SOI wafers and were used as test dummies for some processes as well as for internal stress measurements.

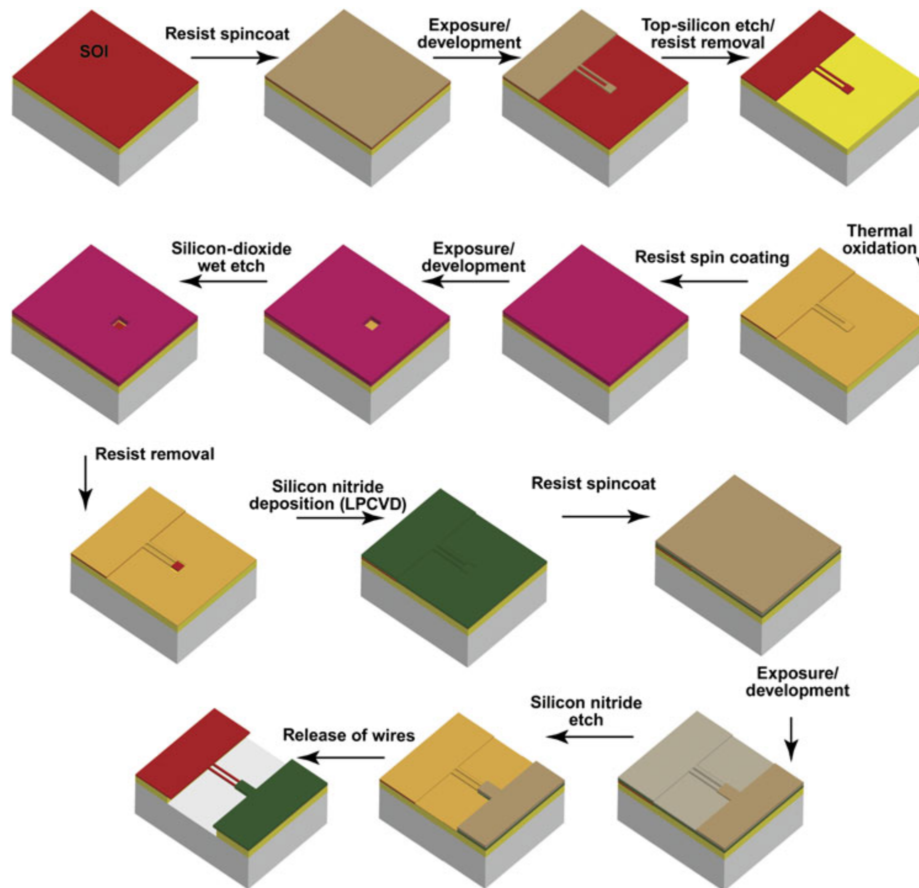

Figure 3.5: Fabrication process of a SOI top film micro scale tensile testing device, from [48]

using IPA and acetone. The result of these steps was the transfer of pattern from the "Gen6mod" onto the SiO_2, which then acted as a mask for the top-Si lithography.
A SiO_2 mask is required for the subsequent Si etching. A standard photolithography photoresist mask would not handle the plasma etching process. As a matter of fact, the top silicon was etched with Reactive Ion Etching (RIE), with a plasma made from a O_2 and Cl_2 gas mixture. Reactive ion etching is required because it creates highly anisotropic etch profiles. Highly anisotropic etch profiles result in clearly carved Si specimens. Otherwise, an isotropic etch would create an undercut profile in the Si specimens walls. The specimens would then have sloppy dimensions, from which precise stresses and strains would be harder to extract.

Troubles with the RIE process

The reactive ion etching proved to be a though challenge. An unknown failure during the etching process resulted in the partial etching of the silicon in 3 of the 4 wafer processed. One of the 3 failed wafer is shown on figure 3.6. Ellipsometry revealed that one part of the wafers was etched as expected, while the other part was not only partially etched, but also covered by an unknown layer of material. The unknown layer of material deposited on top of the partially etched Si seemed to be protect the Si beneath from the RIE process. Ellipsometry measurements were not able to identify the nature of the unknown layer, which is believed to be some Si-Cl-O based coumpound. This failure did not appear when a wafer was treated in a HF bath to remove any native oxide layer right before the etching process. It seemed that any amount of native oxide is linked to the failure by partial covering with the unknown layer.

Numerous hypothesis were raised to explain this behaviour. Any issue related to the nature of the etched Si was rejected, as the etched Si is the top-Si of a SOI wafer and therefore possess a highly

homogeneous crystalline structure, accross the entire wafer. Currently, the most probable hypothesis seems to be a plasma-related failure. Due to the nature of RIE, some Si and SiO_2 particles could have been torn off the wafer surface at the start of the RIE proces, reacting with the plasma and then deposit itself on the wafer. This would partly explain the origin of the unknown layer. However, the link between this supposed mechanism and the effect of the native oxide layer is not clear.

Finally, the unknown layer was successfully removed by dissolution in a BHF bath. The 3 wafers that underwent this RIE failure were successfully re-processed with the RIE process once the unknown layer was removed and any native oxide removed right before entering the palsma chamber of the RIE equipment.

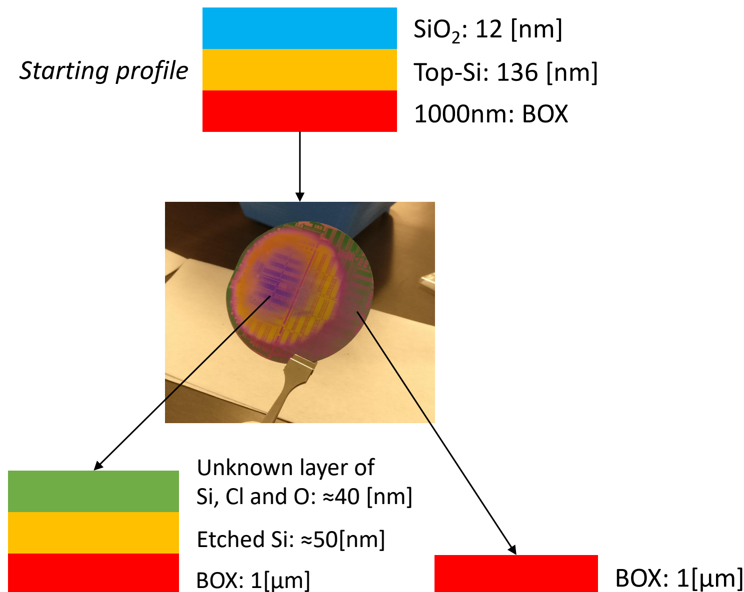

Figure 3.6: Picture of one of the wafer that underwent failure during the RIE etching. Two zones can be distinguished: a circular purple zone on the left and a green moon crescent-shaped zone on the right. Ellispometry on the wafer revealed a partial etching combined with the formation of an unknown layer on top of the Si on the left zone and a completed Si etching on the right zone.

Deposition of Si_3N_4 and creation of the actuators

As disclaimed at the beginning of this section, the microfabrication process was abruptly stopped by the Covid-19 crisis. The steps described from now on were not performed and are only theoretically described.
Once the Si specimens were carved from the top-Si layer, the SiO_2 mask should have been removed in a HF bath and the wafer would have subsequently been through a standard cleaning. Then, a $20[nm]$ thick oxide layer would have been grown on top of the entire wafer. A window would have been cut right on top of the overlap part of the Si specimens by positive photolithography, using the "Gen6overlap" mask. This window exposes the overlap part of the Si specimen so that the Si_3N_4 can be in direct contact with the specimen. Next, a $400[nm]$ thick Si_3N_4 layer should be deposited using Low Pressure Chemical Vapour Deposition (LPCVD) at 800°C. The Si_3N_4 would have been deposited on the front and back of the wafer, therefore requiring the back Si_3N_4 layer to be removed by SF_6 RIE. The front Si_3N_4 should have been patterned using a positive photolithography step and the "Gen6actuator" mask. The subsequent etching should have been performed with SF_6 RIE. Since SF6 etches silicon faster than silicon oxide, the oxide layer (between the top silicon and Si_3N_4) would have acted as an etch stop layer. Finally, a mix of acetone and IPA would have taken care of the remaining photoresist, leaving the completed structure ready to be released.

for the structures' release, the BOX would have been etched away by a highly concentrated HF solution. After the release, the wafer would be kept in a IPA solution and transferred to a critical point dryer. The critical point dryer avoids the collapse of the microstructures due to a stiction mechanism. Finally, the resulting, dry, structures should have been ready to be taken to an electron microscope or a Raman spectrometers for further analyses.

3.2.4 Microfabrication processes

Silicum oxidation

A step of silicium oxidation as been mentioned in the fabrication process of SOI lab-on-chip devices. Oxidation of silicium has been performed using a "dry" oxidation process at 900°C in a Koyo furnace. In a dry oxidation process, high temperature O_2 gas reacts on the wafer surface, according to the following reaction:

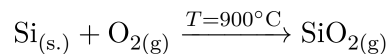

$$\mathrm{Si_{(s.)}} + \mathrm{O_{2(g)}} \xrightarrow{T=900^{\circ}\mathrm{C}} \mathrm{SiO_{2(g)}}$$

Thin film deposition

In the fabrication process of SOI lab-on-chip devices, a layer of Si_3N_4 is deposited using a Low Pressure Chemical Vapour Deposition (LPCVD) process. LPCVD deposition belongs the realm of thin-film deposition techniques using a Chemical Vapour Deposition (CVD) process, as opposed to Physical Vapour Deposition (PVD), such as sputtering, molecular beam epitaxy or evaporation. Silicon nitride LPCVD is performed at pressure around $10^{-6} Torr$ and $\approx$ 800°C by reaction between dichlorosilane and ammonia:

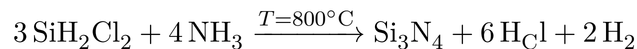

$$3\,\mathrm{SiH_2Cl_2} + 4\,\mathrm{NH_3} \xrightarrow{T=800^{\circ}\mathrm{C}} \mathrm{Si_3N_4} + 6\,\mathrm{H_Cl} + 2\,\mathrm{H_2}$$

Photolithography

Photolithography, along with other lithography techniques like nanoimprint lithography, electron beam lithography,.. is based on the principle of patterning the surface of a solid material at the microscopic level. With photolithography, a 2D pattern is transferred trough a patterned mask on a layer of photoresin, sitting over the wafer being processed. The pattern transfer is made possible by a light beamed though the mask that reacts though a photochemical process with the exposed part of the resin covering the wafer. The exposed part of the resin becomes either more soluble (positive photoresin) or less soluble (negative photoresin) than the unexposed resin. The photoresin is then treated with a solvent that selectively removes the exposed resin (positive photoresin) or the unexposed resist (negative photoresist) in a step called "development". This step is similar to the development of analogue photographs, hence its name. With the patterned photoresin above the substrate, many treatment are possible, from deposition of material over the patterned structure to create 3D surfaces, to a metal lift-off process or the etching of the underlying substrate. The complete process is decomposed into 7 steps, described on figure 3.7. In the Winfab cleanroom, photolithography is performed using UV light. For the fabrication process of SOI lab-on-chip devices, a positive resin has been used for every photolithography step. Furthermore, the only treatment applied after the pattern transfer from the mask to the photoresin have been etching processes. The etching processes used for the fabrication of the SOI lab-on-chip are described in the next paragraph.

Etching

Generally speaking, etching refers to the transfer of pattern from a structured resin to the substrate beneath it, as showed on figure 3.7, by means of chemical or physical removal. Two kinds of etching processes are available in the Winfab cleanroom, wet and dry etching. Wet etching refers to the selective chemical removal of solid compounds using a chemical agent. Wet etching has been used to remove silicon oxide, using either concentrated hydrogen fluoride (HF) or a buffered HF solution (BHF).

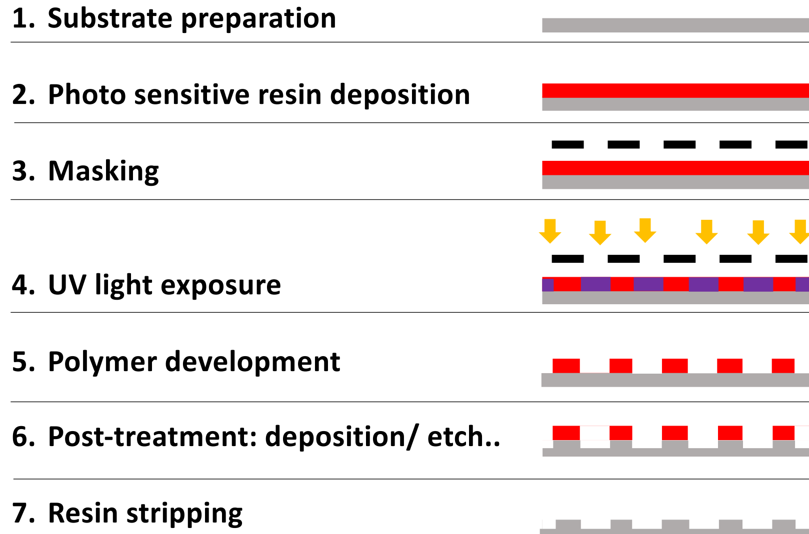

Figure 3.7: Photolithography process in 7 steps, the post-treatment step is an etching step.

HF is highly selective towards SiO_2 which means that the etch rate of SiO_2 is much more important than the one of the other compounds surrounding it, for instance Si and Si_3N_4. However, wet etching is often an isotropic etching process, where the walls of the etched material are altered, as showed on figure 3.8. As cited earlier, Si specimens need to be precisely carved out from the top-Si, therefore an anisotropic etching process is required. Anistropic etching of silicon can be achieved using dry etching, or plasma etching. In the plasma etching equipment used in the Winfab facilities, a $Cl_2 + O_2$ plasma is generated inside the etching chamber and ions are accelerated towards the wafers by means of an electric field. Si is then etched by ion bombardement, resulting in anisotropic eching profiles. The $Cl_2 + O_2$ plasma etching is also highly selective towards Si.

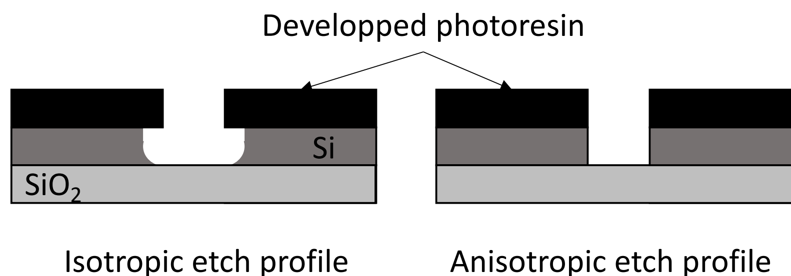

Figure 3.8: Isotropic versus anisotropic etched of Si

Critical point dryer

The critical point dryer (CPD) is a device essential for the release of on-chip tensile testing devices. Normal drying of the IPA solution in which the released structures are kept cause a stiction phenomenon that can cause of collapse of the suspended thin films. The CPD avoids this issue by using the supercritical fluid state of CO_2. In the CPD, IPA is replaced by liquid CO_2, then the pressure and temperature are elevated higher than the critical point of CO_2: $T > 31.1°\text{C}$ and $p > 74[bar]$. The transition between liquid and supercritical CO_2 has no impact on the stiction of CO_2 and the structure, as supercritical fluids are indistinguishable from neither gases or liquids. The pressure and temperature are then brought back to athmospheric conditions where CO_2 is gaseous, following a different path on the (p, T) diagram, as represented on figure 3.9.

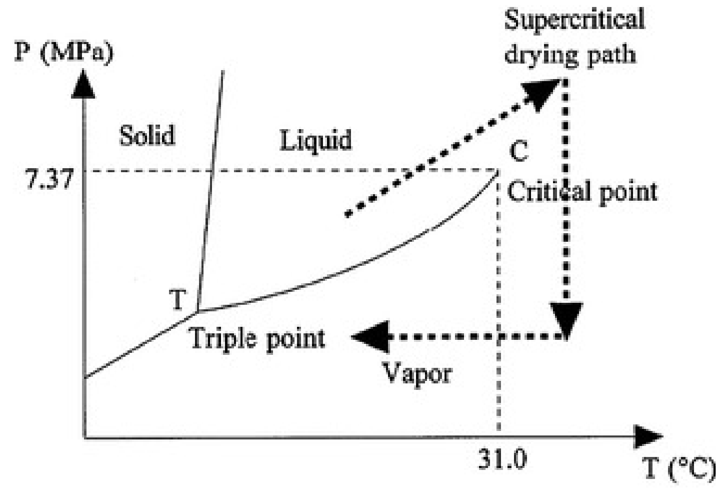

Figure 3.9: CO_2 critical point drying represented on a (p, T) diagram, from [49]

Characterisation: Ellipsometry

A few characterisation methods are also used along the fabrication process of SOI lab-on-chip devices. Ellipsometry is one of them, it allows the non-destructive measurement of the thickness of a single thin film or multiple layers of thin films with great accuracy. Ellipsometry devices shine a linearly polarised beam of light onto the surface of the specimen and measures the change of polarisation upon reflection. The polarisation change is measured through two parameters, the amplitude ratio Ψ and phase difference Δ and depends on optical properties and thickness of the specimen. As optical properties of usual semiconducting materials are known, ellipsometry is well suited to measure thin film thicknesses. More specifically, the ellispometer measures the complex reflectance ratio ρ, a function of both the amplitude ratio Ψ and phase difference Δ:

$$\rho = tan(\Psi)e^{i\Delta} \tag{3.16}$$

Then, ρ is compared to a model. Comparison of the measured data with the model yields the thickness and optical properties of individual layers of materials. [50]

Characterisation: Profilometry

Profilometry is another characterisation technique often used in the fabrication of SOI lab-on-chip devices. Profilometry is used to measure the curvature of a substrate through a measurement of the maximal deflection h_{max} of the substrate:

$$R = \frac{L^2/4}{2h_{max}} \tag{3.17}$$

Evaluating the curvature before and after the deposition of a thin film over a substrate enables the calculation of the internal stress present inside the thin film, using the Stoney formula:

$$\sigma_f = \frac{1}{6}\frac{E_s}{1-\nu_s}\frac{t_s^2}{t_f}\left(\frac{1}{R} - \frac{1}{R_0}\right) \tag{3.18}$$

Which can in turn be used to evaluate the mismatch strain of a deposited film:

$$\varepsilon_{mis,f} = \sigma_f \frac{1-\nu_f}{E_f} \tag{3.19}$$

Chapter 4

Development of a new data reduction scheme for lab-on-chip devices

This chapter deviates from the previous ones, which focused on the strain engineering of silicon and germanium. The reason why this chapter diverges from the main subject of this master thesis is directly linked to the Covid19-related crisis in Belgium. Indeed, the Covid-19 crisis and its subsequent confinement and lockdown measures prohibited any access, nor to the clean room facilities, nor to any type of spectroscopy equipment available on the UCLouvain campus. Therefore, as the study of strain engineering in Si and Ge required both microfabrication processes and photoluminescence spectroscopy, it had to be dropped in favour of another, more "home working-friendly" study.

This "home working-friendly" study came in the form of the development of an upgraded data reduction scheme for on-chip tensile testing devices. More specifically, the work presented here builds up on the latest data reduction schemes for on-chip tensile tests and upgrades it by applying a revised correction model. This upgrade is based on material mechanics and implemented using the Python programming language. An application of the new data reduction scheme is shown on the figure below, as an illustration.

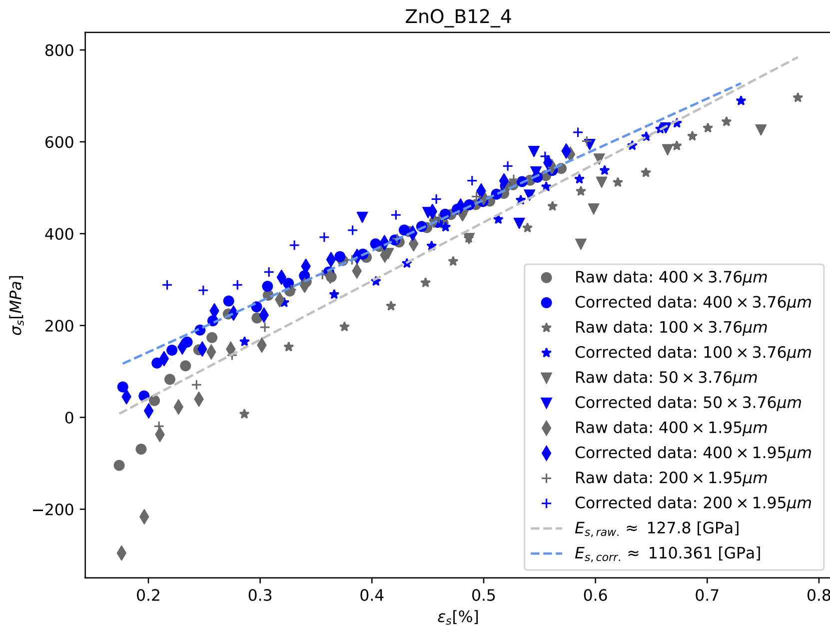

Figure 4.1: Illustration: application of the data reduction scheme on experimental data from lab-on-chip devices. Blue data has been treated with the correction model.

4.1 A data reduction scheme for lab-on-chip devices

The scope of this work is introduced in this section, then the correction model is developed from section 4.2 to section 4.4 and finally, results are presented and discussed in section 4.5.
This introduction briefly explains why the current way of making measurements on on-chip tensile testing devices is flawed and what can be done to fix it. First, a clarification of the "data reduction scheme" terminology is given.

What is a data reduction scheme?

Data reduction covers the transformation of raw data into a more convenient, corrected and ordered form. Data reduction is the process that, for instance, allows experimental data to be transformed into something easier to make interpretations from, such as a chart. In the case of the lab-on-chip devices, the raw data are the displacements of the thin-film samples after their release. These displacements are directly measured on the devices. On the other hand, the corrected, ordered data takes the form of stress-strain curves.

How is it applied to the on-chip testing devices?

As stated in the previous chapter, the displacement between the sample and the actuator "u" can be measured on the lab-on-chip devices. Up to now, a basic data reduction scheme was applied on these measurements. This archaic reduction scheme computes stresses and strains from the measurements of u by simplifying the structure down to two adjacent rectangular beams perfectly connected and perfectly clamped on two external fixed parts. This simplification implies that the measured displacement u corresponds to the true displacement of the sample, denoted as "u_g": $u = u_g$. However, the real geometry of the structure differs from this model:

- The sample is not rectangular, but possess a dog-bone shape. At each extremity of the sample lies a dog-bone element that behaves in a different manner than the sample when strain is applied on the structure.
- The anchor points of the sample and actuator become free-standing during the release process. Therefore, a certain area around both the anchor points contributes to the overall displacement of the structure.
- The overlap region between the sample and actuator also contributes to the overall displacement of the structure.

The contributions of these free-standing parts on u are not negligible. Therefore, it is now clear that u does not correspond to the true displacement of the sample u_g. Actually, the measured displacement u corresponds to the sum of the displacements of multiple individual elements of the structure, including u_g. The behaviour of the sample upon release is better described by a decomposition of the measured displacement u into the displacements of individual segments, as illustrated on figure 4.2.

The work done in this master thesis addresses this issue, by building a **correction model** able to evaluate u_g from the measurement of u, as accurately as possible through an accurate modelling of the structure's mechanical behaviour. To do so, the improved data reduction scheme presented in this master thesis builds on previous work done by *Vayrette et al. (2015), Ghidelli et al. (2017)* and *Lemoine (2018)*. These works paved the way to create the correction model that is introduced in the next sections. [51, 47, 46]

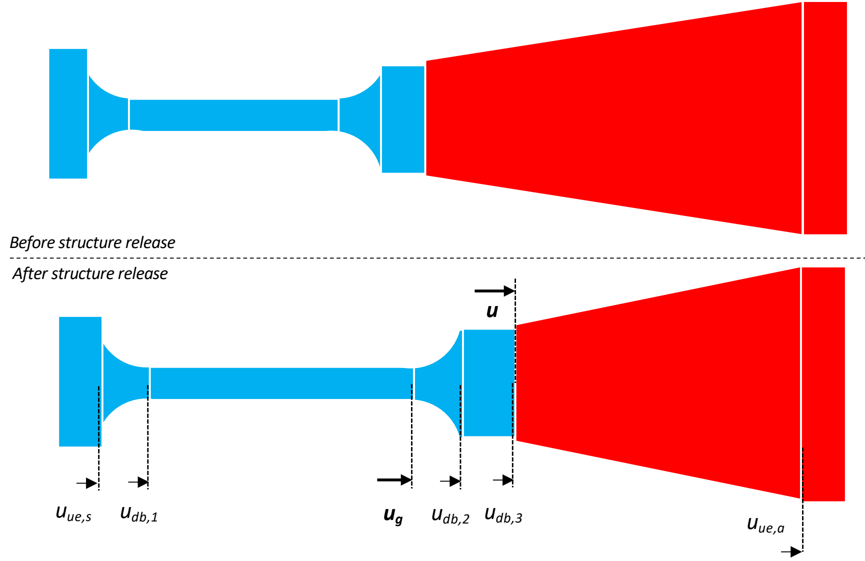

Figure 4.2: Schematic decomposition of the displacement u into the displacements of smaller, distinct, elements.

4.2 The analytical correction model

In this section, the analytical correction model behind the data reduction scheme is presented. This model performs the two tasks of:

1. Correcting the input data, from the measurement of the total, measured, displacement "u" to the displacement of the sample only "u_g"
2. Processing the corrected data, from the sample displacement "u_g" to the corresponding stress and strain values ($\sigma, \varepsilon^{mech.}$).

A schematic representation of both the top and side view of the on-chip tensile test device are drawn on figure 4.3 and figure 4.4. These drawings illustrate all the dimensions of the structure that are relevant in this work. An overview of the data reduction scheme is shown on figure 4.5. The final model is presented in section 4.4

Before delving into the model, some general notations and relations have to be introduced. The displacement u, experimentally measured at the rightmost part of the sample, corresponds to both the displacement of the sample and the actuator after their release. Furthermore, u can be decomposed into the sum of the displacement of individual segments:

$$u = u_g + u^s_{ue} + 2u_{db,1} + u_{db,3} \qquad \text{(Sample side)} \qquad (4.1)$$

$$u = u^a_g + u^a_{ue} \qquad \text{(Actuator side)} \qquad (4.2)$$

The subscripts "^{a}" refers to elements of the structure on the actuator side while "^{s}" refers to the elements on the sample side (red and blue parts in the drawings of the structure, respectively). u^s_{ue} and u^a_{ue} refer to the displacement of the under etched segments on both sides, u^a_g refers to the displacement of the actuator (gauge), $u_{db,3}$ and $u_{db,1}/_{db,2}$ refer to the displacement of the overlap region and the dogbones elements, respectively. A positive displacement value for any part of the structure means that the part extends in the (1) direction, the direction of the actuator's retraction.

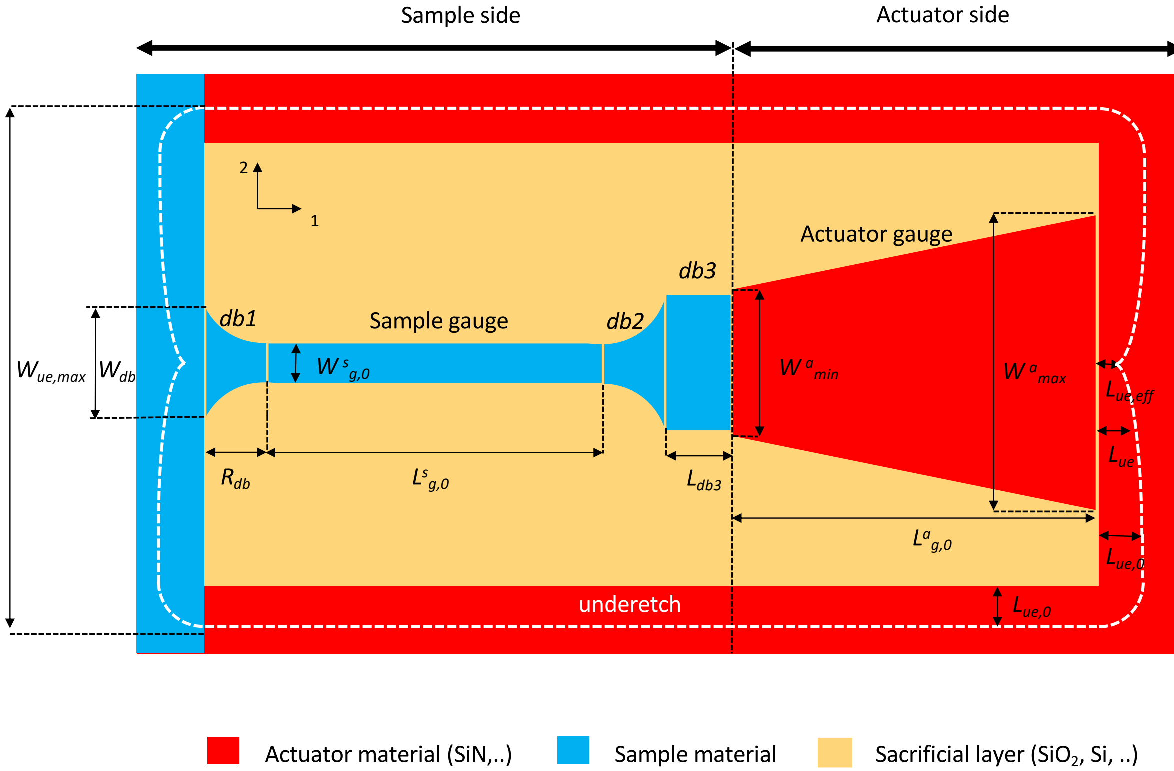

Figure 4.3: Schematic representation of an on-chip tensile test structure, top view. The white dashed line delimits the under-etched zone. The zone inside the white dashed line is considered to be suspended.

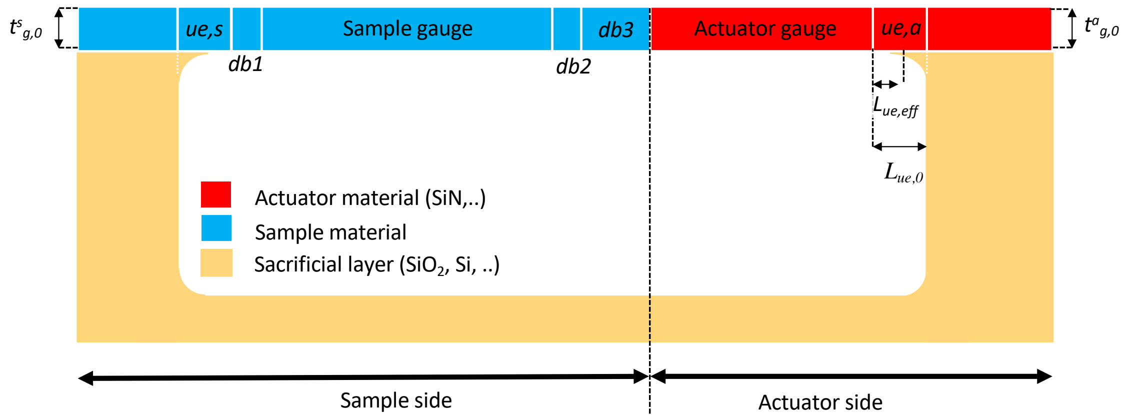

Figure 4.4: Schematic representation of an on-chip tensile test structure, side view. The under-etch profile is represented as a curved edge below the "under-etch" parts of the actuator ue, a and sample "ue, s.

4.2.1 Modelling the actuator side

Here, an expression for the tensile force at equilibrium F is derived from the decomposition of the displacements in the actuator zone. This force is exerted by the actuator on the sample. A good evaluation of the tensile force at equilibrium is the first step towards a valid correction of the stress and strain in the sample.
Considering the actuator side of the structure, they are two distinct parts that contributes to the overall displacement once the structure is released:

- The actuator itself, that retracts once the structure is released. It retracts because of its high internal stress. This internal stress comes from the difference in thermal dilatation coefficient

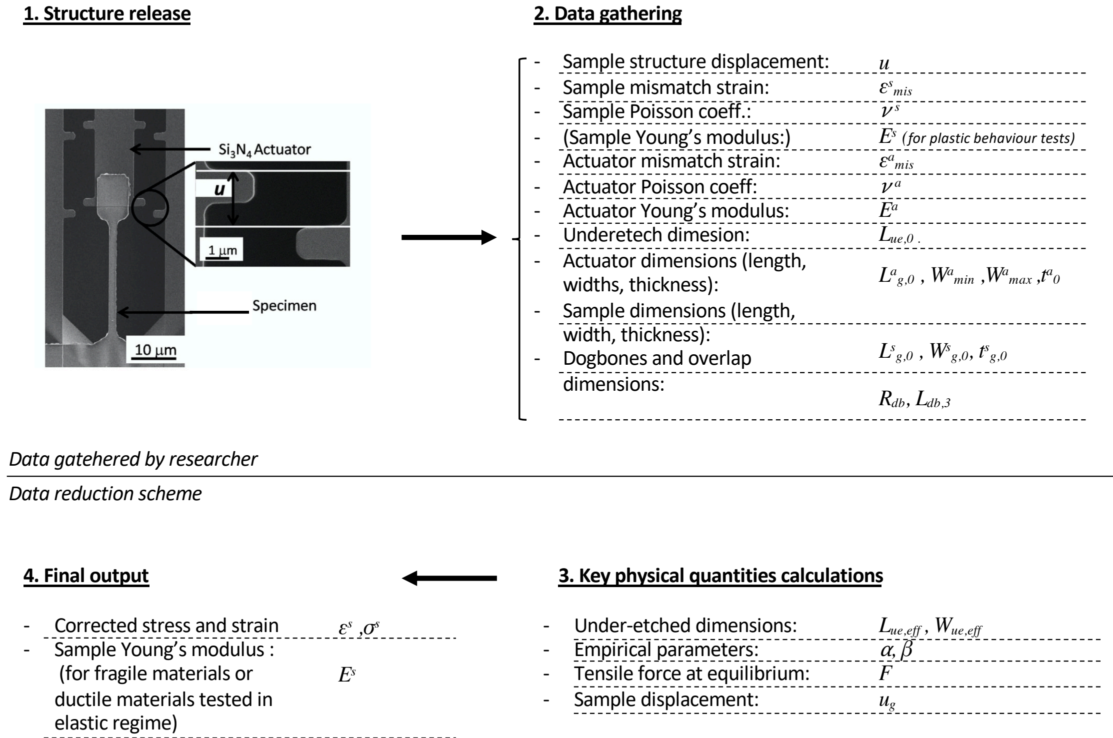

Figure 4.5: General diagram illustrating how the data reduction scheme is applied. The picture of the structure is from [47]

between the actuator material and the sacrificial layer (SiN for instance is deposited at $T \approx 800°$C. Its displacement is denoted as u^a_g;

- The "under-etched" part of the window around the structure that becomes suspended during the release process. This "under-etch" zone is somewhat delimited by the white dashed line on figure 4.3. It acts as an extension of the actuator, as it also retracts during the release process, for the same reason as the actuator. the displacement of this under-etch zone is denoted as u^a_{ue}. The description of this displacement is not trivial and is subject to hypotheses.

Therefore, the following relation for the strain in the actuator region can be derived:

$$u = u^a_g + u^a_{ue} \tag{4.3}$$

$$u = \varepsilon^a_g L^a_{g,0} + \varepsilon^a_{ue} L_{ue} \tag{4.4}$$

where $L^a_{g,0}$ is the initial length of the actuator, L_{ue} the length of the under etched region of the surrounding frame. To find an appropriate expression of the strains ε^a_g, ε^a_{ue} and under-etch length L_{ue}, some hypothesis are used. These hypothesis will be cited and described one after the other, until an appropriate expression of the tensile force is found. The validity of the hypothesis is discussed when results are presented.

Hypothesis 1: The actuator deforms elastically and its section decreases because of the Poisson effect

To simplify the model, the tapered actuator is described by a rectangular beam of equal length and width corresponding to the effective width of the trapeze-shaped actuator $W^a_{g,eff,0}$:

$$\varepsilon^a_g = \frac{\sigma^a}{E^a} = \frac{F}{E^a A^a_{g,eff}} \tag{4.5}$$

$$A^a_{g,eff} = W^a_{g,eff} t^a_g = W^a_{g,eff,0} t^a_{g,0}(1 + \varepsilon^a_{mis.} - \nu^a \varepsilon_g^{a,el(1)})(1 - \nu^a \varepsilon_g^{a,el(1)}) \tag{4.6}$$

Where the terms highlighted in blue require more attention. Firstly, the strain $\varepsilon_g^{a,el(1)}$ itself depends on the tensile force F that is not yet described. This issue is taken care of in the implementation of the model, using iterative methods and a first estimation of the under etch section $A^a_{g,eff,0} = W^a_{g,eff,0} t^a_{g,0}$.

Secondly, the initial effective width $W^a_{g,eff,0}$ of the actuator simplified to a rectangular beam is unknown. One way to describe it is to assume that the actuator is made up of successive springs, with length dx and width $W(x)$. This process might seem tedious, nonetheless the emphasis is on accuracy rather than speed of execution. Therefore, the succession of spring that make up the actuator have a total spring constant k_{tot} given by:

$$\frac{1}{k_{tot}} = \frac{L^a_{g,0}}{t^a E^a W^a_{g,eff,0}} = \frac{1}{t^a E^a} \int_0^{L^a_{g,0}} \frac{dx}{W(x)} \tag{4.7}$$

Where, $W(x)$ for a trapeze is given by $\frac{x(W^a_{max} - W^a_{min})}{L^a_{g,0}}$. Thus, the initial effective width of the trapezoid-shaped actuator $W^a_{g,eff,0}$ can be written as

$$\frac{L^a_{g,0}}{W^a_{g,eff,0}} = \int_0^{L^a_{g,0}} \frac{dx}{W(x)} = L^a_{g,0} \frac{ln(\frac{W^a_{max}}{W^a_{min}})}{W^a_{max} - W^a_{min}} \tag{4.8}$$

$$\Rightarrow W^a_{g,eff,0} = \frac{W^a_{max} - W^a_{min}}{ln(\frac{W^a_{max}}{W^a_{min}})} \tag{4.9}$$

Which is translated into the width of the rectangular beam that replaces the tapered actuator in the correction model. Finally, the effective section of the actuator is given by the following relation:

$$A^a_{g,eff} = ln\left(\frac{W^a_{max}}{W^a_{min}}\right) \frac{t^a_{g,0}}{W^a_{max} - W^a_{min}} (1 + \varepsilon^a_{mis} - \nu^a \varepsilon_g^{a,el(1)})(1 - \nu^a \varepsilon_g^{a,el(1)}) \tag{4.10}$$

Hypothesis 2: The under-etched part can be described by a rectangular shape and the strain in the (2) direction is null.

The direction of the tensile test is denoted as (1) and direction (2) is perpendicular to (1) along the surface of the device. Plane stress is considered.

$$\varepsilon_{ue}^{a,(1)} = \varepsilon_{ue}^{a,el,(1)} + \varepsilon^a_{mis} \tag{4.11}$$

$$\varepsilon_{ue}^{a,(2)} = \varepsilon_{ue}^{a,el,(2)} + \varepsilon^a_{mis} = 0 \tag{4.12}$$

Where the elastic strains are described as:

$$\varepsilon_{ue}^{a,el,(1)} = \frac{\sigma_{ue}^{a,(1)}}{E^a} - \nu^a \frac{\sigma_{ue}^{a,(2)}}{E^a} \tag{4.13}$$

$$\varepsilon_{ue}^{a,el,(2)} = \frac{\sigma_{ue}^{a,(2)}}{E^a} - \nu^a \frac{\sigma_{ue}^{a,(1)}}{E^a} = -\varepsilon^a_{mis} \tag{4.14}$$

And, for an uniaxial tensile test, the stress is written as:

$$\sigma_{ue}^{a,(1)} = \frac{F}{A^a_{ue,eff}} \tag{4.15}$$

In the end, a combination of the previous equations yields:

$$\varepsilon_{ue}^{a,(1)} = \varepsilon_{ue}^{a} = \frac{F}{A_{ue,eff}^{a}E^{a}}(1-(\nu^{a})^{2}) + \varepsilon_{mis}^{a}(1+\nu^{a}) \tag{4.16}$$

The effective under-etched region section $A_{ue,eff}^{a}$ is subject to a third hypothesis:

Hypothesis 3: The effective section of the under-etched region $A_{ue,eff}^{a}$ is independent of the strain.

$$A_{ue,eff}^{a} = A_{ue,eff,0}^{a} = t_{g,0}^{a}W_{max}^{a} \tag{4.17}$$

The combination of the hypotheses' results with equation (4.3) leads to the **first form of the tensile force's model**:

$$F = -E^{a}\left(\frac{u+\varepsilon_{mis}(L_{g,0}^{a}+L_{ue}(1+\nu^{a}))}{\frac{L_{g,0}^{a}}{A_{g,eff}}^{a} + \frac{L_{ue}(1-(\nu^{a})^{2})}{W_{max}^{a}t_{g}^{a}}}\right) \tag{4.18}$$

The length of the under-etched segment L_{ue}, in blue, still needs to be properly described.

Length of the under-etch segment

The length over which the under-etched region is effectively suspended and acts as an extension of the actuator is expressed as L_{ue}. However, the true value of L_{ue} is not known. It lies somewhere between two extreme values:

1. $L_{ue} = L_{ue,0}$. In this case we consider that the effective length of the under-etch to be the maximum under-etch length. This length is simply obtained from the release process parameters $L_{ue,0} = v_{etch}.t_{etch}$
2. $L_{ue} = L_{ue,eff}$. This time, we consider the effective length of the under-etched segment to be the distance between the actuator and the "chin" of the under-etch region. This "chin" is visible in figure 4.4, and is a result of the isotropic etching of the sacrificial layer under the actuator and its anchor point. This length can be evaluated through some basic trigonometry.

One should note that $L_{ue,eff} < L_{ue,0}$.

With those two extreme values in mind, we can express the effective length L_{ue} to be a modulated version of $L_{ue,0}$ and we introduce the first empirical parameter α:

$$L_{ue} = \alpha L_{ue,0} \qquad \text{Where } \alpha \in \left[\frac{L_{ue,eff}}{L_{ue,0}}, 1\right] \tag{4.19}$$

Which can be translated in terms of the displacement u_{ue}^{a}:

$$u_{ue}^{a} = \alpha L_{ue,0}\varepsilon_{ue}^{a} \tag{4.20}$$

Final model of the tensile force

With the addition of the α parameter the final form of tensile force model is obtained:

$$F = -E^{a}\left(\frac{u+\varepsilon_{mis}(L_{g,0}^{a}+\alpha L_{ue,0}(1+\nu^{a}))}{\frac{L_{g,0}^{a}}{A_{g,eff}^{a}} + \frac{\alpha L_{ue,0}(1-(\nu_{a})^{2})}{W_{max}^{a}t_{g}^{a}}}\right) \qquad \text{Where } \alpha \in \left[\frac{L_{ue,eff}}{L_{ue,0}}, 1\right] \tag{4.21}$$

Section 4.3 will be dedicated to the fine-tuning of the model through the optimisation of the α parameter.

4.2.2 Modelling the sample's side

The next steps are the development of a model for the sample's displacement u_g, strain and finally stress. Just like the tensile force F, the displacement of the sample u_g should be precisely evaluated.

First of all, the decomposition of the measured displacement into individual segments can be expressed in terms of strains:

$$u = u_g + u^s_{ue} + 2u_{db,1} + u_{db,3} \tag{4.22}$$

$$u = u_g + \varepsilon^s_{ue} L_{ue,0} + 2\varepsilon_{db,1} R_{db,1} + \varepsilon_{db,3} L_{db,3}$$

$$u_g = u - \varepsilon^s_{ue} L_{ue,0} - 2\varepsilon_{db,1} R_{db,1} - \varepsilon_{db,3} L_{db,3} \tag{4.23}$$

In the last equation, u_g has been isolated and the strain inside the other segments need to be described. In order to do this, two new hypotheses are proposed.

Hypothesis 4: the dog bone region and overlap region stay elastic and under uniaxial tension

$$\Rightarrow \varepsilon_{db,1} = \varepsilon^{el}_{db,1} + \varepsilon^s_{mis} = \frac{1}{E^s} \frac{F}{t^s W_{db,eff}} + \varepsilon^s_{mis}$$

$$\Rightarrow \varepsilon_{db,3} = \varepsilon^{el}_{db,3} + \varepsilon^s_{mis} = \frac{1}{E^s} \frac{F}{t^s W_{db,3}} + \varepsilon^s_{mis}$$

Hypothesis 5: the under-etch region of the sample side behaves in a similar way than the one on the actuator side:

Consequently, the under-etched part can be described by a rectangular shape and the strain in its horizontal direction is null. The development of this hypothesis is similar to the one of hypothesis 2, with the effective section $A_{ue,eff,s}$ of under etched region being described differently.

$$\Rightarrow \varepsilon_{ue,s} = \frac{(1-(\nu^s)^2)}{E^s} \frac{F}{t^s W_{ue}} + \varepsilon^s_{mis}(1+\nu^s)$$

Combining these hypotheses to equation (4.22), a first model for the sample displacement can be written:

$$u_g = u - 2R\left(\frac{1}{E^s}\frac{F}{t^s W_{db,eff}} - \varepsilon^s_{mis}\right) - L_{db3}\left(\frac{1}{E^s}\frac{F}{t^s W_{db}} + \varepsilon^s_{mis}\right) - \dots \tag{4.24}$$

$$\dots - L_{ue,0}\left(\frac{1-(\nu^s)^2}{E^s}\frac{F}{t^s W_{ue}} + \varepsilon^s_{mis}(1+\nu^s)\right)$$

Where the Young's modulus E^s, the effective dog bone width $W_{db,eff}$ and the under-etched region width W_{ue}, highlighted in blue, require more attention.

Width of the under etched region in the sample side

In the same spirit as the previously discussed under-etched length L_{ue}, the width W_{ue} of the under-etched region in the sample side requires a description. One could ask, why is the width unknown here, rather than the length L_{ue} as discussed for the α parameter. Why not apply the β parameter to the under-etched region's length L_{ue}, instead of the under-etched region's width W_{ue}? This would, after all, make the model more coherent as a whole. Unfortunately, this path has been tried in the background of this master thesis and yielded poor results at the very end of the data reduction.
The width of the under-etched region W_{ue} is believed to lie somewhere between two different extreme values:

1. $W_{ue} = W_{ue,max}$: the under-etched part that contributes to the total displacement of the structure is delimited by the rectangle of dimensions $W_{ue,max} \times L_{ue,0}$.
2. $W_{ue} = W_{db}$: in this scenario, the under-etched part that contributes to the total displacement of the structure is delimited by the rectangle of dimensions $W_{db} \times L_{ue,0}$

Similarly as with the α parameter, a $\boldsymbol{\beta}$ parameter is introduced. The effective width is consequently obtained as:

$$W_{ue} = \beta W_{db} \quad \text{where} \quad \beta \in \left[1, \frac{W_{ue,max}}{W_{db}}\right] \tag{4.25}$$

And therefore, the displacement of the under-etched part can be described by:

$$u^s_{ue} = L_{ue,0}\left(\frac{1-(\nu^s)^2}{E^s}\frac{F}{tW_{db}\beta} + \varepsilon^s_{mis.}(1+\nu^s)\right) \quad \text{where} \quad \beta \in \left[1, \frac{W_{ue,max}}{W_{db}}\right] \tag{4.26}$$

Young's modulus of the sample

As stated earlier, when a brittle material is tested with the on-chip tensile test, its Young's modulus is previously unknown. The purpose of the micro-scale tensile test is precisely to measure this E^s, when other caracterisation method are unavailable or not precise enough. Therefore it makes no sense to include it in the model before the calculations of the stress and strains. However, a trick is used here. In the implementation of this model, some numerical methods are involved to deal with this issue and provide a good estimation of E^s, mainly iterative methods.

Effective width of the dogbones

Just like the tapered actuator, the dog bones can be replaced by a rectangular beam. This rectangular beam has the same length as the dog bones but its width is the effective width of the real dog bones. Again, one way to proceed is to assume that the dog bone is made up of successive springs, with length dx and width $W(x)$. Therefore, the succession of spring that make up the dog bone have a total spring constant k_{tot} given by:

$$\frac{1}{k_{tot}} = \frac{1}{t^s E^s W_{db,eff}} = \frac{1}{t^s E^s}\int_0^{R_{db}} \frac{dx}{W(x)} \tag{4.27}$$

With the help of trigonometry and the figure 4.6, one can express the width $W(x)$ as:

$$W(x) = W_{db} - 2\sqrt{2R_{db}x - x^2} \tag{4.28}$$

Without delving into the calculus required to solve the integral, the effective dog bone width is given by:

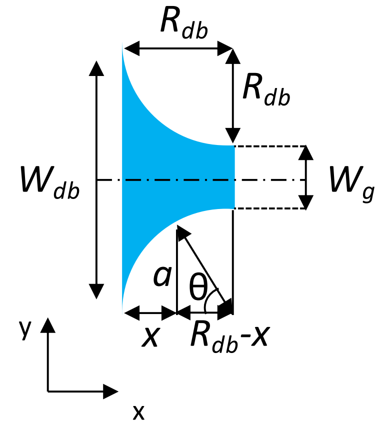

Figure 4.6: Schematic representation of the dog bone element, with key dimensions.

$$W_{db,eff} = \frac{R_{db}}{A} \tag{4.29}$$

Where A is the result of the integral $\int_0^R \frac{dx}{W(x)}$. The dog bone is now replaced by a rectangular beam of length R_db and width $W_{db,eff}$

Final model of the sample displacement

The developpement of $W_{db,eff}$ and the introduction of the parameter β lead to the final model of the sample displacement:

$$u_g = u - (2u_{db1} + u_{db3} + u^s_{ue}) \tag{4.30}$$
$$= u - 2R_{db}\left(\frac{1}{E^s}\frac{F}{t^sW_{db,eff}} - \varepsilon^s_{mis.}\right) - L_{db,3}\left(\frac{1}{E^s}\frac{F}{t^sW_{db}} + \varepsilon^s_{mis.}\right) - ...$$
$$... - L_{ue,0}\left(\frac{1-(\nu^s)^2}{E^s}\frac{F}{tW_{db}\beta} + \varepsilon^s_{mis.}(1+\nu^s)\right) \quad \text{where} \quad \beta \in \left[1, \frac{W_{ue,max}}{W_{db}}\right]$$

Stress and strain

Once the tensile force at equilibrium and the sample displacement have been properly described, it is possible to proceed to the description of the stress and strain.

$$\varepsilon^{mech}_g = \varepsilon_g - \varepsilon^s_{mis} = ln\left(\frac{L_{g,0} - u_g}{L_{g,0}}\right) - \varepsilon^s_{mis} \tag{4.31}$$

$$\sigma_g = \frac{F}{A^{eff}_g} = \frac{F}{W^s_{g,0}t_{g,0}(1 + \varepsilon^s_{mis} - \nu_s\varepsilon^{mech}_g)(1 - \nu_s\varepsilon^{mech}_g})) \tag{4.32}$$

Finally, for a brittle sample or in the elastic regime of a ductile sample, it is the also possible to describe the Young's modulus of the sample:

$$E^s = \frac{\sigma_g}{\varepsilon^{mech}_g} = \frac{F}{W^s_{g,0}t_{g,0}(1 + \varepsilon^s_{mis} - \nu_s\frac{u_g}{L_{g,0}})(1 - \nu_s\frac{u_g}{L_{g,0}})(\frac{u_g}{L_{g,0}} - \varepsilon^s_{mis})} \tag{4.33}$$

Finally, the set of equations that make up the mathematical model behind the data reduction scheme is given by:

$$\begin{cases} F = -E^a\left(\dfrac{u + \varepsilon_{mis}(L^a_{g,0} + \alpha L_{ue,0}(1+\nu^a))}{\frac{L^a_{g,0}}{A^a_{g,eff}} + \frac{\alpha L^a_{ue,0}(1-(\nu^a)^2)}{W^a_{max}t^a_g}}\right) \\ u_g = u - 2R\left(\dfrac{1}{E^s}\dfrac{F}{t^sW_{db,eff}} - \varepsilon_{mis.}\right) - L_{db,3}\left(\dfrac{1}{E^s}\dfrac{F}{t^sW_{db}} + \varepsilon_{mis.}\right) - ... \\ \qquad ... - L_{ue,0}\left(\dfrac{1-\nu^2}{E^s}\dfrac{F}{tW_{db}\beta} + \varepsilon_{mis.}(1+\nu)\right) \\ \varepsilon^{mech}_g = ln\left(\dfrac{L_{g,0} - u_g}{L_{g,0}}\right) - \varepsilon^s_{mis} \\ \sigma_g = \dfrac{F}{W^s_{g,0}t_{g,0}(1 + \varepsilon^s_{mis} - \nu_s\varepsilon^{mech}_g)(1 - \nu_s\varepsilon^{mech}_g)} \\ E^s = \dfrac{\sigma_g}{\varepsilon^{mech}_g} = \dfrac{F}{W^s_{g,0}t_{g,0}(1 + \varepsilon^s_{mis} - \nu_s\frac{u_g}{L_{g,0}})(1 - \nu_s\frac{u_g}{L_{g,0}})(\frac{u_g}{L_{g,0}} - \varepsilon^s_{mis})} \end{cases}$$

Where, thanks to the hypotheses, the device's structure has been simplified in a 7-segments structure, as illustrated below on figure 4.7. α and β are still unknown parameters, within a certain range. Next section is dedicated to their modelling using some reference data.

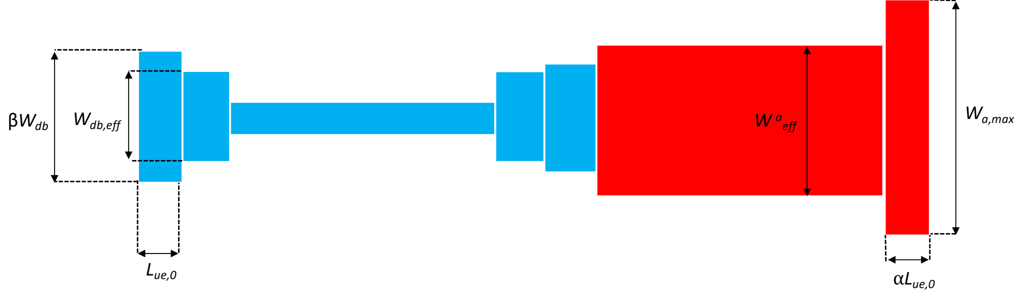

Figure 4.7: Simplification of the device's structure used as a basis for the correction model, with the α and β parameters highlighted

4.3 Linking the model to FE predictions

This section links the analytical correction model to the results of a finite element (FE) simulation of the on-chip test structure. First, the results of this FE simulation will be briefly described, then the model will be assessed towards the FE results, through the manipulation of the α and β parameters. In other words, the results of the FE simulations are used as references to tune the analytical correction model through the α and β parameters.

In fine, suggested models for the α and β parameters are listed on table 4.1. They are designated by α_{approx} and β_{approx} and are a function of h, a mapping of the sample and actuator dimensions. The steps required to obtain these models are described along this section.

Brittle samples:	$\alpha_{approx} = \begin{cases} 0.950 & \text{if } h > 0.01 \\ \dfrac{0.885h}{(7.520 * 10^{-5}) + h} & \text{if } h \in [10^{-4}; 0.01] \\ \dfrac{0.940h}{(1.250 * 10^{-4}) + h} & \text{if } h < 10^{-4} \quad \text{(Unstable!)} \end{cases}$	$h = \frac{L^s_{g,0} W^s_{g,0}}{(L^a_{g,0})^2}$
	$\beta_{approx}(h) = 1.503 - 0.404e^{-8.026h}$	$h = \frac{L^s_{g,0}}{L^a_{g,0}} e^{-W^s_{g,0}}$
Ductile samples:	$\alpha_{approx} = 0.942 - (1,213e * 10^{-4})h$	$h = L^a_{g,0}$
	$\beta_{approx}(h) = 0.623 + 0.404e^{-5,17h}$	$h = \frac{L^s_{g,0}}{L^a_{g,0}} e^{-W^s_{g,0}}$

Table 4.1: Models for α and β parameters: $\alpha_{approx}(h)$ and $\beta_{approx}(h)$

4.3.1 Overview of the reference data

A few finite elements simulations[1] of the on-chip tensile test with various geometries and for different samples have been performed. These simulations generated a set of results, namely the equilibrium tensile force in the actuator and the displacements of each segment in the structure. Together, these results form the reference data. They are considered as reference because a FE simulation is an accurate and reliable estimation of the distinct displacements inside the on-chip tensile testing machine.
The simulation resulted in accurate evaluations of the equilibrium tensile force and displacements of individual segments forming the lab-on-chip device, namely:

- The under-etched region, on the sample side u^s_{ue}
- The dog-bones $u_{db,1,2}$
- The overlap region $u_{db,3}$

[1] Performed on the Abaqus software

- The sample u_g
- The total, measured displacement u

In the calculations presented next, the displacement u provided in the reference data is used as an equivalent to the experimental input of the data reduction scheme. Two sets of data are provided by those simulations, respectively corresponding to a tensile test performed on a brittle (ZnO) and ductile (Pd) material. Inside these two sets, the results are differentiated by different combinations of the structure geometry, as showcased in table 4.2.

$L_{g,0}[\mu m]$	$W^s_{g,0}[\mu m]$	$L^a_{g,0}[\mu m]$	$t^a_{g,0}[\mu m]$	$t^s_{g,0}[\mu m]$
50	1.5	50	1	1
100		100		
400		150		
		1500		

Table 4.2: Dimensions of the actuator and sample in FE simulations

4.3.2 Optimisation and modelling of the α parameter

The goal here is to use the reference data to find an approximate model of the α parameter, appearing in equation (4.21). A considerable effort is dedicated to this task, indeed a correct α model is crucial for the accuracy of the data reduction scheme. Moreover, this model should be applicable to a broad range of sample and actuator geometries.

Tensile force and α

The first step consists in the investigation of the α parameter to highlight which values of α minimises any error made by the correction model. Figure 4.9 shows the error between the force from equation (4.21) and the reference data, as function of the parameter α, in the case of a ductile (top) and brittle material (bottom).
Points where the curves intersects the $\frac{F-F_{ref}}{F_{ref.}} = 0$ correspond the optimum value of α, with respect to the sample and actuator geometry. These specific values of α are designated as "$\alpha_{min,i}$" where the index i refers to the sample and actuator dimension combination (see table 4.2). One can observe that, the longer the actuator, the smaller the $\alpha_{min,i}$ gets. This tendancy is respected for any geometry combination and brittle or ductile sample, with some level of disparity, the most spread out case being the one illustrated on the bottom of figure 4.9. In this particular case, the brittle sample with a $L^a_{g,0} = 50 \times W^s_{g,0} = 4.0/L^a_{g,0} = 1500[\mu m]$ dimension combination, α_{min} dives to ≈ 0.2. This value is well beyond the proposed range for α, stated in equation (4.21), where the minimal value in these condition is ≈ 0.61.
This situation can be interpreted as an overestimation of the under etched segment's displacement u^a_{ue}, as the α must dive for the evaluated F to stay close to the reference value. It could therefore be argued that the contribution of the under etched segment u^a_{ue} to the tensile force F should be neglected for certain combination of actuator and sample dimensions, for instance when the ratio actuator length over sample length is $\geq \frac{1500}{1.5}$.
Moreover, the curves seem to have a common intersection region at α values between $\approx [0.9, 1.0]$. Even though a thorough explanation of this phenomenon could not be uncovered here, this result seems to comfort the hypothesis that the real effective length of the under-etch region is closer to the $L_{ue,0}$ boundary of L_{ue}.

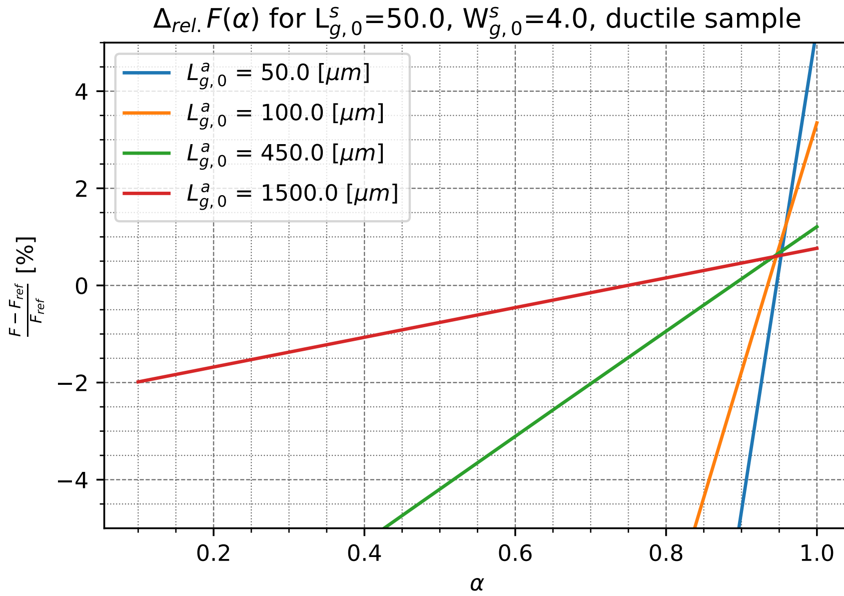

Figure 4.8: Evolution of the error made by the model of equation (4.21) as a function of the α parameter, for fixed sample size and varying actuator sizes. Case of a ductile sample.

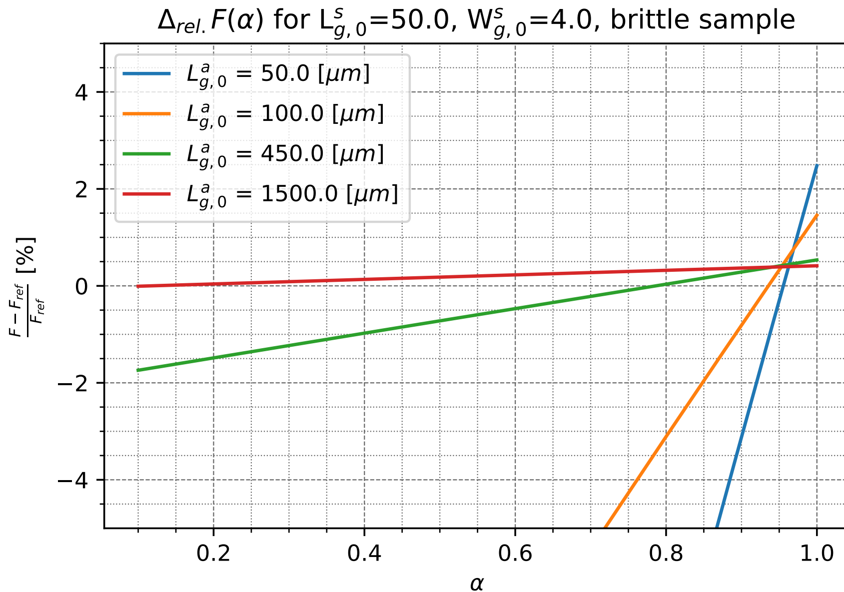

Figure 4.9: Evolution of the error made by the model of equation (4.21) as a function of the α parameter, for a fixed sample size and varying actuator sizes. Case of a brittle sample.

A model for $\alpha_{approx.}(L^s_{g,0}, W^s_{g,0}, L^a_{g,0})$

The values of $\alpha_{min,i}$ according to their respective geometries are listed on table B.1, in the appendices. The important range of the $\alpha_{min,i}$ value and the steepness of the error curves showed on figure 4.9 underlies the necessity of a good approximation of the α parameter to ensure an accurate data reduction. A poorly chosen α could lead to errors larger than the one that this correction model tries to suppress. However, the $\alpha_{min,i}$ parameters are only defined for a limited set of dimensions. It is crucial to extend the correction model to other sample and actuator geometries. One way to proceed to this extension is to find some sort of model for the α parameter that is a function of the sample and actuator's dimensions. This model, designated as α_{approx} would accurately fit the $\alpha_{min,i}$ for the reference dimensions and give an approximated value for any geometries in between.

A careful observation of the $\alpha_{min,i}$ tendencies in table B.1 and table B.2 suggests that there is a pattern behind the evolution of α_{min} and the structure geometry. Therefore, it could be possible to combine the variables and perform a mapping to reduce the number of variables. Such a mapping would make it easier to find an appropriate model for $\alpha_{approx.}(L^s_{g,0}, W^s_{g,0}, L^a_{g,0})$ by becoming the simpler function $\alpha_{approx.}(h)$.

$$\alpha_{approx}(L^s_{g,0}, W^s_{g,0}, L^a_{g,0}) \xrightarrow{h=f(L^s_{g,0},W^s_{g,0},L^a_{g,0})} \alpha_{approx}(h) \tag{4.34}$$

Where the new variable h is a function of the sample and actuator dimensions only. The choice of h required some intuitive feeling and a "fail and retry" approach. Moreover, a different mapping function h is required for the brittle and ductile material, as their $\alpha_{min,i}$ behaves differently. The chosen mapping function are listed on table 4.3 and plots of the $\alpha_{min,i}$ as a function of h are displayed on figure 4.10. and figure 4.11.

	Brittle material	Ductile material
Mapping function	$h = \frac{L_{g,0}W^s_{g,0}}{(L^a_{g,0})^2}$	$h = L^a_{g,0}$

Table 4.3: Mapping function h for $\alpha_{approx}(h)$, case of brittle and ductile samples

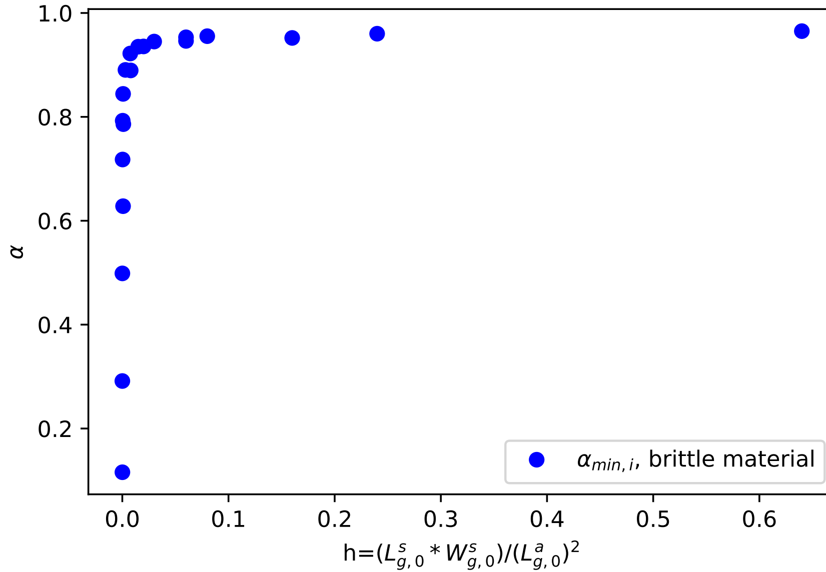

Figure 4.10: Evolution of the $\alpha_{min,i}$ parameters with the mapping h, case of a brittle material (ZnO)

The evolution of the $\alpha_{min,i}$ with h are consistent in both the brittle and ductile case. It is then possible to find a model for α_{approx} by curve-fitting the $\alpha_{min,i}$ points. This method is illustrated on figure 4.12 and figure 4.13 and the resulting curve-fitting models are listed on table 4.4.
In the case of the brittle material, the third regime for α_{approx} where $h < 10^{-4}$ is an unstable regime. As illustrated on figure 4.12, for the smallest values of h, the $\alpha_{min,i}$ are disordered. For $h < 10^{-4}$, the corresponding $\alpha_{min,i}$ values lie below the lower boundary of the range for which α has been described (equation (4.21)). This is an indication that both $h < 10^{-4}$ and $\alpha < \frac{L_{ue,eff}}{L_{ue,0}}$ are good indicators that the model becomes invalid. As stated earlier, α values $< \frac{L_{ue,eff}}{L_{ue,0}}$ are correlated with long actuators and a negligible contribution of the under etch segment to the tensile force.

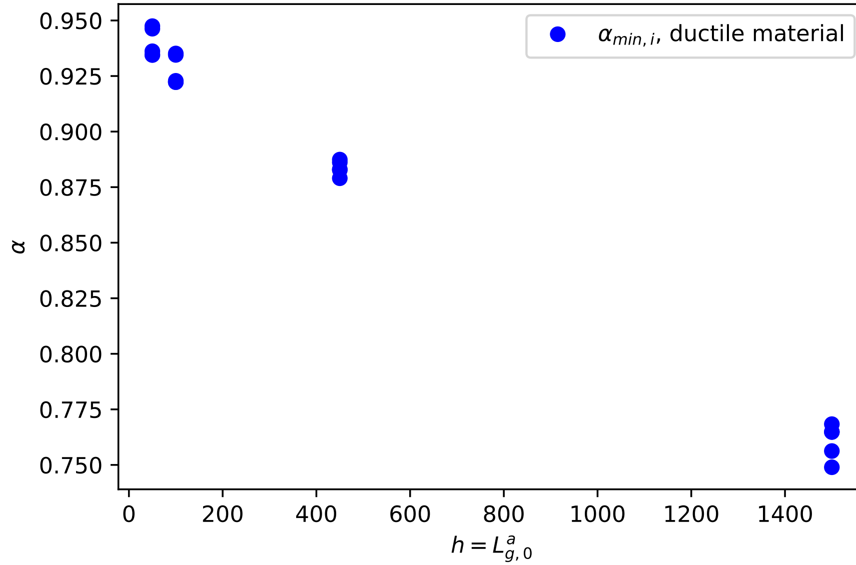

Figure 4.11: Evolution of the $\alpha_{min,i}$ parameters with the mapping h, case of a ductile material (Pd)

Brittle material	$\alpha_{approx} = \begin{cases} 0.950 & \text{if } h > 0.01 \\ \dfrac{0.885h}{(7.520 * 10^{-5}) + h} & \text{if } h \in [10^{-4}; 0.01] \\ \dfrac{0.940h}{(1.250 * 10^{-4}) + h} & \text{if } h < 10^{-4} \quad \text{(Unstable!)} \end{cases}$	$h = \dfrac{L^s_{g,0} W^s_{g,0}}{(L^a_{g,0})^2}$
Ductile material	$\alpha_{approx} = 0.942 - (1,213e * 10^{-4})h$	$h = L^a_{g,0}$

Table 4.4: Models of $\alpha_{approx}(h)$

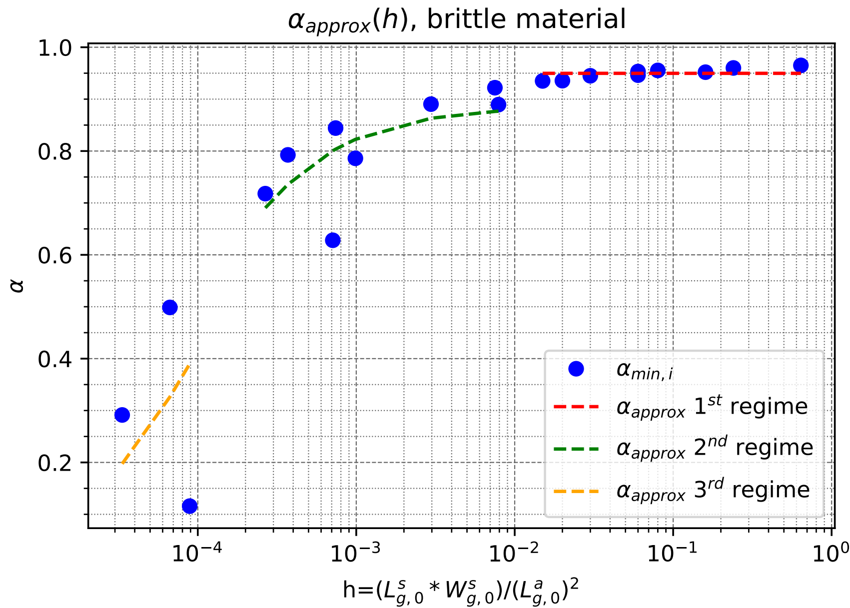

Figure 4.12: Logarithmic plot of $\alpha_{approx}(h)$. 3 curve-fitting regimes corresponding to specific h values are highlighted. Case of a brittle material (ZnO)

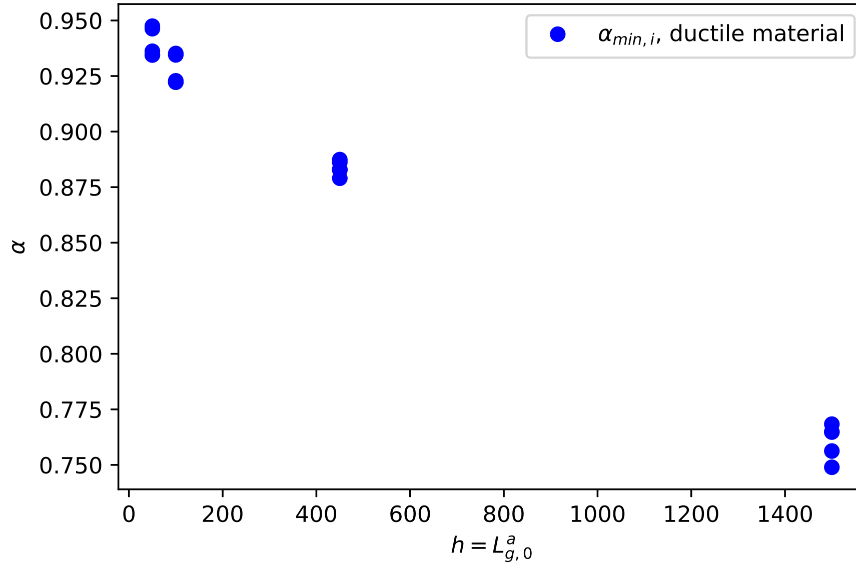

Figure 4.13: Curve fitting model (linear regression) of $\alpha_{approx}(h)$, case of a ductile material (Pd).

4.3.3 Optimisation and modelling of the β parameter

As for the α parameter, the goal here is to develop an approximate model of the β parameter, valid for a broad range of sample and actuator geometries. The treatment applied to the β parameter is similar to the one described earlier for α: **i)** study the evolution of the displacement u_{ue} *vs.* β, **ii)** identify the $\beta_{min,i}$ and their behaviour, **iii)** suggest an appropriate mapping for the structure dimensions and **iv)** find a model for β_{approx} using curve-fitting.

Displacement of the under-etched region and β

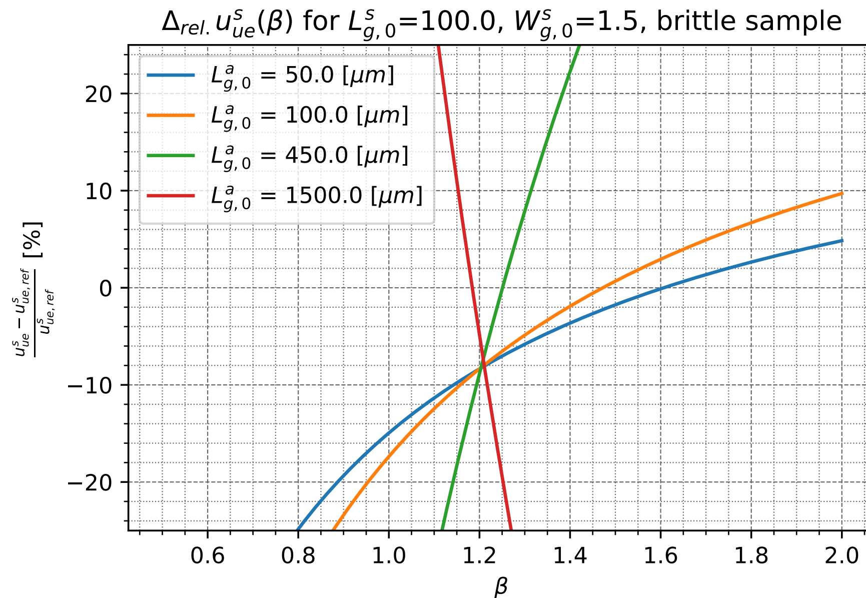

Figure 4.14: Evolution of the error made by the model of equation (4.26) as a function of the parameter β, for fixed sample size and varying actuator size, case of a brittle sample (ZnO)

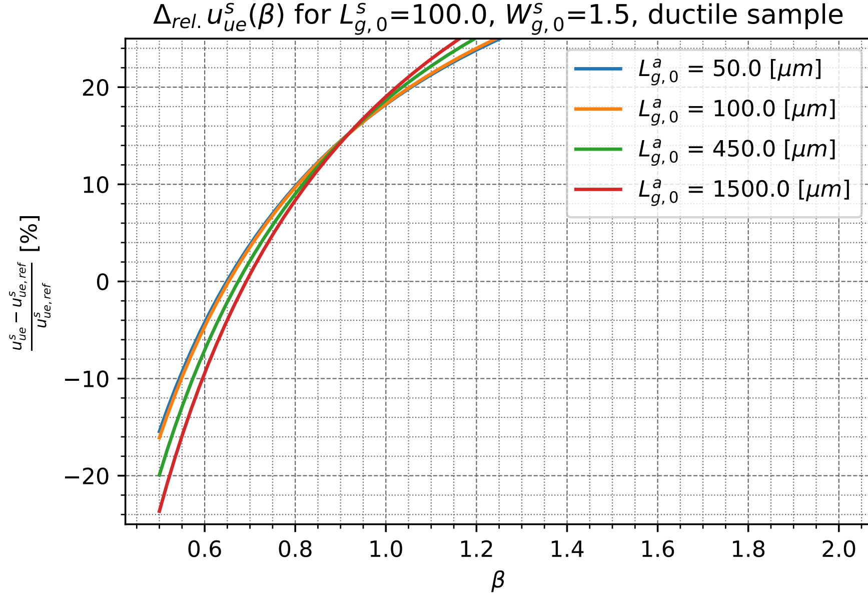

Figure 4.15: Evolution of the error made by the model of equation (4.26) as a function of the parameter β,for fixed sample size and varying actuator size, case of a ductile sample (Pd)

Figure 4.14 and figure 4.15 show the evolution of the error between the calculated displacement u^s_{ue} and the reference data with the β parameter. The values of the β parameter that minimise the error made by the model are denoted by $\beta_{min,i}$ and are listed on table B.1 and table B.2. The behaviour of the error is less tame than the error linked with the α parameter. Indeed, a small change of β leads to a large error on the displacement u^s_{ue}. Moreover, for a brittle sample with a length $L^s_{g,0}$= $100[\mu m]$ or shorter, the error switches from increasing with β to decreasing with β, when the actuator length reaches $1500[\mu m]$. This is explained by the mechanical behaviour of the under etched part. The mismatch strain in this part stays larger than the tensile strain applied by the actuator until the tensile stress reaches a pivot point. At this pivot point, the under etched part switches from a contraction state (negative displacement) to a dilatation state (positive displacement) in the (1) direction. This feature can lead to an almost vertical curve around the β_{min} value, because the relative error is defined as $\frac{u^s_{ue}-u^s_{ue,ref}}{u^s_{ue,ref}}$ and $u^s_{ue,ref}$ reaches 0 at the pivot point.

In the case of the ductile sample, the $\beta_{min,i}$ values that minimise the error on u^s_{ue} are outside the range of accepted β values, below the lower bound. In equation (4.26), a β value smaller than the lower bound means that u^s_{ue} is being underestimated by the correction model. Indeed, as u^s_{ue} is being underestimated, the β parameters takes a value lower than the lower boundary, $\beta = 1$ to stay true to the reference data. 2 hypotheses stem from this observation:

1. The onset of plasticity is reached in the under-etched segment on the sample side, causing larger displacements than expected.

2. The contribution of the mismatch strain is underestimated.

The last hypothesis has to be rejected because the mismatch strain is multiplied by $L_{ue,0}$, which is the upper bound of L_{ue}, leading to a slight overestimation of the mismatch strain's contribution. It is then possible that the onset of plasticity is reached in the under etched segment in these conditions. This can be verified thanks to the implementation of the model and the von Mises criterion. As stated in hypothesis 5, the under etched segment on the sample side is in a state of biaxial plane stress. The

stresses can be computed in the implementation of the model, using the following expressions:

$$\sigma_{ue}^{s,(1)} = \frac{F}{A_{ue,eff}^{s}} \tag{4.35}$$

$$\sigma_{ue}^{s,(1)} = \nu^{s}\sigma_{ue}^{s,(1)} - E^{s}\varepsilon_{mis}^{s} \tag{4.36}$$

$$\sigma_{VM} = \sqrt{\frac{1}{2}[(\sigma_{ue}^{s,(1)} - (\sigma_{ue}^{s,(1)}))^2 + (\sigma_{ue}^{s,(2)})^2 + (\sigma_{ue}^{s,(1)})^2]} \tag{4.37}$$

The von Mises stresses in this situation are ranging between 340 and $500[MPa]$ If the yield stress σ_0^{Pd} is taken at $390[MPa]$ (not a random value, see discussion in section 4.5.1), then the onset of plasticity is not reached in every case. This conclusion excludes the first hypothesis as well. The only explanation to the behaviour of the β parameter when ductile sample are modelled is that hypothesis 5 is invalid for ductile sample. Consequently, either the under-etched part can't be described by a rectangular shape, or the strain in its horizontal direction is not null, or maybe both. To go further and answer this question, another finite element simulation more focused on the under-etched region could be carried out. Anyway, while being out of his theoretical range, the β parameter still has stable values. Thus it is still possible to accurately predict its behaviour, as done afterwards.

Finally, as a last comment, it seems that the $u_{ue}^{s}(\beta)$ curves also have a common intersection region. However, unlike α, this intersection region shifts between $\beta \approx 1.1 - 1.2$ for brittle samples and $\beta \approx 0.9 - 0.95$ for ductile samples and the region is a well defined point. This behaviour could not be explained in this study.

A model for $\beta_{approx}(L_{g,0}^{s}, W_{g,0}^{s}, L_{g,0}^{a})$

The method to find a model for an approximated β parameter is identical to the one described for α_{approx}. Again, the objective is to find a β_{approx} parameter that is continuous for any value of a variable h which itself is a mapping such as $h = f(L_{g,0}^{s}, W_{g,0}^{s}, L_{g,0}^{a})$. The appropriate mapping functions were found by inspection of the $\beta_{min,i}$ tendencies and a "fail-and-retry" approach. The resulting mapping function $h(L_{g,0}^{s}, W_{g,0}^{s}, L_{g,0}^{a})$ are listed on table 4.5.

	Brittle material	Ductile material
Mapping function	$h = \frac{L_{g,0}^{s}}{L_{g,0}^{a}} e^{-W_{g,0}^{s}}$	$h = \frac{L_{g,0}^{s}}{L_{g,0}^{a}} e^{-W_{g,0}^{s}}$

Table 4.5: Mapping function h for $\beta_{approx}(h)$, case of brittle and ductile samples

By plotting the $\beta_{min,i}$ values vs. h, one can find an approximate model for $\beta_{approx}(h)$ using curve fitting. The graphical results of this method are displayed on figure 4.16 and figure 4.17. These plots highlight a limitation of the "mapping-curve fit" approach. There seem to be 2 distinct tendencies in the $\beta_{min,i}$ vs h curves, this is especially visible for the ductile Pd data. Further inspection revealed that these 2 distinct tendencies stem from the width of the sample $W_{g,0}^{s}$. The effect of $W_{g,0}^{s}$ on the $\beta_{min,i}$ values is not linear. Thus, with only two different widths $W_{g,0}^{s} = [1.5 - 4\mu m]$ available as reference data, the "mapping-curve fit" approach suffers from a loss of accuracy. The loss in accuracy leads to errors on the sample displacement u_g up to 6%, in the worst case (see the penultimate column of table B.1). A reference data set with more variation of the sample width would allow to find a better link between the $\beta_{min,i}$ values and the structure dimensions and therefore a more precise model for $\beta_{approx}(h)$. In the mean time, the suggested models for β_{approx} are listed on table 4.6.

Brittle material	$\beta_{approx}(h) = 1.503 - 0.404e^{-8.026h}$	$h = \frac{L^s_{g,0}}{L^a_{g,0}} e^{-W^s_{g,0}}$
Ductile material	$\beta_{approx}(h) = 0.623 + 0.404e^{-5,17h}$	$h = \frac{L^s_{g,0}}{L^a_{g,0}} e^{-W^s_{g,0}}$

Table 4.6: Models of $\beta_{approx}(h)$

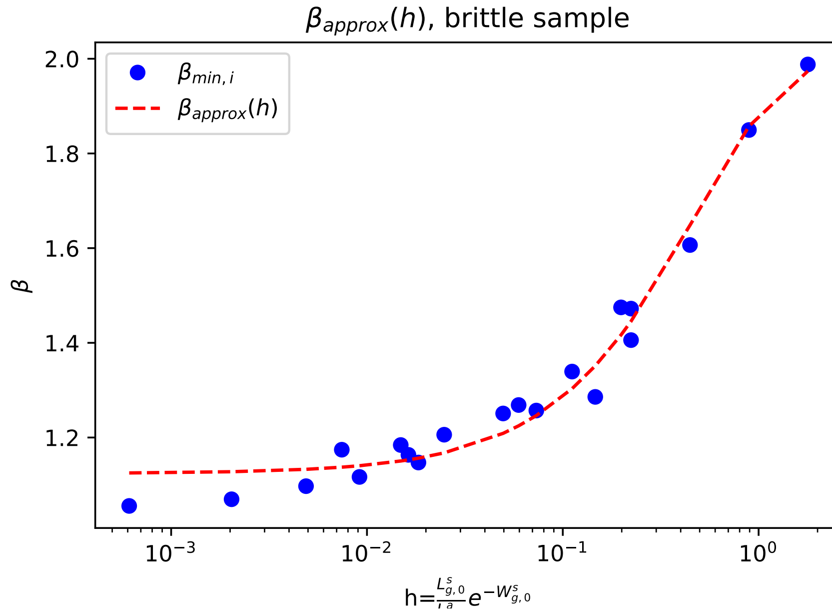

Figure 4.16: Curve fitting model of $\beta_{approx}(h)$, case of a brittle material (ZnO).

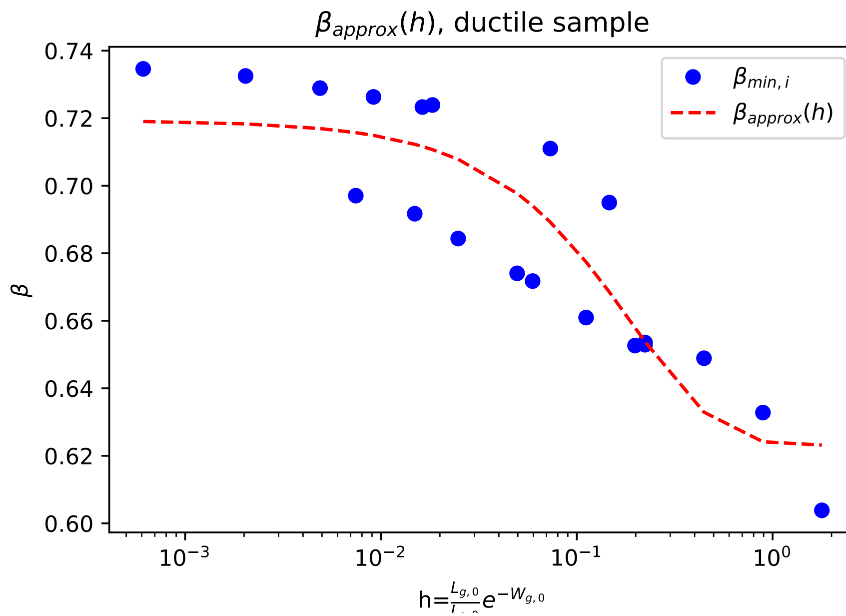

Figure 4.17: Curve fitting model of $\beta_{approx}(h)$, case of a ductile material (Pd).

4.4 Final correction model and data reduction scheme

With the hypotheses introduced in the development of the correction model, the actuator-sample system is now described by a set of 7 individual segments all uniquely contributing to the displacement of the structure. This system is illustrated on figure 4.18 and its mechanical behaviour is described by the following equations:

$$\begin{cases} F = -E^a \left(\dfrac{u + \varepsilon^a_{mis}(L^a_{g,0} + \alpha_{approx} L_{ue,0}(1+\nu^a))}{\frac{L^a_{g,0}}{A^a_{g,eff}} + \frac{\alpha_{approx} L_{ue,0}(1-(\nu^a)^2)}{W^a_{max} t^a_g}} \right) \\ u_g = u - 2R_{db} \left(\dfrac{1}{E^s} \dfrac{F}{t^s W_{db,eff}} - \varepsilon^s_{mis.} \right) - L_{db,3} \left(\dfrac{1}{E^s} \dfrac{F}{t^s W_{db}} + \varepsilon^s_{mis.} \right) - ... \\ \qquad ... - L_{ue,0} \left(\dfrac{1-(\nu^s)^2}{E^s} \dfrac{F}{t^s_{g,0} W_{db} \beta_{approx}} + \varepsilon^s_{mis.}(1+\nu^s) \right) \\ \varepsilon^{mech}_g = ln \left(\dfrac{L^s_{g,0} - u_g}{L^s_{g,0}} \right) - \varepsilon^s_{mis} \\ \sigma_g = \dfrac{F}{W^s_{g,0} t^s_{g,0} (1 + \varepsilon^s_{mis} - \nu^s \varepsilon^{mech}_g)(1 - \nu^s \varepsilon^{mech}_g)} \\ E^s = \dfrac{\sigma_g}{\varepsilon^{mech}_g} = \dfrac{F}{W^s_{g,0} t^s_{g,0} (1 + \varepsilon^s_{mis} - \nu^s \frac{u_g}{L^s_{g,0}})(1 - \nu^s \frac{u_g}{L^s_{g,0}})(\frac{u_g}{L^s_{g,0}} - \varepsilon^s_{mis})} \end{cases}$$

Where α_{approx} and β_{approx} are given by:

Brittle samples:

$$\alpha_{approx} = \begin{cases} 0.950 & \text{if } h > 0.01 \\ \dfrac{0.885h}{(7.520 * 10^{-5}) + h} & \text{if } h \in [10^{-4}; 0.01] \\ \dfrac{0.940h}{(1.250 * 10^{-4}) + h} & \text{if } h < 10^{-4} \quad \text{(Unstable!)} \end{cases} \qquad h = \frac{L^s_{g,0} W^s_{g,0}}{(L^a_{g,0})^2}$$

$$\beta_{approx}(h) = 1.503 - 0.404e^{-8.026h} \qquad h = \frac{L^s_{g,0}}{L^a_{g,0}} e^{-W^s_{g,0}}$$

Ductile samples:

$$\alpha_{approx} = 0.942 - (1,213e * 10^{-4})h \qquad h = L^a_{g,0}$$

$$\beta_{approx}(h) = 0.623 + 0.404e^{-5,17h} \qquad h = \frac{L^s_{g,0}}{L^a_{g,0}} e^{-W^s_{g,0}}$$

The data reduction scheme uses this model to correct incoming experimental. The data reduction scheme applies this model to incoming experimental data and returns both a stress-strain graph as well as the corrected data as lists of value. The data reduction scheme has been developed as a Python script, which uses an Excel file containing the input data and produces both a graph and an Excel file containing the corrected data.

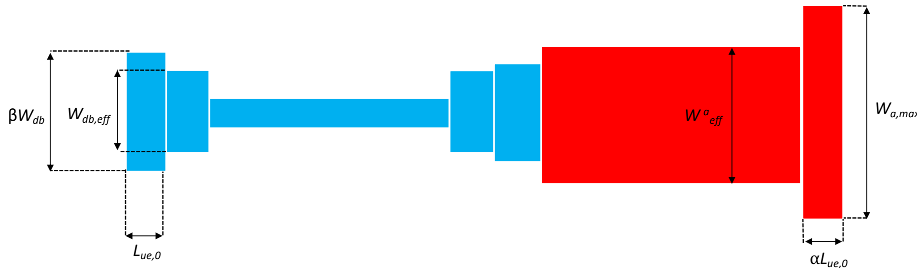

Figure 4.18: Simplification of the device's structure used as a basis for the correction model, with some important dimensions highlighted.

4.5 Results and sicussion

4.5.1 Application on reference data

The final correction model is first applied on the reference data. This allows to see how well the model performs against non-corrected and reference data. In non-corrected data, stresses and strain are computed with u instead of u_g, therefore no correction is applied on these points. also brings a quantitative analysis of the precision gained when the correction model is applied in the data reduction scheme. It should be kept in mind that this should be the best case scenario for the correction model, as the α_{approx} and β_{approx} parameters were tuned using the reference data.

Figure 4.19 shows the resulting stress-strain curve obtained when the the correction model is applied on results from brittle samples. As the sample is brittle, only an elastic regime appears on the graph. Therefore, the sample's Young's modulus E_s has been plotted along the data points, through linear regression. The error on E_s between the non-corrected and reference data sets is around 7.76%. Meanwhile, the error on E_s between the corrected and reference data sets is only around 2.97%. The E_s approximated using the displacement correction inside the data reduction scheme is therefore $\approx 2.6\times$ more precise.

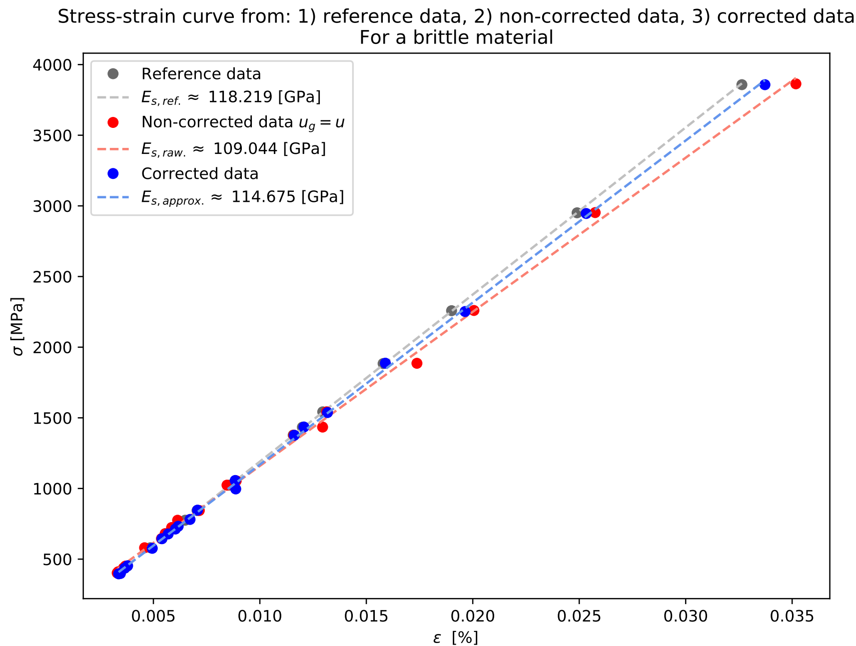

Figure 4.19: Stress-strain curve for brittle ZnO samples, data simulated from FE simulations. The grey data is the reference data, computed by finite element methods on the Abaqus software. The red data corresponds to the application of the scheme with the displacement correction. The blue data corresponds to the application of the scheme without the displacement correction.

The stress-strain curve associated with the ductile reference data is presented on figure 4.20. This time, as a plastic regime is present, the Young's modulus has not been calculated (not enough points in the linear regime). Instead, the strain hardening coefficient is roughly calculated by curve fitting a Swift law onto the data in the plastic regime. The transition between plastic and elastic regime occurs when the stress becomes larger than the yield stress σ_0. As the reference data is based on a simulation for a Pd sample, a yield stress value valid at the microscopic scale choice has been chosen: $\sigma_0 = 390[MPa]$ [52].

The effect of the correction model on this data set is not as remarkable as in the previous case. The

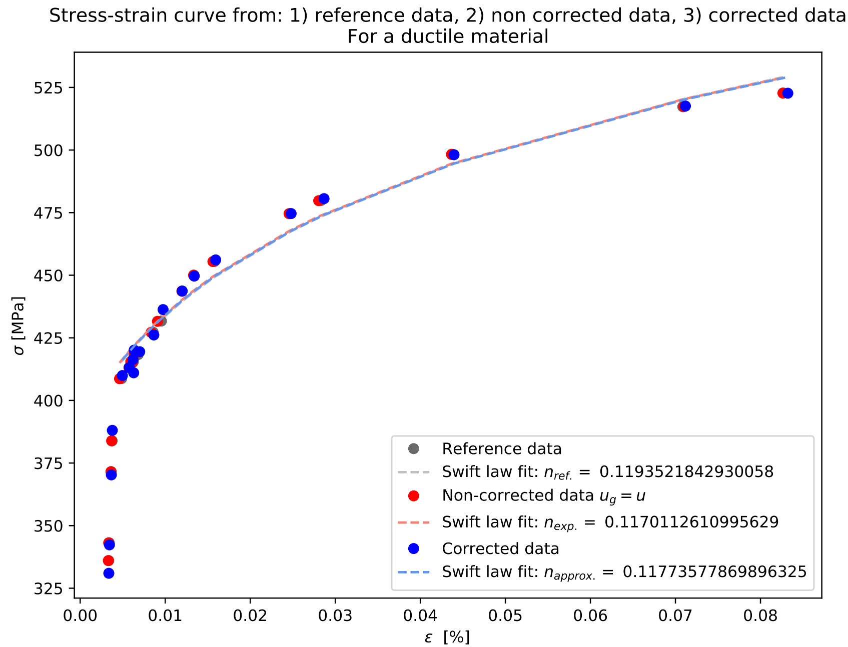

Figure 4.20: Stress-strain curve for ductile Pd samples, data simulated from FE simulations. The grey data is the reference data, computed by finite element methods on the Abaqus software. The red data corresponds to the application of the scheme with the displacement correction. The blue data corresponds to the application of the scheme without the displacement correction.

gain in precision is not apparent on the graph, mainly due to the scale used as well as the overlapping coloured markers. The stress-strain curve obtained with the non-corrected data is already close to the reference data. The addition of the correction model only brings an insignificant gain in precision. No conclusions about the contribution of the correction model can be made in this case. Fortunately, experimental data on ductile samples (Al) have been also been treated with the correction model. These results are more conclusive and can be found in section section 4.5.3.

Furthermore, the Swift law fits the data poorly. This might be narrowed down to the choice of σ_0 and the lack of points around the chosen σ_0 value. The σ_0 has been chosen from the lower bound of experimentally measured values in [52]. This lower bound seemed to be the closest σ_0 to the one observed in the reference data set: $\sigma_0^{Pd} = 390[MPa]$. A more precise choice of σ_0 could be made, however the Swift law fit and strain hardening coefficient are only displayed for "show", not for a careful data analysis on the material. All in all, the choice of the σ_0 value is imprecise. Moreover, the points in the plastic regime just above the yield stress are crucial to fully describe the plastic regime. Their absence, combined with the approximative yield stress value, is likely a cause of the poor fit of the Swift law on the data.

Limitations of the correction model

While the results of the application of the correction model on the reference data are encouraging, some limitations need to be highlighted.

First and foremost, the correction model is intrinsically limited by the variety of the data provided in the reference data set. Indeed, the model behind the optimisation of α_{approx} and β_{approx} was extracted from the reference data set, where the contribution of certain parameters couldn't be evaluated (thickness of the sample) or are poorly evaluated (width of the sample). A more diverse reference data set would be a important step forward to create a more polyvalent and reliable correction model.
Moreover, the model behind the $\alpha_{approx.}$ parameter has been shown to become unstable for brittle

samples with specific actuator and sample dimensions. These specific dimensions are described by $h = \frac{L^s_{g,0} W^s_{g,0}}{(L^a_{g,0})^2} < 10^{-4}$. Again, as the reference data offered no variation of the sample's thickness and only two different sample width, their contribution can't be properly evaluated on $\alpha_{approx.}(h)$. Hence, there is a risk for some unstable data to "fly under the radar" because they are not properly described by the condition $h = \frac{L^s_{g,0} W^s_{g,0}}{(L^a_{g,0})^2} < 10^{-4}$.

In a second time, the remaining variations between the corrected and reference data can't be entirely explained by the previously mentioned limitation in reference data. Other contributing factors must be brought to light. One hypothesis is that the displacement u_g is not properly described by equation (4.30). Indeed, careful analysis of the data in table B.1 and table B.2 underlies a certain level of error in the evaluated sample displacement u_g. Consequently, a rigorous inspection of the strain[2] inside the different parts of the structure has been conducted. The goal pursued by this investigation is to observe how reliably does the model evaluates strain in the different elements of the structure, the dog bones, the overlap regions, ... As a reminder, the β and α parameters are designed to optimize the accuracy of the model to describe the displacements of the under-etched segments, u^s_{ue} and u^a_{ue}. However, this is not the case for the other elements, namely the dog bones and the overlap region. Thus, one could expected the strain in the two under etched segments to be well approximated, while the other elements could show a more exotic evaluation. In order to shed light on those assumptions, the strain in the different parts of the lab-on-chip are represented and compared to the reference data on figure 4.21 and figure 4.22, for brittle and ductile samples respectively.

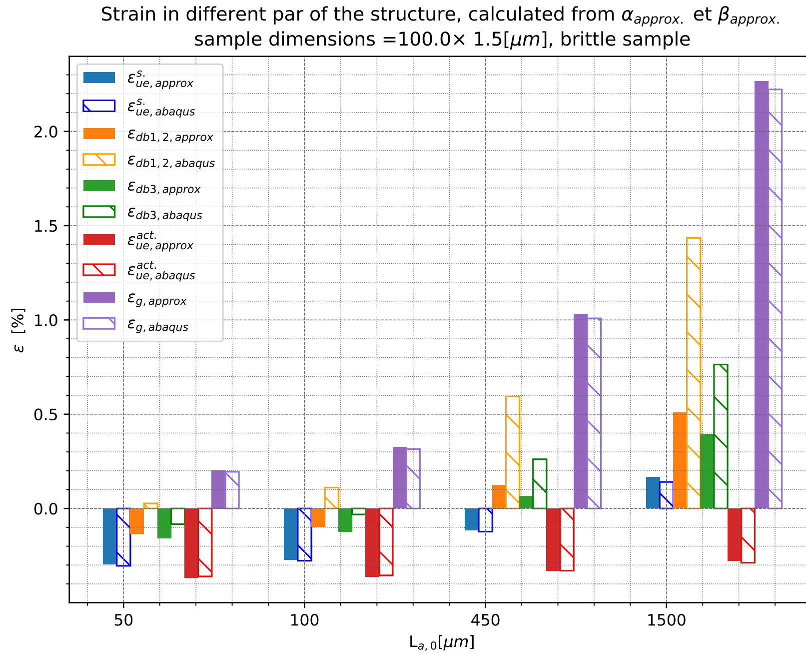

Figure 4.21: Strain in different regions of the lab-on-chip device, represented as a bar plot. Plain bars indicates the result of the correction model while the hatched bar represent the reference data, case of a brittle sample

As expected, figure 4.21 and figure 4.22 suggest that that in either brittle or ductile case, the evaluated strain in the two under-etched segments is accurate with respect to the reference data, while the strain in the dog bone and overlap region are poorly evaluated. This observation is consistent throughout the entire range of actuator lengths and sample dimensions (as showcased in figure 4.24, where the results of another set of actuator and sample dimensions is showcased). Three plausible explanations of this behaviour are considered.

[2]Strain is inspected, rather than displacements, because the dimensions such as $R_{db,0}, L_{db3,0}$ used to jump from strains to displacement are supposedly precise and constants.

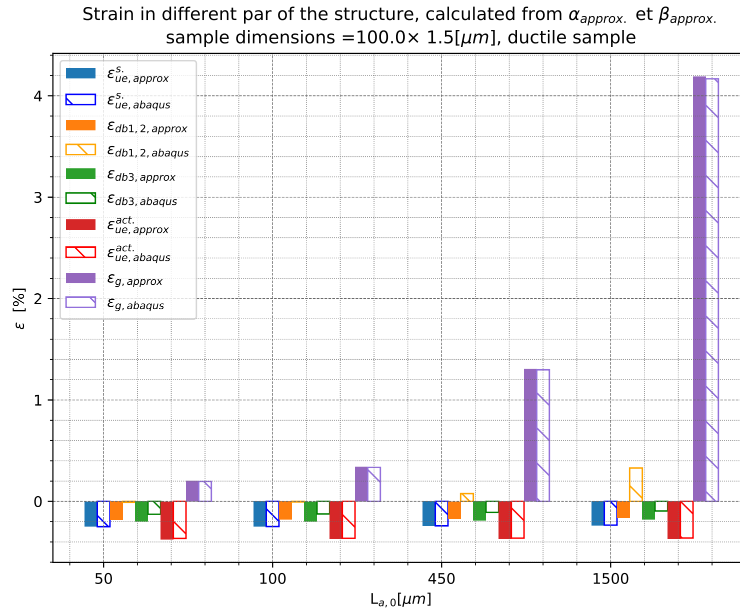

Figure 4.22: Strain in different regions of the lab-on-chip device, represented as a bar plot. Plain bars indicates the result of the correction model while the hatched bar represent the reference data, case of a ductile sample

1. Hypothesis 4 made in the development of the correction model is not always valid for the dog bone regions. The stress inside the dog bone might not be uniaxial, therefore the strain would be wrongly evaluated and the onset of plasticity could be reached in the dog bone before it is reached in the sample. This hypothesis is supported for the dog bone attached to the under-etched segment. Indeed, the under etched segment is considered to be in a biaxial plane stress configuration, therefore some shear stress should appear in the side of the dog bone that is connected to the under-etched segment, the resulting supposed stress state is represented on figure 4.23. However, the stress state for such a situation could not be described here. If the stress state could be evaluated, the von Mises equivalent stress could be computed and it would be possible to verify whether the dog bone behaves plastically. In the meantime, this assumption can't be properly verified.

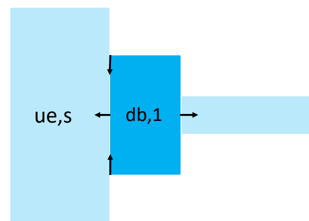

Figure 4.23: Supposed stress state in the dog bone connected to the under-etched frame. The stress is assumed to be compressive because of the effect of the mismatch strain in the under-etched segment.

2. The reference data itself is skewed. This doesn't mean that all the reference data is compromised, but rather that due to concerns over boundary conditions between different regions in the FE simulations, strains of the individual elements can't be dissociated from the total strain as it was performed in this study.

3. For the overlap region only, the model of the overlap region is intrinsically wrong as the real overlap region is made from an *overlap* of both the sample and a layer of actuator material. This "layered" aspect can be observed schematically in figure 3.3. However, the correction model

ignores the top layer of actuator material and its contribution to the strain in the overlap segment. The model could be enhanced by taking this bi-layer structure into account.

On the other hand, it can also be observed that the errors made on the strain in the dog bone and overlap region do not contribute a lot to the strain in the sample ε_g. Indeed, the error between the plain bar in purple, corresponding to ε_g, and the reference is much smaller than the errors made on the dog bones and overlap regions. This is mainly due to the fact that the dog bone and overlap region are the smallest elements of the structure and therefore contribute less to the overall strain in the structure.
Moreover, the plots highlights that the strain in certain elements in sometimes negative. In those cases, the mismatch strain is larger than the tensile strain exerted by the actuator.

Finally, the observations made on the behaviour of the α and β parameters in section 4.3.2 and section 4.3.2 still hold true. To sum up these discussions, it has been shown that:

- In the case of brittle samples, the $\alpha_{min,i}$ values of α dive to values well below their theoretical range when the ratio $\frac{L^a_{g,0}}{L^s_{g,0}} \geq 1000$. This could be due to an overestimation of the under-etched segment's contribution on the tensile force, leading to an overcompensation through the α parameter, causing it to dive below the lower boundary (≈ 0.61). One solution would be to dismiss this contribution for extreme $\frac{L^a_{g,0}}{L^s_{g,0}}$ values.

- For ductile samples, the $\beta_{min,i}$ values are consistently below the minimal value of their theoretical range. This case has been studied and some hypotheses were excluded thanks to careful analysis of the situation. The only explanation left to explain this bizarre behaviour is that hypothesis 5 of the correction model is invalid for ductile samples. It was also noted that, while unsettling, this observation doesn't jeopardise the capacity of the correction model, as the $\beta_{min,i}$ values can still be accurately predicted.

- One stone has been left unturned: the unexplained intersection area between the $F(\alpha)$ curves and the $u^s_{ue}(\beta)$ curves. No leads were found to start this investigation.

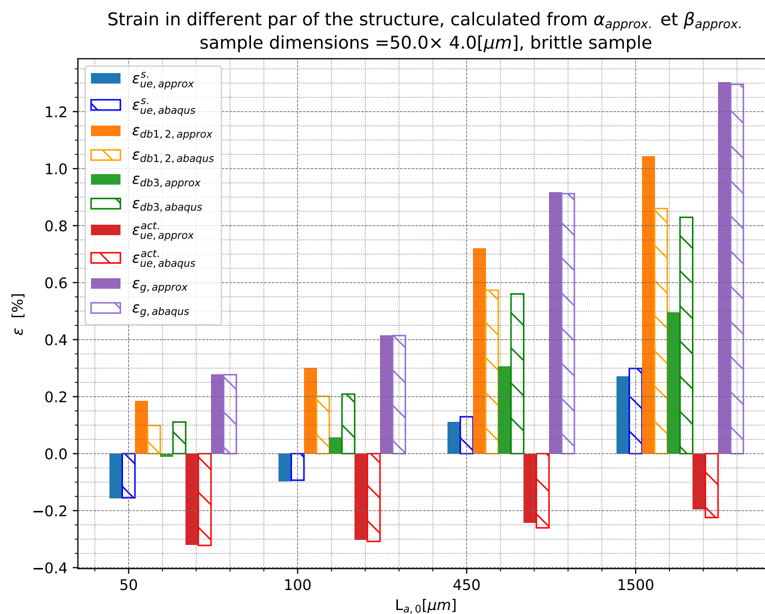

Figure 4.24: Graph equivalent to figure 4.21 but for different sample dimensions

4.5.2 Practical example: ZnO samples

The application of the correction model on the experimental data for ZnO sample further comforts the claims made previously for brittle samples. The correction model seems to work as expected: points corresponding to different data sets (ie: different sample or actuator geometries) are less further apart when the correction model is applied. This phenomenon is visible on figure 4.25. The stresses are also consistently higher when corrected. This could mean that non-coorected stresses are underestimated, which is in agreement with an observation made by *Lemoine et Al.*, in an unpublished work. Moreover, the Young's modulus E^s has been calculated for both the corrected and uncorrected data. The corrected E^s is closer to the reference value for ZnO microwires: $E^{ZnO} \approx 100[GPa]$[53]. If we choose $E^{ZnO} \approx 100[GPa]$ as a reference, the relative error between the non corrected E^s and the reference is around 27.8% while it goes down to 9.7% for the corrected data.

On a side note, the graphs obtained from now on have been obtained with the final data reduction scheme tool. This tool applies the correction model on input data and computes the stresses and strains, which are plotted and returned as values in an Excel file.

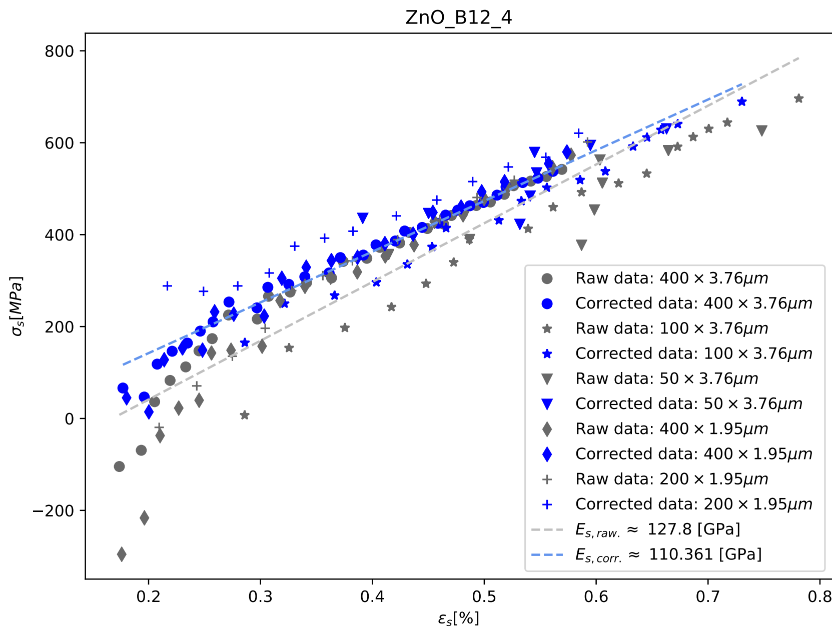

Figure 4.25: Stress-strain curve for ZnO samples with various geometries, experimental data from R. Tuyaerts.

4.5.3 Practical example: Al samples

The application of the correction model on measurements made on Al samples yields interesting results. Aluminium is a ductile material and was deposited on the on-chip tensile testing device by sputtering. This case begins with a set of compromised experimental results. Indeed, the mismatch strain of the actuator $\varepsilon^a_{mis.}$ was measured with a lot of uncertainty: $\varepsilon^a_{mis.,0} \approx -0.003$. This case is a good sandbox to assess the contribution of $\varepsilon^a_{mis.}$ on the correction model.

Without the correction model developed here, the stress-strain curve was inconsistent and a correction was applied by slightly increasing the value of $\varepsilon^a_{mis.}$. This correction made the stress-strain curve more consistent, but the $\varepsilon^a_{mis.}$ value had to be altered and was overestimated: $\varepsilon^a_{mis.} = -0.0034$.

When the correction model was applied, inconsistent behaviour was still observed with the unaltered $\varepsilon^a_{mis.}$. This time however, a much smaller correction on the mismatch was necessary to get a consistent curve: $\varepsilon^a_{mis.} = -0.0032$. The resulting graph is shown on figure 4.27, while the graph illustrating the case where $\varepsilon^a_{mis.}$ is left unchanged is shown on figure 4.26. With the overestimated mismatch strain $\varepsilon^a_{mis.} = -0.0034$, the stress-strain curve became inconstant again.

These observations highlights the stress's sensibility to the actuator's mismatch strain. Both the non-corrected data and the data treated by the correction model saw a twofold increase in their stresses value when the $\varepsilon^a_{mis.}$ was raised from -0.003 to -0.0034. This can lead to critical overestimation of the yield strength or the ultimate strength of the studied material. Thus, in order for the model to do a good work, it needs a precise value of $\varepsilon^a_{mis.}$, otherwise the results will be skewed.

Moreover, the fact that a lesser correction on the $\varepsilon^a_{mis.}$ is needed when the correction model is applied implies that the model already does a good job of correcting the data. The contribution of the correction model is especially visible when $\varepsilon^a_{mis.}$ is left unchanged, represented on figure 4.26. Again, the data points are less spread apart when the correction is applied.

In sum, the benefits of the correction model for ductile samples are not as evident than for brittle sample, as the measurements from the experiments made on these Al samples were imprecise to start with. Nonetheless, it appears that the correction model still limits the spreading out of the stress-strain points, which is still a good indication of the proper functioning of the correction model.

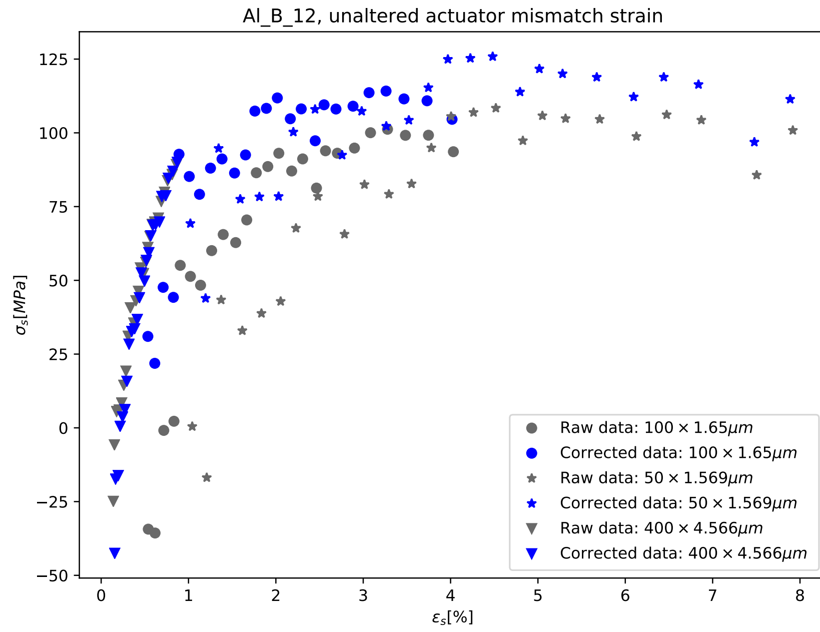

Figure 4.26: Stress-strain curve for Al samples with width, experimental data from H. Wang. Case of unaltered $\varepsilon^{a}_{mis.}$.

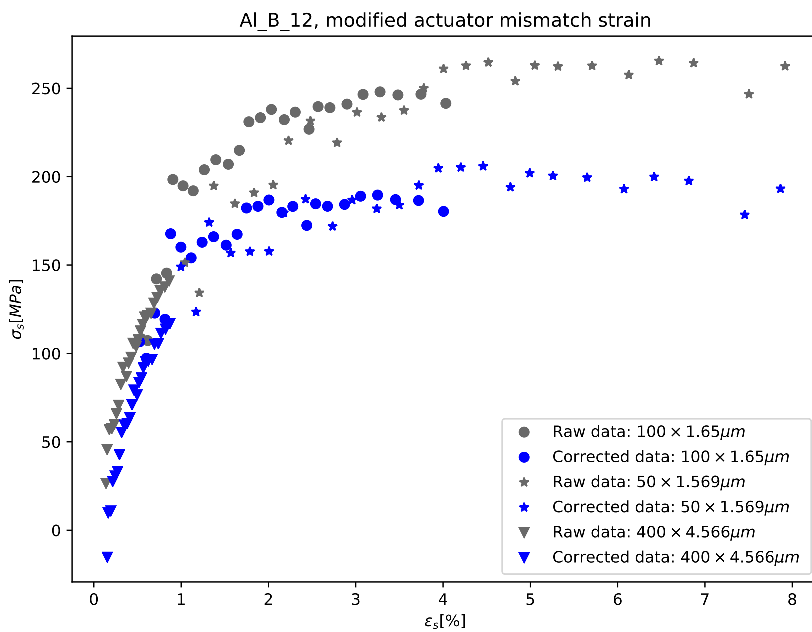

Figure 4.27: Stress-strain curve for Al samples with width, experimental data from H. Wang. Case of modified $\varepsilon^{a}_{mis.}$. For the raw data, $\varepsilon^{a}_{mis.} = -0.0034$, for the corrected data, $\varepsilon^{a}_{mis.} = -0.0032$.

4.5.4 Practical example: Al_2O_3 samples

An older set of experimental data on Al_2O_3 samples has also been treated with the correction model. Here, a lot of approximations were made in order to be able to treat the data with the new data reduction scheme. The results are shown on figure 4.28.

The corrected results are slightly less spread out than the non-corrected one, which is still a good

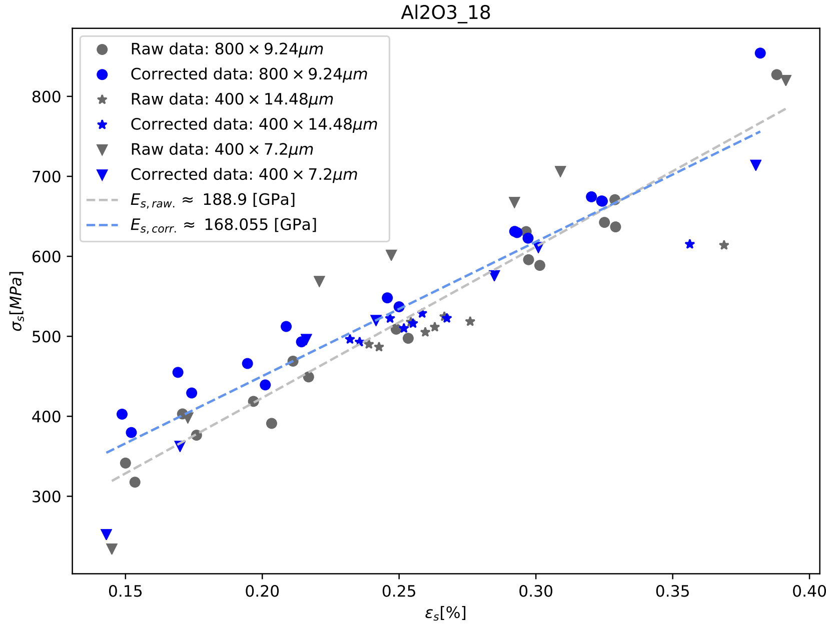

Figure 4.28: Stress-strain curve for Al_2O_3samples.

indicator of the proper functioning of the correction model. However, in this case, the benefits of using the correction model are weighted down by the approximations made on the input data:

- The latest implementation of the data reduction scheme requires the width of the actuator to be constant. In the input data of the Al_2O_3, the actuator width where spread between 18.29 and 18.02 $[\mu m]$, requiring them to be approximated at a mean value of 18.2$[\mu m]$.
- The under-etch was approximated to be 10$[\mu m]$ long. The sensitivity of the correction to the under-etch length has been tested. It was found that a 25% increase in $L_{ue,0}$ resulted in a $\approx$ 3% decrease in the approximated Young's modulus.
- The geometry of the dog bone was unknown and were considered to be equivalent to the reference data, a circular dog bone described by a R_{db} of 2$[\mu m]$. Other dog bone geometries were tried but only slightly affected the results: $< 1\%$ variation between R_{db} ranging from 1 to 5$[\mu m]$.

This case highlights some guidelines to respect in order to ensure a proper functioning of the new data reduction model. The actuator width should be controlled in order to be as constant possible. Otherwise, a mix of different actuator widths should be avoided, even if it means that some measurements should be discarded. Moreover, the under-etch's length $L_{ue,0}$ should be should be known with accuracy, whether it comes from direct measurements or approximations considering the etching rate. These guidelines are complementary with other observations made on the Al and ZnO samples, they are summed up in the conclusion of this work (chapter 6).

Chapter 5

Sustainability assessment of opto-electronic devices fabrication

This chapter takes a step back from the material science point of view of strained light emitting devices. Here, another aspect surrounding integrated light emitting devices is considered: an assessment of the **sustainability** surrounding the fabrication of such devices.
Taking a step back like this is key to keep a critical mindset towards the technology that has been presented throughout the master thesis. Nowadays, studying and judging a technology only on its performance for a specific task is outdated. A critical look towards the insertion of this technology on the market and its sustainability is crucial.

The main focus of this master thesis revolves around integrated light emitting devices ans their strain engineering. The fabrication and application of such devices have been described in chapter 2.4, but only for silicon and germanium based devices built in research environments.

As this chapter takes a step back from the previous ones, the framework gets broader. From a material point of view, this means that the sustainability discussion will not be limited to strained Si and Ge-based devices. The discussion will also take into account devices made from different, unstrained, materials. Indeed, alongside Si and Ge, III-V materials are also heavily used for their opto-electronic properties, especially as light emitters. In this work, III-V materials are represented by GaAs which has been a spearhead semiconductor in the development of integrated light sources. [54]

As part of a material engineering master thesis, the discussions in this chapter will be directed towards the materials used in integrated light-emitting devices. Therefore, this chapter will try to answer the following question:
Which semiconductor material should be used in order to build the most sustainable integrated light-emitting devices?

And to answer this question, a simplified **sustainability assessment of the materials used in opto-electronic devices** is carried out in this chapter.
This sustainabilty assessment will first introduce some *sustainability indicators*. These sustainability indicators will then be used to compare Si, Ge and GaAs-based integrated light emitting devices. Finally, a discussion based on the data that has been gathered will be carried out.

5.1 Actors and industry involved in integrated opto-electronic devices fabrication

Before delving into the sustainability assessment of Si, Ge or GaAs-based devices, a quick look to their associated value chain is mandatory.
The value chain of integrated light-emitting devices describes the processes and actors acting towards the fabrication and distribution of the finished product to the market. Here, from the material

engineer's point of view, it extends from the raw material extraction to the finished product assembly and end of life.
A simplified value chain for Si, Ge and GaAs-based devices is presented on table 5.1.
The most common commercial application of integrated light emitters are optical communication systems used in data centers. Therefore they will be the end product, the commercialised product, in this value chain. [55, 56, 57]

Steps	**Actors** (largest)	**References**
1. Metal smelting, from quartz, to MG[1] metals (outside China,unless mentionned)	Largest smelters and miners : Si: Ferroglobe, Dow, Elkem Ge: Umicore, Teck Ga: Zhuahei, Chalco (China) As: Managem, Umicore	[58, 59, 60, 61]
2. Metal purification to EG[2] metals	Si: GCL-poly, Wacker-Chemie Ge: Umicore, 5N+ Ga, including: PPM Recylcex As, including: Umicore, PPM Recyclex	[62, 59, 60] [61, 63, 64]
3. Wafer production	Si (SOI), includes: SOITEC Ge (GeOI): - Ge, includes: Umicore, 5N+ GaAs, includes: Freiberger, Vital	[65, 59, 66]
4. Device fabrication (integrated light source)	Si + GaAs hybrid laser technology Includes: Luxterra, Global Foundries, IMEC	[3, 56, 55]
5. Final product assembly (Optical communication systems)	Includes: Intel, Global Foundries, IMEC	[57, 56, 55]
6. End of life and recycling	-	-

Table 5.1: Simplified value chain associated to the fabrication of integrated opto-electronic devices, especially integrated light sources, listed manufacturers of different goods were (publicly) active in 2020.

[1] Metallurgical Grade semiconductors, see section 5.3
[2] Electronic Grade semiconductors, see section 5.3

5.2 Scope and assumptions

A perfect sustainability assessment comparing Si, Ge and GaAs integrated light emitting devices would study the life cycle of every kind of these devices, from their primary ores' extraction to their end-of-life. Such a study would deliver an eco-selection index based on every measurable sustainability metrics, through the entire life cycle of the device. This kind of task would require an infinite amount of time and knowledge. Therefore, the scope of this study has to be limited somewhere.

Firstly, all the integrated light emitting devices considered here are equal in performance and can perform the exact same tasks. **The only point of comparison between the devices is the semiconducting material they are made of**.

Secondly, to narrow down the study and provide more precise results, **the scope will be limited to the production of Si, Ge and GaAs wafers.**
The sustainability assessment will therefore be based on considerations directed towards the fabrication of three, identically sized wafers, made from each of the three semiconductors.
This means that only the 3 first steps of the value chain are considered. Steps *4.*, *5.* and *6.* will not be adressed.

This heavy limitation is justified by the following observations and assumptions:

- First, a technological boundary intrinsically limits the scope of this assessment: to this day, strained Si and Ge integrated light sources are not mature and commercialised technologies. Only GaAs-Si hybrid integrated lasers are already being used at commercial scale.[3]
  Thus, the **microfabrication processes** used to build the devices **cannot be compared**, as no reference exists for strained Si and Ge devices. Discarding this part of the device manufacture process is a heavy simplification, as microfabrication techniques are energy intensive and wasteful processes that could be a source of divergence between the sustainability assessment of Ge, Si and GaAs-based devices.

- In the wake of the previous argument, as commercial application of strained Si and Ge integrated light sources exists, neither the use nor the end-of-life stages of the three materials can be taken into account.
  Thus, the following assumptions are made:
  1. **The "use" stage of the devices' life cycles can't be used to differentiate the devices**.
  2. **The end-of-life is equivalent for devices made out of Ge, Si or GaAs**. Indeed, this stage is fundamentally similar for any Si, Ge or GaAs integrated device: integrated chips are not recycled. It is very likely that end-of-life considerations wouldn't be able to differentiate Si, Ge or GaAs anyway. [59]

- The limitation to the wafer production stage makes sense in the framework of the fabrication of integrated light sources and optical interconnections. Indeed, it is common for Si, Ge or GaAs integrated light sources to start their life as a Si, Ge or GaAs wafer.
  - **GaAs** can be used either as a material platform on which all the photonic circuitry is integrated, or as a standalone, hybrid integrated, light source on a silicon substrate. In either cases, the devices are built from a GaAs wafer. Indeed, GaAs is rarely grown direcly on Si substrate by means of epitaxy or other growing technique. Instead, the most common

integration technique is the bonding of unprocessed dice[3] of GaAs on SOI[4] wafers. This method is the current way-to-go for manufacturers of hybrid integrated lasers. A schematic representation of this process is shown on figure 5.1. [67]

- **Silicon** being the standard substrate materials, silicon opto-electronic devices are always built on Si, or more often, SOI wafers.

- **Ge** integrated devices introduced in the State-of-the-art were all made on GeOI wafers. GeOI wafers are fabricated from the SmartCut process, which uses both a Si and a Ge wafer. However, Ge light sources integrated on silicon substrates are also being researched. These require Ge layers growth on Si substrate. In this scenario, the life cycle of germanium doesn't include a wafer production step. Instead, epitaxy and chemical vapor deposition of Ge are used, which require precursor gases ($GeCl_4$, GeH_4) instead of a Ge wafer. [3, 68]

This last fact underlies a flaw in the limitation of the scope to the wafer production stage.

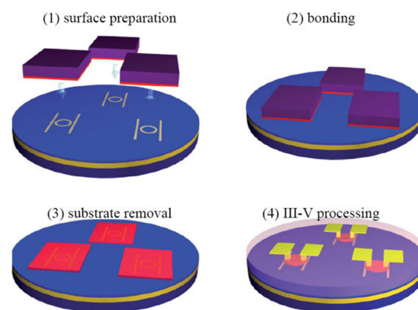

Figure 5.1: Hybrid integrated III-V/Si laser fabrication using die-to-wafer bonding. The red film is made out of III-V material, GaAs or InP, while the blue substrate is silicon, a SOI substrate in this representation from [67].

5.3 Si, Ge and GaAs wafers industrial fabrication

As the scope limits the value chain to its first 3 steps, details about these first three steps are given in this section. This short introduction to wafer manufacturing serves as a reference for the latter parts of this chapter.

The common production steps for the production of Si, Ge or GaAs wafers are:

1. The primary ores reduction to metallurgical grade (MG) metals, commonly 95-99% pure metals.

2. Further refining to electronical grade (EG) metals, here considered to be **6N**, or 99.9999% pure metals

Since opto-electronic devices require very high purity, an ultra purification step could be taken into account:

3. Optional: Ultrapure-refining to 7-9N pure metals.

4. Monocrystalline growth process and slicing

[3]Dice are square cut-outs from wafers, which often contains the finished integrated circuit. Most of the time, finished chips are "diced" out of the wafer on which they were processed

[4]Silicon On Insulator

Silicon wafer production

Silicon wafers start their life as high purity quartz, SiO_2. The quartz rocks are purified to metallurgical grade silicon by smelting, through the carboreduction reaction:

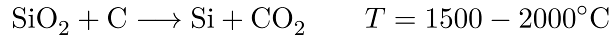

$$\mathrm{SiO_2 + C \longrightarrow Si + CO_2} \qquad T = 1500 - 2000°\mathrm{C}$$

MG silicon is then purified to electronical grade Si through the Siemens process, which includes silicon chlorination, distillation and reduction. the Siemens process can be summed up with the following equations:

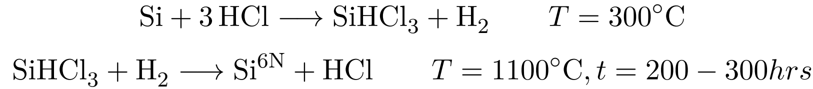

$$\mathrm{Si + 3\,HCl \longrightarrow SiHCl_3 + H_2} \qquad T = 300°\mathrm{C}$$

$$\mathrm{SiHCl_3 + H_2 \longrightarrow Si^{6N} + HCl} \qquad T = 1100°\mathrm{C}, t = 200 - 300hrs$$

This process reaches the 6N purity threshold, further refining can be achieved through zone refining. Finally, monocrystalline ingots of silicon are obtained through the Czochraski (CZ) growth technique, from which wafers are sliced out. [69]

Germanium wafers production

Germanium is not mined from a dedicated ore source. Instead, it is obtained as a by-product of the zinc extraction industry or by extraction from coal fly ashes. Thus, Ge has to be first concentrated from low-concentration scraps. Ge is concentrated in its oxidised form GeO_2. The oxide is then chlorinated to $GeCl_4$ in order to be refined through distillation:

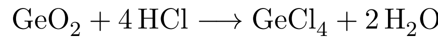

$$\mathrm{GeO_2 + 4\,HCl \longrightarrow GeCl_4 + 2\,H_2O}$$

After distillation, the reverse reaction is used to obtain 6N pure germanium oxyde:

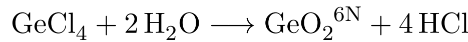

$$\mathrm{GeCl_4 + 2\,H_2O \longrightarrow {GeO_2}^{6N} + 4\,HCl}$$

Which is readily reduced by hydrogen to its metal form:

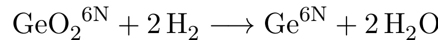

$$\mathrm{{GeO_2}^{6N} + 2\,H_2 \longrightarrow Ge^{6N} + 2\,H_2O}$$

Just as silicon, Ge ingots can then be further refined through zone-refining and Ge wafers are sliced out mono-crystalline ingots obtained from CZ growth. [70]

GaAs wafers production

Before being mixed to form GaAs, gallium and arsenic are separately extracted and refined.

Gallium

Similarly to Ge, Ga is obtained as a by-product from the aluminium and zinc metallurgy. The majority of Ga production originates from the Bayer process of Al production. Gallium solutions are first enriched through electrolysis. Metallic Ga is obtained from another electrolysis process. Refining to 4N purity requires high temperature O_2 and acid treatment. Purification to 6N purity requires zone refining. [71, 69]

Arsenic

Arsenic is obtained commercially by the condensation of vapors obtained from smelting minerals, such as $FeAs_2$ or FeAsS, in the absence of air:

$$\mathrm{FeAsS \longrightarrow FeS + As_{v.} \longrightarrow As_{s.}}$$

Electronic grade (6N) arsenic is obtained through zone-refining. [69]

Once electronic grade Ga and As are obtained, the synthesis of GaAs is done through a direct reaction between As vapours and liquid gallium, as shown on figure 5.2. Afterwards, a common way to obtain single crystal GaAs wafers is through the CZ process, like Ge and Si wafers.

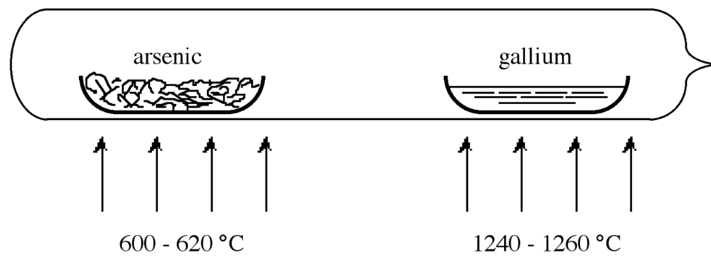

Figure 5.2: Schematical representation of sealed tube synthesis of GaAs, from [69]

5.4 Systemic and multidisciplinary approach to the sustainability assessment

The scope of the study has been set, some technical knowledge about wafer fabrication has been gathered, but a method to assess the sustainability of Si, Ge and GaAs wafers needs to be defined.

5.4.1 Assessment of sustainability through indicators comparison

The method that is chosen will follow a **systemic impact evaluation, by means of comparison indicators**. The sustainability assessment is intended to be as comprehensive as possible, therefore it takes a systemic view at the materials level by assessing them against environmental, socio-economic and legislative frameworks. This multidisciplinary study will be based on the comparison of different sustainability indicators. These indicators are related to the different frameworks embodied in a sustainability assessment. They are split in four categories, namely the *Environmental*, *supply chain*, *regulation* and *societal impact* considerations associated to a product.

In sum, the sustainability assessment of the Si, Ge and GaAs wafer production will be made by means of various comparison indicators according to the roadmap presented on figure 5.3.

The sustainability indicators presented on the roadmap are introduced and detailed in the following sections and table 5.2 lists the results. Given the limited resources and expertise of this study, only a few indicators have been chosen. However, they are chosen to be as comprehensive as possible.

5.4.2 Indicators linked to the environmental impact of the wafer production

Here, the environmental impact related to the production of standard Si, Ge and GaAs wafers will be discussed and quantified through appropriate indicators.

The reference element will be the current standard **"300mm" wafer**, with dimensions: $300 \times 0,775mm$ (Diameter × thickness, standard dimensions for silicon wafers). Though it may not be the most common size for Ge or GaAs wafers, it is a standard size nonetheless. Thus, each wafers are considered to be $300 \times 0,775mm$ in size. [72, 73]

To measure the environmental load of the 300mm wafer production, three indicators will be used:

- **Embodied energy:** the embodied energy represents the cumulative energy required to fabricate an object or material. Embodied energy can be evaluated through a Cumulative Energy Demand method, for instance. It can be expressed in $[MJ/kg]$ or $[MJ/unit]$ depending on the context. The embodied energy indicator describes the environmental impact of the production of the three wafers, for material sourcing and finished products fabrication (sliced 300mm wafers). A high embodied energy is a good indicator of poor environmental sustainability. **??**.

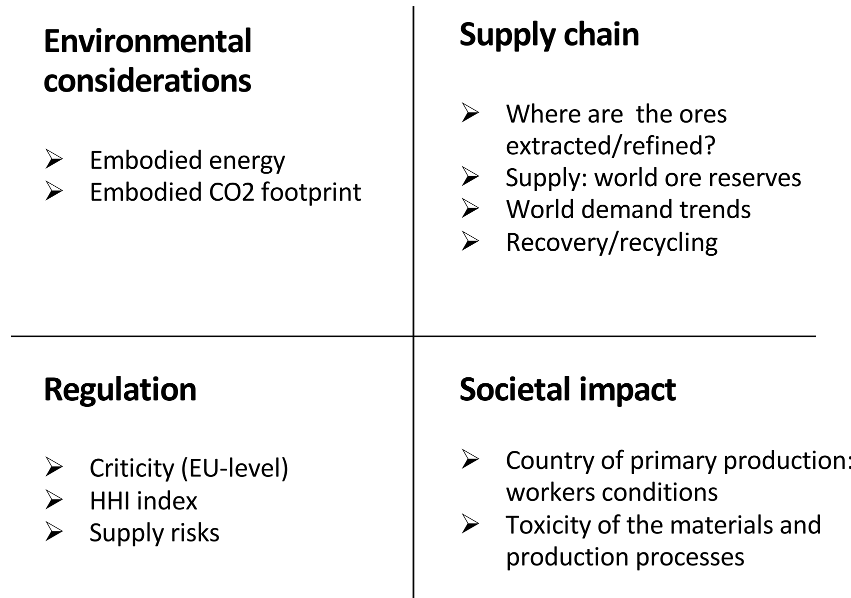

Figure 5.3: Roadmap for differents categories of sustainability indicators for Si, Ge and GaAs integrated light sources

- CO_2 **footprint**: the CO_2 footprint quantifies greenhouse gases emitted during the production of a certain unit of material or object. This indicator will be used to describe the environmental local caused by the primary production of metallurgical grade Si, Ge and GaAs. Evaluation of the CO_2 footprint of the wafer production from raw metals is not conceivable for the scope of this work.
- **Water usage:** describes the volume of water needed to process a material/object. In the same spirit as the previous indicator, it will be used to further describe the environmental load of the raw materials production.

Embodied energies of Ge, Si and GaAs as material feedstock and as finished products have been listed and computed on table 5.2.

Embodied energies of the Si and GaAs wafers have been computed from data coming out of LCA studies. [74, 75]
No data for Ge wafer production have been found, as such studies have yet to be made on Ge wafers. Sadly, as the Ge wafer production differs from Si and GaAs wafers, no extrapolation and no educated estimate of the embodied energy can be given.

5.4.3 Indicators linked to the supply chain

Here, the **sustainability of the supply** of Si, Ge and GaAs wafers is assessed.
Issues surrounding primary ores resources[5], supply and demand will be described and quantified using the following indicators:

- **Material resources**: describes the quantity of economically prospectable metal in known deposits. Expressed in [Mt], a material with low amounts of reserves suffers from poor supply sustainability.

[5]A mineral resource is a known occurrence of a mineral in such concentration or quantity that it could reasonably be economic to prospect.

- **Production**: describes the quantity of metallic Si, Ge and Ga[6] produced per year and the major producing countries. It is not a sustainability indicator by itself, but is a useful information to better understand the Supply Risk and $\frac{Demand}{Production}$ indicators.

- **Recovery/recycling**: describes the amount of recovered material in the material's global substance flow. Examples of global substance flows are given in the appendices, on figure C.1 and figure C.2 for gallium and germanium.

  The amount of recovered/recycled material is expressed as a percent of the material's total annual production. There are two types of recovery/recycling in a material's global substance flow. The first one is the Pre-Consumer (PC) recovery, the second is the End-Of-Life (EOL) recycling. The first one covers the recovery of scrap material inside the industrial production, while the second one addresses the recovery of material after use by the consumer. Poor EOL and PC figures negatively impact the sustainability of a material.

- $\frac{Demand}{Production}$ **trends**. A comparison between an actual and (evaluated) future $\frac{Demand}{Production}$ ratio gives an indication whether the supply of the material can keep up with the demand. A ratio close to 1 is a bad sign.

5.4.4 Indicators linked to regulations

Regulations and their expected evolution also affect the sustainability of the semiconductor wafers production.
To assess this aspect, the following indicators are used:

- **Supply risk (SR)**: indicates whether the supply chain of a material or object is subject to abrupt disruptions. Here, the EU definition of Supply Risk is used. It is based on the european reliance on foreign productor countries and the stability of their supply. [76]
  The Supply Risk is scaled between 0 (safe) and 8 (most critic). The higher the SR value, the less sustainable the supply is. A SR above a maximum threshold value, 1 for the EU, is a necessary but not sufficient condition to consider the material to be a Critical Raw Material.

- **Criticity of the material**: a material is considered, for the EU, as a Critical Raw Material if its Supply Risk and Economic Importance both exceed a certain threshold. Critical materials are, *de facto*, less economically and strategically sustainable than non-critical materials.

- **Environmental country risk Herfindahl-Hirschman Index**: indicates the risk for the worldwide supply of a material to be restricted by environmental protection regulations. A higher value means a greater risk for the supply to be restricted in the future. The **Environmental country risk level** is simply the qualitative (low-high) supply risk associated to the HHI value.

5.4.5 Indicators linked to social impact

Last but not least, the impacts of the wafer production on society has to be taken into account. Health hazard and workers conditions will be assessed and quantified using the following indicators:

- **Workers condition**: Workers conditions is a concern mainly for the first step in the value chain, the primary ore extraction and smelting. However, as most of Si, Ge and Ga are mined and smelted in China, one can't really differentiate the work conditions associated to the extraction activity. Only a knowledge of the difference between the Si, Ge and Ga extractive industries *inside* China could help to bring any meaningful information.

- **Toxicity**: indicates whether the object or its components contain toxic elements. Since wafers are made out of a single materials, this task is easy. Toxicity is quantified using the European Chemical Association nomenclature. This nomenclature attributes toxicity labels to materials. If a material is safe, no label is given, if it is somewhat dangerous, the "warning" label is given

[6] Ga instead of GaAs, see justification at the beginning of section 5.5

and if the material is toxic, the "danger" label is given. Moreover, if a material is toxic, its properties of concern are given and scaled (from *suspected* to *recognised* carcinogenic, mutagenic, ... properties).

5.5 Results and discussion

The indicators previously introduced are listed in the table table 5.2.
The indicators are given for silicon, germanium and **gallium**, not gallium arsenide, unless stated otherwise. Indeed, for most of the indicators, gallium is the "limitating element" between Ga and As. Contrary to As, Ga is considered to be a Critical Raw Material.

	Si	**Ge**	**Ga(As)**	**Sources**
Supply chain metrics				
Resources [Mt]	"largely sufficient"[7]	356	760-1000	[76]
Production in 2020 [t]	≈7000 (China 64%, Russia 8%, Norway8%)	≈130 (China 65%, Russia, Belgium)	≈ 320 (China 97%, Russia, Ukraine <3%)	[77]
Recovery/Recycling	EOL[8] : no - PC[9]: "slight"	EOL: 2% - PC: >30%	EOL: <1% - PC: >70%	[76, 78]
$\frac{Demand}{Production}$ figures for 2013-2035	No data	0,4→0,8	0,3→0,4	[79]
Regulations-related metrics				
Supply risk (Scale 1 - 9)	1,6	1,9	1,8	[76]
Criticity (EU level)	Yes	Yes	Yes (As: no)	[76]
Environmental country risk HH index and risk level	missing	3,59 = high risk	3,53 = high risk	[80]
Social impact metrics				
Primary production: workers conditions	-	-	-	
Health and toxicity issues	No classified hazards	"Warning" label	Ga: "Warning" label As: "Danger" label GaAs: "Danger" label, + Recognised as: Carcinogenic, Toxic to reproduction	[81, 82] [83, 84, 85]
Environmental considerations associated with the wafer production				
Primary ore production: water usage [l/kg_{metal}]	23,2-25,7	9390-10400	3610-3990 (As:36)	[80]
Primary ore production: CO2 footprint [$CO_{2eq.}/kg_{metal}$]	4,78-5,27	47-51,9	198-218 (As: 0)	[80]
Primary ore production: Embodied energy [MJ/kg_{metal}]	116-218	871-963	2920-3120 (As: 0)	[80]
Wafer: embodied energy [MJ/wafer]	239,8	Insuffcient data	588,9	[75, 70, 74]
Wafer weight [kg]	0,175	0,278	0,278	

Table 5.2: Comparison of sustainability indicators between the production of Si, Ge or GaAs wafers. According to the available data, green cell means the material performs better than the other two, a red cell means the material performs the worst.

With the data of table 5.2, it is now possible to assess and compare the environmental cost associated to the production of Si, Ge and GaAs wafers.

From an objective point of view, one can state that overall, a silicon wafer performs better than Ge and GaAs wafers for most of the sustainability indicators listed on table 5.2, with the exception of recycling.

Therefore, the first implication that one could draw is that the environmental, socio-economic and geopolitical tolls of silicon wafer production are lesser than those of Ge and GaAs wafers. This implication would indicate that, **for similar tasks and performance, a silicon-based technology outperforms Ge or GaAs-based alternatives in terms of material sustainability**.

One could try to go a step further and translate this statement about Si, Ge and GaAs wafers to Si, Ge and GaAs-based devices (the integrated light emitters). However, as mentioned in the scope

[7] Largely sufficient fto supply the next decades, according to the European Commission report [76]
[8] EOL = End-Of-Life, see above
[9] PC = Pre-consumer, see above

section, while wafers made from different materials are comparable, integrated light emitters made from different materials are much less comparable.
As a matter of fact, while Ge-based integrated lasers and GaAs-only photonic circuitry use GeOI and GaAs wafers, hybrid integrated laserd only use a small quantity of GaAs on a Si wafer (as shown on figure 5.1). This makes the comparison between the different type of devices tedious and uncertain with only the data provided by the comparison of wafers.

Even though a rigorous comparison between the different end devices might be out of reach, the data provided by the sustainability assessment of the three types of wafers can still yield interesting results. Indeed, one could make this first supposition:
When an application requires the use of Ge or GaAs in a device, manufactures should maximise the ratio of quantity of silicon over quantity of Ge or GaAs to create a device with the highest material sustainability. This proposition aligns well with the observations made in the state-of-the-art of this master thesis. As a matter of fact, full silicon-based optical interconnection are, to this day, still unavailable. Thus, if a silicon-based optical interconnection is impossible, it is still possible to develop a solution that mitigates the environmental impact by maximising the ratio of quantity of silicon over quantity of Ge or GaAs.

Secondly, another interesting implication coming out of the data from table 5.2 concerns recycling. It is stated that the silicon used in the fabrication of Si wafers undergoes very little to no recycling, inside the industrial loop as well as in the end-of-life of devices containing silicon. While the recovery of silicon from any integrated devices, seems out of reach today, the recycling of Si inside the industrial loop (Pre Consumer, PC, recycling) is not inconceivable. Indeed, 30 and 70% of the entire annual production of Ge and Ga (respectively) originates from recycled industrial Ge and Ga scraps. Although the manufacturing processes of Si, Ge and GaAs is not identical, the description of those processes given in the previous section, section 5.3, underlies a lot of similarities between them. Thus, one could make the stretch and argue that the industrial fabrication of silicon has the potential to use more material recovered from production scraps. One could also argue that it doesn't make sense to stretch the usage of scraps in Ge and Ga to the Si industry, as Ge and Ga are much more valuable metals[10]. Still, one could make the following statement: **To build a silicon-based device with increased material sustainability, a device manufacturer should use a wafer that contains a maximal amount of silicon recovered from scraps. At the same time, wafer manufacturers should integrate as much recovered silicon as possible in their final product.**

As a final remark, it must be underlined that photonics are, to this day, still an emerging technology with very few commercial applicationd. Thus, for a work with limited scope and resources, the implications of the introduction of photonics technology to a large scale implication can't be discussed here. This means that sustainability considerations related to the replacement of electronic systems by photonics systems, or the creation of new systems based on photonic devices won't be discussed here. However those discussions should take place and it is the duty of the engineering community to evaluate whether photonics, as fascinating as they might be, can, overall, positively contribute to a more sustainable future.

[10]Price [$/kg] (2019): Si≈2.64, Ga≈350, Ge≈950, from [77]

Chapter 6

Conclusion

No conclusion regarding the opto-electronic properties enhancement through strain engineering can be drawn from this interrupted work. However, the sustainability of the materials used in integrated light emitting devices could still be discussed. The study was limited to the comparison between wafers made from three main semiconductor materials. The results and discussion of this short study led to the following statements. For similar tasks and performance, a silicon-based technology outperforms Ge or GaAs-based alternatives in terms of material sustainability. Moreover, when an application requires the use of Ge or GaAs in a device, manufactures should maximise the ratio of quantity of silicon over quantity of Ge or GaAs to create a device with the highest material sustainability. Finally, to build a silicon-based device with increased material sustainability, a device manufacturer should use a wafer that contains a maximal amount of silicon recovered from scraps. At the same time, wafer manufacturers should integrate as much recovered silicon as possible in their final product.
This discussion about sustainability was limited by its scope, which did not include the fabrication of actual devices, but stopped at the fabrication of wafers. In addition to this, the discussion is based on the comparison between indicators, whose choice were limited by the available data at the time of writing this work and my own, limited, expertise.

Concerning the improved data reduction scheme: the integration of a correction model inside the data reduction scheme has proven to be generally successful. Experimental data treated with the correction model yielded more precise stress-strain curves than without the correction model, both for brittle and ductile samples. In every studied cases, corrected stress strain points were less spread out than non-corrected ones, a sign that the correction model compensates the effect of the structure's geometry on the results. The precision was improved from 27.8% of relative error on the Young's modulus down to 9.704% with the correction model applied on experimental data from tensile test performed on ZnO (with $E^{ZnO} = 100GPa$ as reference). However, the case of ductile samples is prone to more uncertainty than the case of brittle samples. There were fewer reliable experimental data sets on ductile samples to thoroughly study the behaviour of the correction model.
The correction model is limited by the fact that the models used to compute α_{approx} and β_{approx} are empirical models. Their modelling is mainly limited by the respectively unknown and uncertain contributions of the sample's thickness and width.
Furthermore, some unexpected behaviours of the correction model still cast a shadow on its accuracy, such as the behaviour[1] of the β parameter for ductile materials.
Finally, the model's dubious evaluation of the strain in the dog bones and overlap elements of the lab-on-chip structure is also a crucial limitation of the model's accuracy.
To get the best out of the correction model, the following guidelines should be followed:

- For brittle samples, structures with dimensions where the h-value $h = \frac{L^s_{g,0} W^s_{g,0}}{(L^s_{g,0})^2}$ is smaller than 10^{-4} should be treated carefully, as they lead to unstable approximations of α_{approx}.

[1]While misunderstood, the β parameter's behaviour is still predictable and doesn't jeopardise the accuracy of the correction model.

- An identical actuator width is required inside a single data set. An entire experiment made with a fixed actuator width is the best case scenario.
- The correction model is extremely sensible to the actuator's mismatch strain ε^{a}_{mis}. It should be measured with great care.
- The correction model is also sensible to the under-etch's length $L_{ue,0}$, but less critically than the actuator's mismatch strain. If it can't be measured, it should be precisely approximated by means of the over-etch time and etch rate.
- Short actuators combined with short samples (ie: sample and actuator length $\leq 50[\mu m]$) lead to considerable errors on the evaluated sample displacement u_g. They should be avoided.

To go further with this work, the first step would be to generate more reference data with FE simulations, including variations of the sample and actuator width and thickness. This would allow to challenge the correction model and enhance the modelling of the α_{approx} and β_{approx}.
The next step would be to review some hypotheses of the correction model. Some hypotheses linked to the behaviour of the dog bone and the overlap regions and under-etched region need to be reviewed. More specifically, the stress state in the dog bone connected to the frame should be investigated carefully to study the eventual apparition of shear stresses. Additionally, the overlap region should be modelled differently to take into account the layer of actuator material resting on top of it. Finally, a FE simulation of the under-etched segment could help figure out the unexplained behaviour of the β parameter for ductile samples.

Finally, the software developped for the data reduction scheme is available on One Drive with this link: https://uclouvain-my.sharepoint.com/:f:/g/personal/apip_oasis_uclouvain_be/EjBj21ck4kBOmq5Ik9DS36ABL4PJtQh7vYWn9pZWemvntw?e=dd62us

Appendix A

Electronic band structure modelling, supplementary models

The Pseudopotential method

The pseudopotential method, to describe band structure, stems from another type of approximation to the Schrödinger equation of an electron than the one used for the NFE approach. Here, using the concept of pseudopotential, it is possible to rewrite the one-electron Schrödinger equation Equation 2.3 in term of pseudo-wave function. This is called the **pseudo-wave-equation**. $V(r)$ is the pseudopotential and p the momentum of the electron.

$$\left[\frac{p^2}{2m} + V(r_i)\right]\psi_k(r_i) = E_k\psi_k(r_i) \tag{A.1}$$

This model relies on an approximation of the potential exerted by the atom to its conduction valence electrons. It is assumed that, the wavefunction of those electrons can be divided into a smooth "pseudo-wave" function and an oscillatory part. As opposed to the core electrons, the conduction and valence electron can be seen as influenced only by the weak pseudopotential. This allows to simplify the Shrödinger equation to equation Equation A.1 and only consider valence and conduction bands, ditching the useless core states.

To draw the band structures, E_k and the ψ_k function have to obtained, however to find them, it is required to express the pseudopotential $V(r)$ first. The pseudopotential $V(r)$ is expressed as a matrix whose elements are hard to get, as the depend on pseudopotential form factors. Those form factors can be computed for certain material, they are computed for Ge and are shown in table Table A.1. Once the calculations are done, it is possible to draw the band structure shown on figure Figure A.1, for silicon. These band calculations include the effect of spin-orbit coupling. [20]

	V_3^s	V_8^s	$V_1 1^s$	V_3^a	V_4^a $V_1 1^a$	
Si	-0.211	0.004	0.008	0	0	0

Table A.1: Pseudopotential form factors for Si, in Rydbergs = $13eV$, from [20]

One way to compute the pseudopotential form factors is to use experimental data from optical reflectivity spectra or photodetection spectra. This approach is called the **Empirical Pseudodpotential Method**. It is also possible to disregard the need for experimental data and go straight to computer simulation to get the pseudopotential form factor thanks to first principles. Those method are known as *ab-initio* pseudopotential method.

The $k \cdot p$ method

What makes the $k \cdot p$ method attractive is that it allows to extrapolate the band structure from the energy gaps at the Γ (0,0,0) point and experimental result.

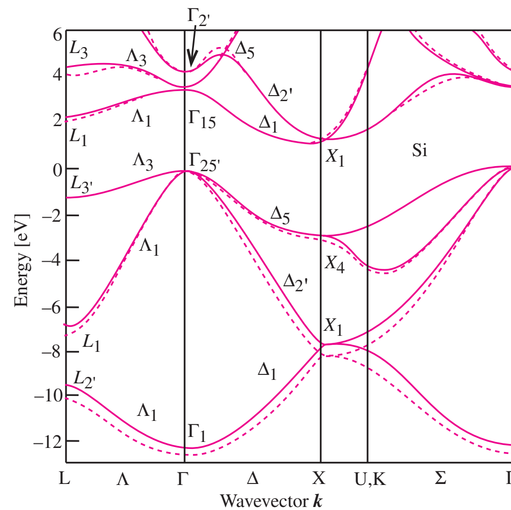

Figure A.1: Band structure of Si from the pseudopotential method, from [20]. The 0 in energy is set at the top of the valence band at the Γ point in the Brillouin zone. The high symmetry points and direction have "double goup" notation on this figure.

This method is derived from the one-electron Schrödinger equation Equation 2.3, whose solutions are, here, expressed according to the Bloch theorem:

$$\Phi_{nk} = e^{ik \cdot r} u_{nk}(r) \tag{A.2}$$

Where n is the band index, k is the wavector in the first Brillouin zone and u_{nk} the lattic periodicity function. Once plugged in equation Equation 2.3, the Schrödinger equation becomes:

$$\left(\frac{p^2}{2m} + \frac{\hbar k \cdot p}{m} + \frac{\hbar^2 k^2}{2m} + V \right) u_{nk} = E_{nk} u_{nk} \tag{A.3}$$

Which reduces to, at $k_0 = (0, 0, 0)$:

$$\left(\frac{p^2}{2m} + V \right) u_{n0} = E_{n0} u_{n0} (n = 1, 2, 3, ..) \tag{A.4}$$

Which form a complete and orthnormal set of basis functions and can be used to compute E_{n0} and u_{n0}. The next step used in this method is to apply perturbation theory on the $\hbar k \cdot p/m$ and $\hbar^2 k^2/(2m)$ terms in equation Equation A.3. This allows to work out the band structure around the k_0 point, when the wave function[1] and energies at k_0 are known. Both of those required results can be measured experimentally.
In general, this method can be applied to any k_0, provided the energies and wave function at this k_0 can be measured experimentally.
Furthermore, the treatment of the $k \cdot p$ term by the perturbation theory can be done using either degenerate or nondegenerate perturbation theory. This is helpful to distinguish the computation for degenerate and nondegenerate bands.

The band structure historically obtained in 1966 from this method is shown on figure Figure A.2, for germanium.

[1] Or the matrix elements of p between the wavefunction. [20]

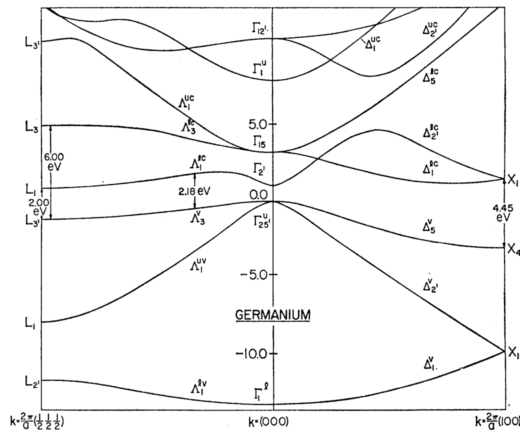

Figure A.2: Band structure in Ge along the [1 1 1] and [1 0 0] direction in the reciprocal space. From [86]

Appendix B

Data reduction scheme: results

Dimensions [μm]																
Sample			**Actuator**	α_{min}	$\Delta_{rel}F$ [%]	$\Delta_{rel}\sigma$ [%]	β_{min}	$\Delta_{rel.}u_g$ [%]	$\Delta_{rel}\varepsilon$[%]	α_{approx}	$\Delta_{rel}F(\alpha_{approx.})$ [%]	$\Delta_{rel}\sigma(\alpha_{approx.}, \beta_{approx})$ [%]	β_{approx}	$\Delta_{rel}u(\beta_{approx.})$ [%]	$\Delta_{rel}\varepsilon(\alpha_{approx.}, \beta_{approx})$ [%]
$L_{g,0}$	$W_{g,0}$	$t_{g,0} = t_{a,0}$	$L_{a,0}$												
50	1,5	1	50	0,945	2,43E-03	4,23E-03	1,406	0,838	0,462	0,950	0,701	0,714	1,446	6,369	3,502
50	1,5	1	100	0,922	-9,26E-04	1,61E-03	1,339	0,744	0,491	0,876	-2,655	-2,638	1,303	5,088	3,349
50	1,5	1	450	0,793	1,31E-05	6,23E-03	1,206	0,643	0,542	0,736	-0,304	-0,265	1,168	3,971	3,334
50	1,5	1	1500	0,291	1,23E-05	1,12E-02	1,174	0,628	0,565	0,197	-0,072	-0,006	1,138	3,695	3,314
100	1,5	1	50	0,953	-3,81E-03	-3,46E-03	1,607	0,531	0,119	0,950	-0,700	-0,695	1,648	4,448	1,777
100	1,5	1	100	0,935	1,98E-03	2,81E-03	1,472	0,443	0,229	0,950	1,237	1,243	1,446	3,337	1,728
100	1,5	1	450	0,844	-1,95E-05	2,06E-03	1,251	0,345	0,266	0,804	-0,346	-0,332	1,209	2,227	1,717
100	1,5	1	1500	0,499	-2,78E-05	4,25E-03	1,184	0,325	0,284	0,326	-0,196	-0,170	1,151	1,972	1,721
400	1,5	1	50	0,960	2,14E-03	2,05E-03	1,988	0,300	-0,045	0,950	-2,994	-2,993	1,974	2,881	0,435
400	1,5	1	100	0,946	-1,58E-03	-1,63E-03	1,850	0,213	-0,021	0,950	0,483	0,484	1,857	1,945	0,441
400	1,5	1	450	0,890	-4,97E-04	-2,86E-04	1,475	0,114	0,058	0,863	-0,542	-0,541	1,417	0,844	0,433
400	1,5	1	1500	0,718	1,64E-05	4,82E-04	1,269	0,090	0,067	0,690	-0,080	-0,077	1,225	0,590	0,439
50	4	1	50	0,955	-5,87E-04	-3,52E-04	1,148	0,130	0,069	0,950	-0,315	-0,314	1,157	0,382	0,186
50	4	1	100	0,936	4,87E-04	9,95E-04	1,117	0,194	0,120	0,950	0,321	0,323	1,141	0,513	0,300
50	4	1	450	0,786	7,30E-07	1,49E-03	1,070	0,265	0,207	0,823	0,091	0,096	1,128	0,744	0,561
50	4	1	1500	0,116	9,13E-06	2,30E-03	1,056	0,288	0,240	0,390	0,129	0,135	1,125	0,809	0,655
400	4	1	50	0,965	1,22E-03	1,18E-03	1,286	-0,137	-0,018	0,950	-1,576	-1,576	1,351	0,148	0,020
400	4	1	100	0,952	4,95E-04	4,67E-04	1,257	-0,064	-0,013	0,950	-0,110	-0,110	1,246	-0,097	-0,020
400	4	1	450	0,889	4,38E-05	5,46E-05	1,163	0,007	0,003	0,877	-0,093	-0,093	1,153	-0,010	-0,004
400	4	1	1500	0,628	1,68E-05	1,06E-04	1,097	0,025	0,017	0,800	0,206	0,206	1,133	0,068	0,045

Table B.1: Analytical correction model assessed towards FE simulation results. Precision of the model vs. reference data. Case of a brittle sample (ZnO).

Dimensions [μm]																
Sample			Actuator	α_{min}	$\Delta_{rel}F$ [%]	$\Delta_{rel}\sigma$ [%]	β_{min}	$\Delta_{rel.}u_g$ [%]	$\Delta_{rel}\varepsilon$[%]	α_{approx}	$\Delta_{rel}F(\alpha_{approx.})$ [%]	$\Delta_{rel}\sigma(\alpha_{approx.}, \beta_{approx})$ [%]	β_{approx}	$\Delta_{rel}u(\beta_{approx.})$ [%]	$\Delta_{rel}\varepsilon(\alpha_{approx.}, \beta_{approx})$ [%]
$L_{g,0}$	$W_{g,0}$	$t_{g,0} = t_{a,0}$	$L_{a,0}$												
50	1,5	1	50	0,935	1,64E-03	0,006	0,654	1,849	1,056	0,935	0,260	0,271	0,654	0,260	2,646
50	1,5	1	100	0,922	3,32E-04	0,005	0,661	1,163	0,805	0,929	1,047	1,058	0,677	1,047	2,002
50	1,5	1	450	0,883	-2,17E-04	0,012	0,684	0,817	0,724	0,887	0,132	0,152	0,708	0,132	1,179
50	1,5	1	1500	0,765	1,97E-04	0,026	0,697	0,537	0,498	0,760	-0,045	-0,012	0,716	-0,045	0,652
100	1,5	1	50	0,934	-2,10E-03	0,000	0,649	1,783	0,717	0,935	0,292	0,297	0,633	0,292	1,743
100	1,5	1	100	0,922	-5,73E-04	0,002	0,653	1,067	0,569	0,929	1,086	1,092	0,654	1,086	1,408
100	1,5	1	450	0,883	-4,76E-04	0,003	0,674	0,470	0,381	0,887	0,126	0,134	0,698	0,126	0,777
100	1,5	1	1500	0,765	1,38E-04	0,009	0,692	0,372	0,340	0,760	-0,047	-0,034	0,712	-0,047	0,488
400	1,5	1	50	0,936	1,64E-03	0,002	0,604	1,561	0,230	0,935	-0,239	-0,238	0,623	-0,239	0,586
400	1,5	1	100	0,923	4,00E-03	0,004	0,633	0,982	0,221	0,929	1,083	1,085	0,624	1,083	0,533
400	1,5	1	450	0,879	-4,71E-05	0,000	0,653	0,272	0,143	0,887	0,283	0,284	0,658	0,283	0,365
400	1,5	1	1500	0,768	7,63E-05	0,001	0,672	0,131	0,102	0,760	-0,086	-0,085	0,694	-0,086	0,218
50	4	1	50	0,946	-2,24E-03	0,003	0,724	2,430	1,287	0,935	-1,083	-1,078	0,711	-1,083	1,292
50	4	1	100	0,935	1,05E-03	0,006	0,726	1,476	0,972	0,929	-0,261	-0,256	0,715	-0,261	0,919
50	4	1	450	0,887	-2,60E-04	0,008	0,733	0,647	0,565	0,887	-0,005	0,003	0,718	-0,005	0,531
50	4	1	1500	0,749	-3,50E-05	0,020	0,735	0,493	0,457	0,760	0,033	0,052	0,719	0,033	0,444
400	4	1	50	0,947	8,59E-04	0,001	0,695	1,868	0,247	0,935	-1,509	-1,509	0,669	-1,509	0,231
400	4	1	100	0,935	2,16E-04	0,001	0,711	1,194	0,242	0,929	-0,344	-0,344	0,689	-0,344	0,211
400	4	1	450	0,886	-2,31E-04	0,000	0,723	0,346	0,171	0,887	0,010	0,010	0,712	0,010	0,157
400	4	1	1500	0,756	-1,39E-05	0,001	0,729	0,122	0,092	0,760	0,012	0,012	0,717	0,012	0,085

Table B.2: Analytical correction model assessed towards FE simulation results. Precision of the model vs. reference data. Case of a ductile sample (Pd).

Appendix C

Global substance flows

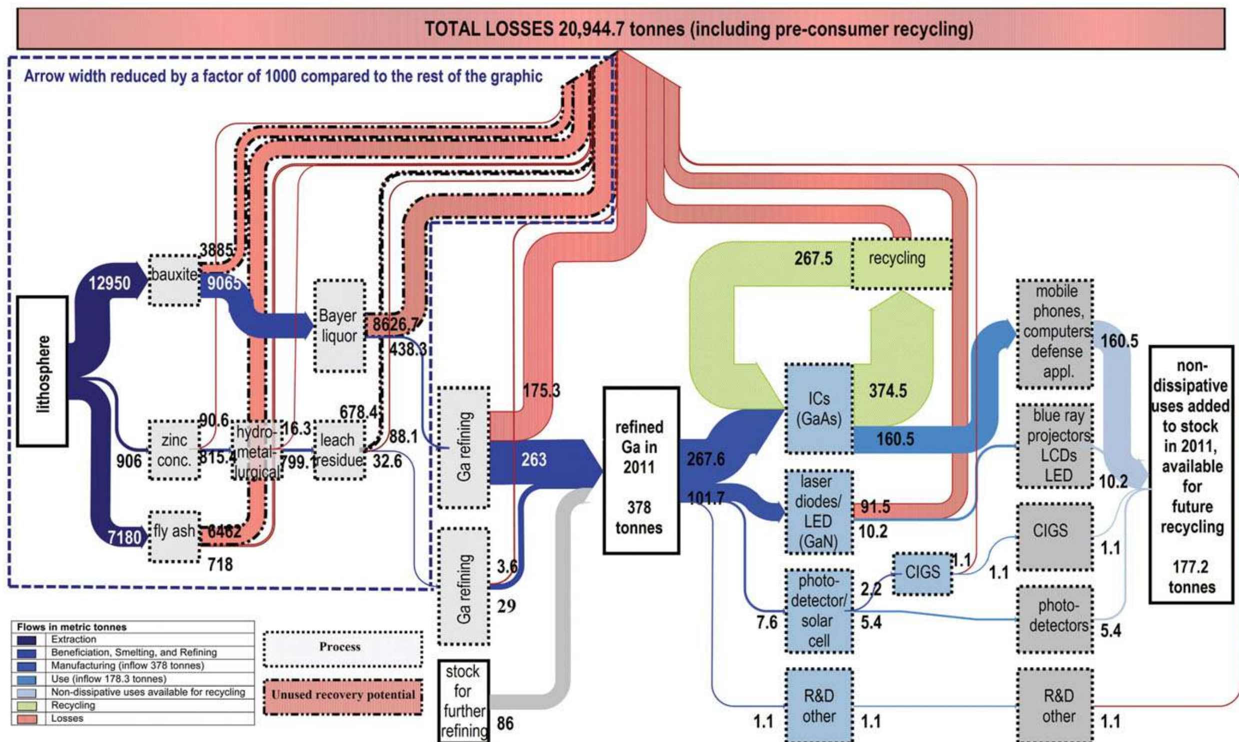

Figure C.1: Global substance flow of gallium in 2011, from [71]

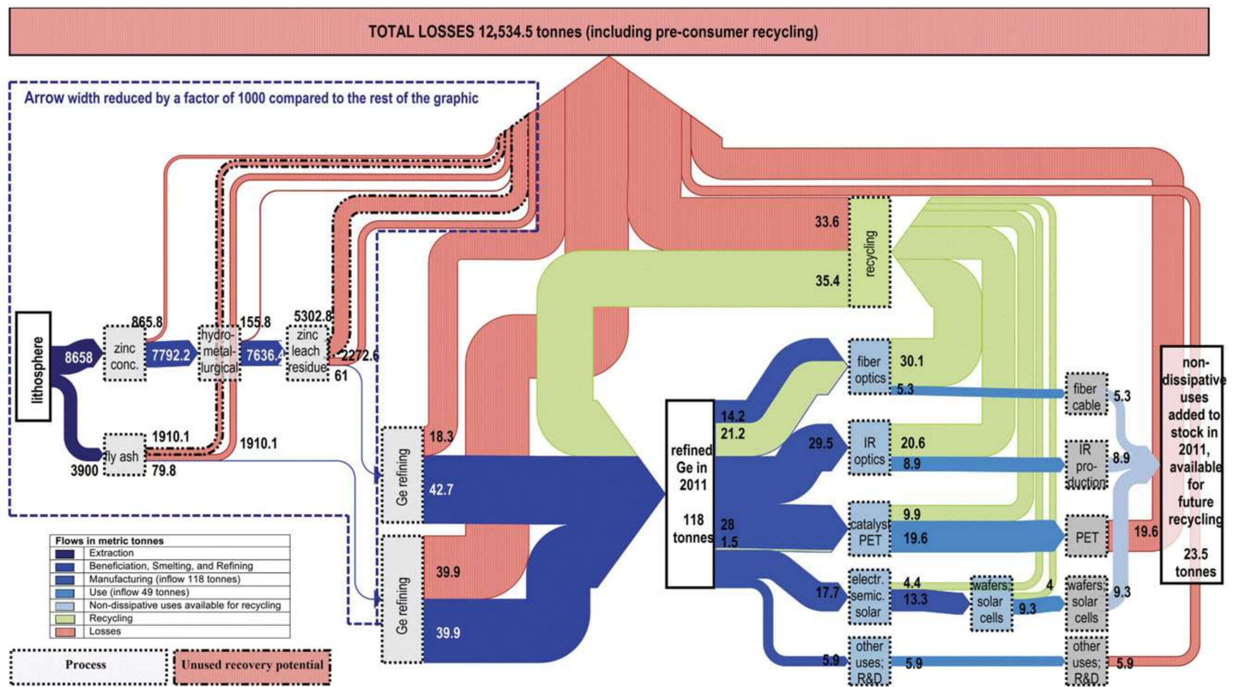

Figure C.2: Global substance flow of germanium in 2011, from [71]

References

[1] Richard Geiger, Thomas Zabel, and Hans Sigg. “Group IV direct band gap photonics: Methods, challenges, and opportunities”. In: *Frontiers in Materials* 2.July (2015). ISSN: 22968016. DOI: 10.3389/fmats.2015.00052.

[2] Marie-Stéphane Colla. “Plasticity and creep in thin free-standing nanocrystalline Pd films”. In: March 2014 (2014), p. 287.

[3] V. Reboud et al. “Germanium based photonic components toward a full silicon/germanium photonic platform”. In: *Progress in Crystal Growth and Characterization of Materials* 63.2 (2017), pp. 1–24. ISSN: 09608974. DOI: 10.1016/j.pcrysgrow.2017.04.004. URL: http://dx.doi.org/10.1016/j.pcrysgrow.2017.04.004.

[4] Xiaochen Sun. “Germanium-on-Silicon for Integrated Silicon Photonics”. In: *Advanced Photonic Sciences* (2012). DOI: 10.5772/25662.

[5] “Performance comparison between copper, carbon nanotube, and optical interconnects”. In: *Proceedings - IEEE International Symposium on Circuits and Systems*. 2008, pp. 2781–2784. ISBN: 9781424416844. DOI: 10.1109/ISCAS.2008.4542034.

[6] Krishna Saraswat. “Silicon compatible optical interconnects”. In: *2016 IEEE International Interconnect Technology Conference / Advanced Metallization Conference, IITC/AMC 2016* (2016). DOI: 10.1109/IITC-AMC.2016.7507739.

[7] A. Rahim et al. “Expanding the Silicon Photonics Portfolio With Silicon Nitride Photonic Integrated Circuits”. In: *Journal of Lightwave Technology* 35.4 (Feb. 2017), pp. 639–649. ISSN: 1558-2213. DOI: 10.1109/JLT.2016.2617624.

[8] S. E. Thompson et al. “In search of "Forever," continued transistor scaling one new material at a time”. In: *IEEE Transactions on Semiconductor Manufacturing* 18.1 (Feb. 2005), pp. 26–36. ISSN: 1558-2345. DOI: 10.1109/TSM.2004.841816.

[9] Unknown. *Technology Node*. Accessed: 2020-01-19. URL: https://en.wikichip.org/wiki/technology_node#Meaning_lost.

[10] Unknown. *7nm lithography process*. Accessed: 2020-01-19. URL: https://en.wikichip.org/wiki/7_nm_lithography_process.

[11] Cepheiden. *Integrated circuits, fabrication techniques, the CMOS process*. Accessed: 2020-01-19. URL: https://en.wikipedia.org/wiki/Integrated_circuit#/media/File:Cmos-chip_structure_in_2000s_(en).svg.

[12] Xiaochi Chen et al. “Surface Treatment of Ge Grown Epitaxially on Si by Ex-Situ Annealing for Optical Computing by Ge Technology”. In: *IEIE Transactions on Smart Processing and Computing* 3 (Oct. 2014), pp. 331–337. DOI: 10.5573/IEIESPC.2014.3.5.331.

[13] Hao Zhang et al. “Optical waveguide materials, structures, and dispersion modulation”. In: *Nanophotonics and Micro/Nano Optics III* 10027 (2016), p. 100270D. ISSN: 1996756X. DOI: 10.1117/12.2249446.

[14] Molly Piels and John E. Bowers. *Photodetectors for silicon photonic integrated circuits*. Nov. 2015. URL: https://www.sciencedirect.com/science/article/pii/B9781782424451000014.

[15] Barry L. Shoop, Andre H. Sayles, and Daniel M. Litynski. *New Devices for Optoelectronics: Smart Pixels*. Sept. 2007. URL: https://www.sciencedirect.com/science/article/pii/B9780122078927500114.

[16] Papichaya Chaisakul et al. "Integrated germanium optical interconnects on silicon substrates". In: *Nature Photonics* 8.6 (2014), pp. 482–488. ISSN: 17494893. DOI: 10.1038/nphoton.2014.73.

[17] Christian Brendel. "Topologically Protected Transport of Phonons at the Nanoscale". PhD thesis. Jan. 2019.

[18] Toshikazu Nishida Yongke Sun Scott E. Thompson. *Strain Effect in Semiconductors, Theory and device and applications*. New York NY: Springer Verlag, 2010. ISBN: 978-1-4419-0552-9.

[19] Wikipedia contributors. *Electronic band structures: Basic concept.* [Online; accessed 3-January-2020]. 2019. URL: https://en.wikipedia.org/wiki/Electronic_band_structure#Assumptions_and_limits_of_band_structure_theory.

[20] Peter YU and Manuel Cardona. *Fundamentals of Semiconductors: Physics and Materials Properties.* 3rd ed. Springer-Verlag Berlin Heidelberg, 2010. ISBN: 978-3-642-00710-1. DOI: 10.1007/978-3-642-00710-1.

[21] Debdeep Jena. *Physics of semiconductors & nanostructures: Lecture 13 - Brillouin zones, crystal k*. 2017. URL: https://djena.engineering.cornell.edu/2017_ece4070_mse6050.htm.

[22] Bruce Averill and Patricia Eldredge. *General Chemistry: Principles, Patterns and Applications*. Saylor Foundation, 2011. ISBN: 13: 9781453322307.

[23] Matthew Schwartz and (Physics departments - Harvard University). *Statisical Mechanics, lecture 14*. 2019. URL: http://users.physics.harvard.edu/%7B~%7Dschwartz/teaching%7B%5C#%7Dsm.

[24] Nalin S. Fernando et al. " Band gap and strain engineering of pseudomorphic Ge 1 x y Si x Sn y alloys on Ge and GaAs for photonic applications ". In: *Journal of Vacuum Science & Technology B, Nanotechnology and Microelectronics: Materials, Processing, Measurement, and Phenomena* 36.2 (2018), p. 021202. ISSN: 2166-2746. DOI: 10.1116/1.5001948. URL: http://dx.doi.org/10.1116/1.5001948.

[25] Woo Sik Yoo et al. "Temperature Dependence of Photoluminescence Spectra from Crystalline Silicon". In: *ECS Journal of Solid State Science and Technology* 4.12 (2015), P456–P461. ISSN: 2162-8769. DOI: 10.1149/2.0251512jss.

[26] Xavier Gonze. *MAPR2014, Physics of Functional Materials, Propriété optiques des matériaux*. UCLouvain, Ecole Polytechnique de Louvain, 2019.

[27] J (Max Planck In-stitut für Festkörperforschung) Wagner. "Photoluminescence and excitation spectroscopy in heavily doped n- and p-type silicon J." In: *Physical review B* 29.February (1984).

[28] Kevin Guilloy et al. "Germanium under High Tensile Stress: Nonlinear Dependence of Direct Band Gap vs Strain". In: *ACS Photonics* 3.10 (2016), pp. 1907–1911. ISSN: 23304022. DOI: 10.1021/acsphotonics.6b00429.

[29] Chris Van de Walle and Richard M Martin. "Theoretical calculations of heterojunction discontinuities in the Si/Ge system". In: *Physical Review B* 34.8 (1986), pp. 5621–5634.

[30] J. Munguía et al. "Strain dependence of indirect band gap for strained silicon on insulator wafers". In: *Applied Physics Letters* 93.10 (2008). ISSN: 00036951. DOI: 10.1063/1.2978241.

[31] Song Li et al. "A study of strain-induced indirect-direct bandgap transition for silicon nanowire applications". In: *Journal of Applied Physics* 125.8 (2019). ISSN: 10897550. DOI: 10.1063/1.5052718.

[32] Zhe Shi et al. "Deep elastic strain engineering of bandgap through machine learning". In: *Proceedings of the National Academy of Sciences of the United States of America* 116.10 (2019), pp. 4117–4122. ISSN: 10916490. DOI: 10.1073/pnas.1818555116.

[33] Chris G. Van de Walle. "Band lineups and deformation potentials in the model-solid theory". In: *Phys. Rev. B* 39 (3 Jan. 1989), pp. 1871–1883. DOI: 10.1103/PhysRevB.39.1871. URL: https://link.aps.org/doi/10.1103/PhysRevB.39.1871.

[34] A. Gassenq et al. "Accurate strain measurements in highly strained Ge microbridges". In: *Applied Physics Letters* 108.24 (2016). ISSN: 00036951. DOI: 10.1063/1.4953788.

[35] David S. Sukhdeo et al. "Direct bandgap germanium-on-silicon inferred from 57% 100 uniaxial tensile strain [Invited]". In: *Photonics Research* 2.3 (2014), A8. ISSN: 2327-9125. DOI: 10.1364/prj.2.0000a8.

[36] Hongti Zhang et al. "Approaching the ideal elastic strain limit in silicon nanowires". In: *Science Advances* 2.8 (2016), pp. 2–10. ISSN: 23752548. DOI: 10.1126/sciadv.1501382.

[37] Ferran Ureña et al. "Strain in silicon nanowire beams". In: *Journal of Applied Physics* 112.11 (2012). ISSN: 00218979. DOI: 10.1063/1.4765025.

[38] "Direct-bandgap light-emitting germanium in tensilely strained nanomembranes". In: *Proceedings of the National Academy of Sciences of the United States of America* 108.47 (2011), pp. 18893–18898. ISSN: 00278424. DOI: 10.1073/pnas.1107968108.

[39] V. Reboud et al. "Ultra-high amplified strain on 200 mm optical Germanium-On-Insulator (GeOI) substrates: towards CMOS compatible Ge lasers". In: *Silicon Photonics XI* 9752 (2016), 97520F. ISSN: 1996756X. DOI: 10.1117/12.2212597.

[40] Donguk Nam et al. *Strain-induced pseudoheterostructure nanowires confining carriers at room temperature with nanoscale-tunable band profiles.* 2013. DOI: 10.1021/nl401042n.

[41] Jan Petykiewicz et al. "Direct Bandgap Light Emission from Strained Germanium Nanowires Coupled with High-Q Nanophotonic Cavities". In: *Nano Letters* 16.4 (2016), pp. 2168–2173. ISSN: 15306992. DOI: 10.1021/acs.nanolett.5b03976. arXiv: 1508.01255.

[42] Unknown. "Phys 774: Raman Scattering Introduction: Brillouin and Raman spectroscopy". In: *(New Jersey Institute of Technology)* (2007). URL: https://web.njit.edu/%7B~%7Dsirenko/Phys-774/Lecture11-2007.pdf.

[43] Thomas Wermelinger and Ralph Spolenak. "Stress analysis by means of raman microscopy". In: *Springer Series in Surface Sciences* 66 (2018), pp. 509–529. ISSN: 09315195. DOI: 10.1007/978-3-319-75380-5_21.

[44] Libretexts. *Raman: Theory.* May 2020. URL: https://chem.libretexts.org/Bookshelves/Physical_and_Theoretical_Chemistry_Textbook_Maps/Supplemental_Modules_(Physical_and_Theoretical_Chemistry)/Spectroscopy/Vibrational_Spectroscopy/Raman_Spectroscopy/Raman:_Theory.

[45] Ferran Ureña, Sarah H. Olsen, and Jean Pierre Raskin. *Raman measurements of uniaxial strain in silicon nanostructures.* 2013. DOI: 10.1063/1.4824291.

[46] Guerric Lemoine. "Time dependent plasticity and strain localization in nanocrystalline metallic thin films". PhD thesis. Institute of Mechanics, Materials and Civil Engineering (iMMC), UCLouvain, 2018. URL: https://dial.uclouvain.be/pr/boreal/en/object/boreal%7B%5C%%7D3A200816.

[47] Matteo Ghidelli et al. "Homogeneous flow and size dependent mechanical behavior in highly ductile Zr65Ni35 metallic glass films". In: *Acta Materialia* 131 (2017), pp. 246–259. ISSN: 13596454. DOI: 10.1016/j.actamat.2017.03.072.

[48] Umesh Bhaskar et al. "On-chip tensile testing of nanoscale silicon free-standing beams". In: *Journal of Materials Research* 27.3 (2012), pp. 571–579. ISSN: 08842914. DOI: 10.1557/jmr.2011.340.

[49] *Micro to Nano.* URL: https://www.microtonano.com/de/Overview-Tousimis-Critical-Poin-Dryers.php.

[50] *What is Ellipsometry?* Nov. 2019. URL: https://www.jawoollam.com/resources/ellipsometry-tutorial/what-is-ellipsometry.

[51] Renaud Vayrette, Jean Pierre Raskin, and Thomas Pardoen. “On-chip fracture testing of freestanding nanoscale materials”. In: *Engineering Fracture Mechanics* 150 (2015), pp. 222–238. ISSN: 00137944. DOI: 10.1016/j.engfracmech.2015.07.006. URL: http://dx.doi.org/10.1016/j.engfracmech.2015.07.006.

[52] M.-S. Colla. “Influence de l ’ hydruration sur les propriétés mécaniques de films minces de palladium”. Master thesis. UCLouvain - EPL, 2009.

[53] Romain Tuyaerts. “Internal stress and opto-electronic properties of pure and Al-doped ZnO thin films deposited by reactive sputtering”. PhD thesis. UCLouvain - EPL, 2018.

[54] Jianwei Wang et al. “Gallium arsenide (GaAs) quantum photonic waveguide circuits”. In: *Optics Communications* 327.September (2014), pp. 49–55. ISSN: 00304018. DOI: 10.1016/j.optcom.2014.02.040.

[55] *Integrated photonics*. URL: https://www.imec-int.com/en/integrated-photonics.

[56] Andy Eu Jin Lim et al. “Path to silicon photonics commercialization: 25 Gb/s platform development in a CMOS manufacturing foundry line”. In: *Optical Fiber Communication Conference, OFC 2014* Ild (2014), pp. 2–4. DOI: 10.1364/ofc.2014.th2a.51.

[57] *Intel silicon photonics*. URL: https://www.intel.com/content/www/us/en/architecture-and-technology/silicon-photonics/silicon-photonics-overview.html.

[58] *Silicium Archives*. URL: https://www.lelementarium.fr/element/silicium/.

[59] Alex Pip. *Stage en entreprise LFSA2995 (UCLouvain). Rapport confidentiel: prospection Germanium.* Tech. rep. Hydrométal S.A., 2019-2020.

[60] *Gallium*. URL: https://www.lelementarium.fr/element-fiche/gallium/.

[61] *Arsenic Archives*. URL: https://www.lelementarium.fr/element/arsenic/.

[62] M. Garside. *Leading polysilicon manufacturers worldwide by production 2015-2018*. Feb. 2020. URL: https://www.statista.com/statistics/585895/leading-polysilicon-manufacturers-worldwide/.

[63] *Arsenic Trioxyde*. URL: https://csm.umicore.com/en/products/arsenic/.

[64] *PPM Pure Metals*. URL: https://recylex.eu/en/ppm-pure-metals/.

[65] *PHOTONICS-SOI POUR ÉMETTEURS-RÉCEPTEURS OPTIQUES À HAUT DÉBI*. URL: https://www.soitec.com/fr/produits/photonics-soi.

[66] *GaAs Wafer*. URL: https://freiberger.com/en/products/.

[67] Günther Roelkens, Yannick De Koninck, and Shahram Keyvaninia. “Hybrid Silicon Lasers”. In: (2013). URL: https://www.photonics.intec.ugent.be/download/pub%7B%5C_%7D2704.pdf.

[68] Matteo Bosi and Giovanni Attolini. “Germanium: Epitaxy and its applications”. In: *Progress in Crystal Growth and Characterization of Materials* 56.3 (2010), pp. 146–174. ISSN: 0960-8974. DOI: https://doi.org/10.1016/j.pcrysgrow.2010.09.002. URL: http://www.sciencedirect.com/science/article/pii/S0960897410000100.

[69] Andrew R Barron et al. “Chemistry of Electronic Materials”. In: *Chemistry of Electronic Materials* (2011), pp. 1–344. ISSN: 0006-8993. DOI: S0006-8993(96)00826-8[pii].

[70] Danilo C. Curtolo, Semiramis Friedrich, and Bernd Friedrich. “High Purity Germanium, a Review on Principle Theories and Technical Production Methodologies”. In: *Journal of Crystallization Process and Technology* 07.04 (2017), pp. 65–84. ISSN: 2161-7678. DOI: 10.4236/jcpt.2017.74005.

[71] Christina Licht, Laura Talens Peiró, and Gara Villalba. “Global substance flow analysis of gallium, germanium, and indium: Quantification of extraction, uses, and dissipative losses within their anthropogenic cycles”. In: *Journal of Industrial Ecology* 19.5 (2015), pp. 890–903. ISSN: 15309290. DOI: 10.1111/jiec.12287.

[72] Umicore. *Germanium substrates*. 2020. URL: https://eom.umicore.com/en/germanium-solutions/products/germanium-substrates/.

[73] American Elements. *Gallium Arsenide Wafer*. 2020. URL: https://www.americanelements.com/gallium-arsenide-wafer-1303-00-0.

[74] N J Mohr et al. “Life cycle assessment of thin-film GaAs and GaInP/GaAs solar modules”. In: *Progress in Photovoltaics: Research and Applications* 15.2 (2007), pp. 163–179. DOI: 10.1002/pip.735. URL: https://onlinelibrary.wiley.com/doi/abs/10.1002/pip.735.

[75] I. Nawaz and G. N. Tiwari. “Embodied energy analysis of photovoltaic (PV) system based on macro- and micro-level”. In: *Energy Policy* 34.17 (2006), pp. 3144–3152. ISSN: 03014215. DOI: 10.1016/j.enpol.2005.06.018.

[76] European Commission. *Study on the review of the list of Critical Raw Materials - Critical Raw Materials Factsheets*. 2017, p. 93. ISBN: 978-92-79-47937-3. DOI: 10.2873/876644. URL: https://op.europa.eu/en/publication-detail/-/publication/08fdab5f-9766-11e7-b92d-01aa75ed71a1/language-en.

[77] U.S Geological Survey. *Mineral Commodity Summaries 2020*. 2020, pp. 1–196. ISBN: 9781411343627. URL: %5Curl%7Bhttps://pubs.usgs.gov/periodicals/mcs2020/mcs2020.pdf%7D.

[78] BRGM. “Fiche de criticité -silicium métal”. In: (2019), pp. 1–15. URL: http://www.mineralinfo.fr/sites/default/files/upload/documents/Fiches_criticite/fichecriticitesiliciummetal-publique20190729.pdf.

[79] Fraunhofer Institute For Systems and Innovation Research. *DERA Raw materials metal 2016.pdf*. 2016. URL: https://www.isi.fraunhofer.de/en/competence-center/nachhaltigkeit-infrastruktursysteme/projekte/rohstoffbedarf%7B%5C_%7Dzukunftstechnologien%7B%5C_%7Dii.html.

[80] Granta. *GRANTA EduPack*. Version 2019 Eco Audit Tool. URL: https://grantadesign.com/education/ces-edupack/tools/.

[81] European Chemicals Agency (ECHA). *Substance Infocard: silicon*. 2020. URL: https://echa.europa.eu/nl/substance-information/-/substanceinfo/100.028.300.

[82] European Chemicals Agency (ECHA). *Substance Infocard: germanium*. 2020. URL: https://echa.europa.eu/nl/substance-information/-/substanceinfo/100.028.331.

[83] European Chemicals Agency (ECHA). *Substance Infocard: gallium*. 2020. URL: https://echa.europa.eu/nl/substance-information/-/substanceinfo/100.028.330.

[84] European Chemicals Agency (ECHA). *Substance Infocard: arsenic*. 2020. URL: https://echa.europa.eu/nl/substance-information/-/substanceinfo/100.028.316.

[85] European Chemicals Agency (ECHA). *Substance Infocard: gallium arsenide*. 2020. URL: https://echa.europa.eu/nl/substance-information/-/substanceinfo/100.013.741.

[86] Fred H. Cardona, Manuel and Pollak. “Energy-Band Structure of Germanium and Silicon: The k · p Method”. In: *Physical Review* 142.2 (1966).

UNIVERSITÉ CATHOLIQUE DE LOUVAIN
École polytechnique de Louvain
Rue Archimède, 1 bte L6.11.01, 1348 Louvain-la-Neuve, Belgique | **www.uclouvain.be/epl**